

ABSTRACT

Title of Thesis: **Heavily Loaded Vehicle Tires:
Analysis and Characterization**

Nicholas Garcia, Master of Science, 2008

Thesis directed by: Dr. Balakumar Balachandran
Department of Mechanical Engineering

Vibration characterization and experimental modal analysis were carried out with a heavily loaded vehicle tire. These tires are typically subjected to loads that are over two times those experienced by a passenger car tire. The results obtained through experimental modal analysis were compared to similar results obtained for standard passenger car tires. The comparisons show that the heavily loaded tire has unique dynamic characteristics. Complex damping and nonlinear behavior were considered to explain these characteristics. A flexible ring tire model was used to investigate these nonlinear characteristics. Complex damping was also examined to explain the experimental observations. This thesis contains some of the first results on vibration characterization of heavily loaded vehicle tires. The incorporation of the results into a multi-degree-of-freedom tire model for use with the Effective Road Profile Control scheme used for vehicle durability simulation studies was also investigated.

HEAVILY LOADED VEHICLE TIRES:
ANALYSIS AND CHARACTERIZATION

By

Nicholas Garcia

Thesis submitted to the Faculty of the Graduate School of the
University of Maryland, College Park, in partial fulfillment
of the requirements for the degree of
Master of Science
2008

Advisory Committee:
Professor Balakumar Balachandran, Chair
Dr. Gregory A. Schultz
Associate Professor Hugh Bruck

© Copyright by
Nicholas J Garcia
2008

Dedication

To my parents, who have always been there for me. Thank you for all of the support and prodding.

Acknowledgements

Thanks to: Dr. Balakumar Balachandran, for his guidance, assistance and patience throughout this endeavor. His supervision and understanding made this research possible. Dr. Greg Schultz for getting me interested in vehicle dynamics and actual engineering. Without the opportunity to work with the FSAE team, I don't know where I would be right now. Kevin Kefauver from the Roadway Simulator group at Aberdeen Test Center for his assistance and guidance with running the tests and data acquisition.

Thanks to the Army Materiel Systems Analysis Activity for giving me the time and opportunity to pursue a degree while working full time.

Table of Contents

Dedication	ii
Acknowledgements	iii
List of Tables	v
Chapter 1: Introduction	1
1.1 Literature Review	1
1.1.1 Tires: Experimental Characterization.....	1
1.1.2 Tires: Modeling Efforts	8
1.1.3 Nonlinearities and Modal Analyses	11
1.1.4 Effective Road Profile Control (ERPC)	13
1.2 Objectives and Scope	15
1.3 Outline of Thesis.....	16
Chapter 2: Experimental Characterization.....	17
2.1 Experimental Setup.....	17
2.2 Assumptions Made.....	20
2.3 Sources of Error	21
2.4 Analysis Procedure	24
2.5 Experimental Results	28
Chapter 3: Modeling Efforts and Comparison with Experimental Results	43
3.1 Flexible Ring Model	43
3.2 Parameters and Numerical Solution.....	52
3.3 Model Results	53
Chapter 4: Extension of ERPC Framework.....	71
4.1 Transfer Function for a Multi-Degree-of-Freedom Tire Model.....	71
4.2 Connections with Earlier Work	78
Chapter 5: Concluding Remarks	80
5.1 Contributions to the Field.....	80
5.2 Suggestions for Future Work.....	81
Appendix and Programs.....	83
Bibliography	99

List of Tables

2.1 Data channels	19
2.2 Natural frequencies for the first five modes found through experimental modal analysis	29
3.1 Parameters used in model studies following Zegelaar (1997)	52
3.2 Flexible Ring Model Results Summary	54

List of Figures

1.1a	Experimental set-up: the positions and directions of the force excitations	3
1.1b	Experimental set-up: the positions and orientations of the accelerometers	3
1.2	Modes of a standing tire from experimental modal analysis due to radial impulse at point 3: $F_z=4000\text{N}$ (Zegelaar, 1997).....	4-5
1.3	Measured frequency response functions in the radial direction at point 3 of Figure 1.1 due to a radial excitation at point 3 for two different boundary conditions ...	6
1.4	Mode shapes due to radial excitation.....	7
1.5	Tire ring model	8
1.6	The tire ring and the deformation and the coordinate system used (Zegelaar, 1997)	9
1.7	Mass-spring-damper tire model used in ERPC	14
2.1	Experimental Arrangement	19
2.2	FRF's for the free and standing tire due to a modal hammer impulse.....	28
2.3	FRF of the radial acceleration to the input table acceleration. The circles show the areas of potential natural frequencies. Sine sweep test for the standing tire ($F_z=9000\text{ N}$) at 50 psi.	29
2.4	FRF of radial acceleration to vertical tire force. Sine sweep test for the standing tire ($F_z=9000\text{ N}$) at 50psi.	30
2.5	FRF of vertical tire force to table acceleration. Sine sweep test for the standing tire ($F_z=9000\text{ N}$) at 50psi.	31
2.6	FRF of spindle acceleration to table acceleration. Sine sweep test for the standing tire ($F_z=9000\text{ N}$) at 50psi.	32
2.7	Mode Shapes for the standing tire ($F_z=9000\text{lb}$). Sine sweep test. The two colors show the extremes of the mode shapes as it expands (one color) and contracts (the other)	33-34
2.8	Comparison of passenger tire modes and heavily loaded vehicle tire modes	36-37

2.9	Tangential Mode Shapes for the standing tire ($F_z=9000\text{lb}$). Sine sweep test.....	39-40
2.10	FRFs of tangential acceleration at different tire locations to table acceleration. Sine sweep test for the standing tire ($F_z=9000\text{ N}$) at 50psi. The different accelerometer locations around the tire are shown by a different color in the figure. All twelve sensor locations are present in the plot. The figure below shows the Phase of the FRF for only 3 points around the tire. The noisy channels were removed to give a clearer picture.....	41
2.11	FRFs of lateral acceleration at different tire locations to table acceleration. Sine sweep test for the standing tire ($F_z=9000\text{ N}$) at 50psi. The different accelerometer locations around the tire are shown by a different color in the figure. All twelve sensor locations are present in the plot	42
3.1	FRFs of radial displacement at different locations on the tire to input displacement. Predictions of the flexible ring model are shown. The different locations around the tire where the flexible ring model predictions were made are shown by a different color. The red line with amplitude of one for all frequencies correspond to the points at the base of the tire where the input was applied, hence, the corresponding FRF magnitude is 1... ..	55
	a) FRFs for one hundred and one equally distributed points around the tire....	55
	b) Representative plots at 90° and 180°	55
3.2	First three modes predicted by the flexible ring model with no damping. The dashed line in each figure corresponds to the nominal position, and the lines in blue and green correspond to the extremes of the mode shape motions.....	56
	a) 1st flexible mode, 97.19 Hz, flexible ring model with no damping.... ..	56
	b) 2 nd flexible mode, 120.2 Hz, flexible ring model with no damping.... ..	56
	c) 3 rd flexible mode, 140.8 Hz, flexible ring model with no damping.....	57
3.3	FRFs of radial displacement at different locations on the tire to input displacement. Predictions of the flexible ring model with regular damping, with magnitude $1e3\text{ Ns/m}$, are shown. The different locations around the tire where the flexible ring model predictions were made are shown by a different color. The red line with amplitude of one for all frequencies correspond to the points at the base of the tire where the input was applied, hence, the corresponding FRF magnitude is 1.....	58
	a) FRFs for one hundred and one equally distributed points around the tire....	58

b)	Representative plots at 90° and 180°.....	58
3.4	FRFs of radial displacement at different locations on the tire to input displacement. Predictions of the flexible ring model with regular damping, with magnitude 1e4 Ns/m, are shown. The different locations around the tire where the flexible ring model predictions were made are shown by a different color. The red line with amplitude of one for all frequencies correspond to the points at the base of the tire where the input was applied, hence, the corresponding FRF magnitude is 1.....	59
a)	FRFs for one hundred and one equally distributed points around the tire....	59
b)	Representative plots at 90° and 180°.....	59
3.5	FRFs of radial displacement at different locations on the tire to input displacement. Predictions of the flexible ring model with complex damping, with magnitude 1e5j Ns/m, are shown. The different locations around the tire where the flexible ring model predictions were made are shown by a different color. The red line with amplitude of one for all frequencies correspond to the points at the base of the tire where the input was applied, hence, the corresponding FRF magnitude is 1.....	60
a)	FRFs for one hundred and one equally distributed points around the tire....	60
b)	Representative plots at 90° and 180°.....	60
3.6	First three modes predicted by the flexible ring model with complex damping of magnitude $K_d=1e5j$. The dashed line in each figure corresponds to the nominal position, and the lines in blue and green correspond to the extremes of the mode shape motions	61
a)	2 nd flexible mode, 38.2 Hz, flexible ring model with complex damping $K_d=1e5j$	61
b)	3 rd flexible mode, 47.6 Hz, flexible ring model with complex damping $K_d=1e5j$	61
3.7	FRFs of radial displacement at different locations on the tire to input displacement. Predictions of the flexible ring model with complex damping, with magnitude 5e5j Ns/m, are shown. The different locations around the tire where the flexible ring model predictions were made are shown by a different color. The red line with amplitude of one for all frequencies correspond to the points at the base of the tire where the input was applied, hence, the corresponding FRF magnitude is 1.....	62

a)	FRFs for one hundred and one equally distributed points around the tire....	62
b)	Representative plots at 90° and 180°.....	62
3.8	First three modes predicted by the flexible ring model with complex damping of magnitude $K_d=5e5j$. The dashed line in each figure corresponds to the nominal position, and the lines in blue and green correspond to the extremes of the mode shape motions	63
a)	2 nd flexible mode, 8.15 Hz, flexible ring model with complex damping $K_d=5e5j$	63
b)	3 rd flexible mode, 9.80 Hz, flexible ring model with complex damping $K_d=5e5j$	63
3.9	FRFs of radial displacement at different locations on the tire to input displacement. Predictions of the flexible ring model with complex damping, with magnitude $1e6j$ Ns/m, are shown. The different locations around the tire where the flexible ring model predictions were made are shown by a different color. The red line with amplitude of one for all frequencies correspond to the points at the base of the tire where the input was applied, hence, the corresponding FRF magnitude is 1.....	64
a)	FRFs for one hundred and one equally distributed points around the tire....	64
b)	Representative plots at 90° and 180°.....	64
3.10	First three modes predicted by the flexible ring model with complex damping of magnitude $K_d=1e6j$. The dashed line in each figure corresponds to the nominal position, and the lines in blue and green correspond to the extremes of the mode shape motions	65
a)	2 nd flexible mode, 4.26 Hz, flexible ring model with complex damping $K_d=1e6j$	65
b)	3 rd flexible mode, 5.28 Hz, flexible ring model with complex damping $K_d=1e6j$	65
3.11	FRFs of radial displacement at different locations on the tire to input displacement. Predictions of the flexible ring model with cubic stiffness, with magnitude $1e6$ N/m ³ , are shown. The different locations around the tire where the flexible ring model predictions were made are shown by a different color. The red line with amplitude of one for all frequencies correspond to the points at the base of the tire where the input was applied, hence, the corresponding FRF magnitude is 1.....	66

a)	FRFs for one hundred and one equally distributed points around the tire....	66
b)	Representative plots at 90° and 180°.....	66
3.12	FRFs of radial displacement at different locations on the tire to input displacement. Predictions of the flexible ring model with cubic stiffness, with magnitude $1e7 \text{ N/m}^3$, are shown. The different locations around the tire where the flexible ring model predictions were made are shown by a different color. The red line with amplitude of one for all frequencies correspond to the points at the base of the tire where the input was applied, hence, the corresponding FRF magnitude is 1.....	67
a)	FRFs for one hundred and one equally distributed points around the tire....	67
b)	Representative plots at 90° and 180°.....	67
3.13	FRFs of radial displacement at different locations on the tire to input displacement. Predictions of the flexible ring model with cubic stiffness, with magnitude $1e8 \text{ N/m}^3$, are shown. The different locations around the tire where the flexible ring model predictions were made are shown by a different color. The red line with amplitude of one for all frequencies correspond to the points at the base of the tire where the input was applied, hence, the corresponding FRF magnitude is 1.....	68
a)	FRFs for one hundred and one equally distributed points around the tire....	68
b)	Representative plots at 90° and 180°.....	68
4.1	Spring and damper tire model used in ERPC.....	72
4.2	Spring and damper tire model used in ERPC in the longitudinal direction.....	74

Chapter 1

Introduction

The study of vehicle dynamics starts with the interaction between the tires of the vehicle and the road. A large portion of all of the loads on the vehicle can be tracked back to the loads on the tires. Since the tires are the only part of the vehicle that is in direct contact with the environment, the loads in the suspension and steering components can all be traced back to the loads at the tire patch, where the flexible tire contacts the road. In order to predict vehicle dynamics loads it is important to have an accurate tire model. As the performance requirements for vehicles increase a more precise understanding of vehicle dynamics is needed. This requires a much better understanding of the dynamic properties of vehicle tires. Modal analysis of passenger vehicle tires started in the 1960's. A major contributor to this study was Pacejka (1993) who proposed a semi-empirical tire model known as the "magic" tire formula. These experiments focused on comparing the behavior of bias ply with new radial tires. These early tests utilized a fixed axle test set up with radial excitations.

1.1 Literature Review

1.1.1 Tires: Experimental Characterization

Over the last decade, considerable amount of work has been done by Zegelaar (1997) and Yam, Guan, and Zhang (2000) to examine the three dimensional mode shapes

of passenger tires. These experiments use a free tire set up with the tire suspended from above with radial and tangential excitations. Zegelaar (1997) examined the in-plane vibrations of such a tire in a free condition and a loaded (standing) condition and compared the experimental results with analytical results derived from the flexible ring modal proposed by Gong (1993). The loaded condition consisted of a vertical force, F_z , of 4000 N. By comparison, the heavily loaded tire analyzed in this thesis is subjected to a static loading force of 9000 N. This is over two times as much as the static load a passenger tire is subjected to in Zegelaar and Yam *et al.*'s analyses. Zegelaar's analyses show modes starting around 100 Hz with the first flexible mode of the free tire to be at 115.9 Hz, see Figure 1.2. In Figures 1.1 to 1.3, the experimental arrangement and results obtained by Zegelaar are shown.

Zegelaar (1997) performed experimental modal analysis by placing tri-axial accelerometers around the tire tread and hitting the tire in various places with a modal hammer. The input force from the hammer is recorded along with the outputs of the accelerometers in order to determine the frequency response function between the input and an output force. In Figure 1.1a the force excitations used are shown and in Figure 1.1b the positions and orientations of the accelerometers are shown. The input radial force is applied at point 3, as shown in figure 1.1a. This experiment is not truly indicative of the response of the tire, since the input force is in general applied at the contact patch; that is point 11. The experimental modal analysis performed in this thesis will make use of an input force at the contact patch of the tire. The experimental set-up used by Zegelaar and others is similar to the one that is used in this thesis work, except that a harmonic excitation produced by a shaker table is used instead of a modal hammer

excitation. Modal hammer strikes could not impart enough force to sufficiently excite the much stiffer heavily loaded tire studied in this thesis.

Yam, Guan, and Zhang (2000) used a similar test set up and analyzed the full three-dimensional motion of the tire to get in-plane and out-of-plane vibrations of the tire. Their results showed the first flexible mode occurs around 120 Hz, which agrees with Zegelaar's findings. In the analysis by Yam *et al* only the free tire modes were examined. In Figure 1.4 the modes found in Yam *et al*'s analyses in all three dimensions for a radial excitation are shown.

In this thesis the author examines the three dimensional vibrations of a heavily loaded military grade tire due to radial excitations. The first flexible mode is seen at 54 Hz which is significantly lower than those found for a standard passenger tire. The natural frequencies of these modes are important since the vehicle can excite the lower frequencies during normal operation. Out-of-plane motion was also observed in response to a radial in-plane excitation. The modes for the passenger tire analyzed by Zegelaar are at significantly higher frequencies than those of the much stiffer and heavier tire studies in this work.

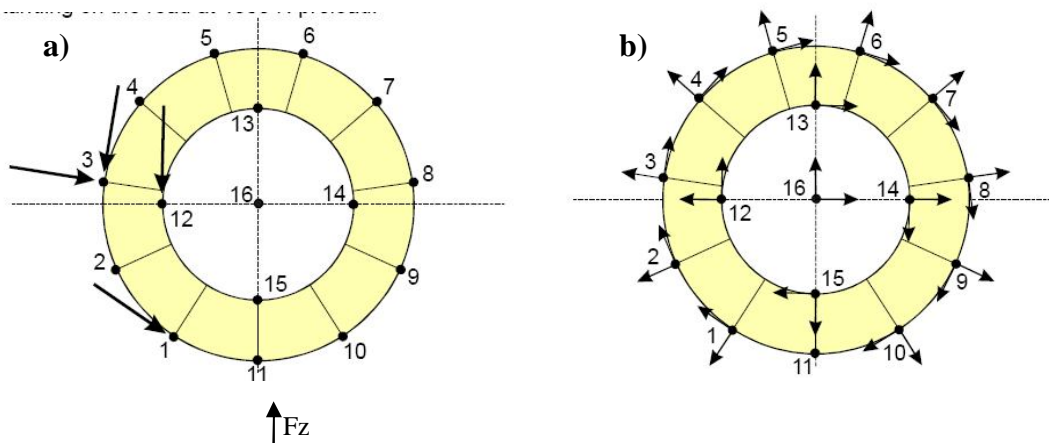


Figure 1.1: Experimental set-up: a) positions and directions of the force excitations and b) positions and orientations of the accelerometers (Zegelaar, 1997).

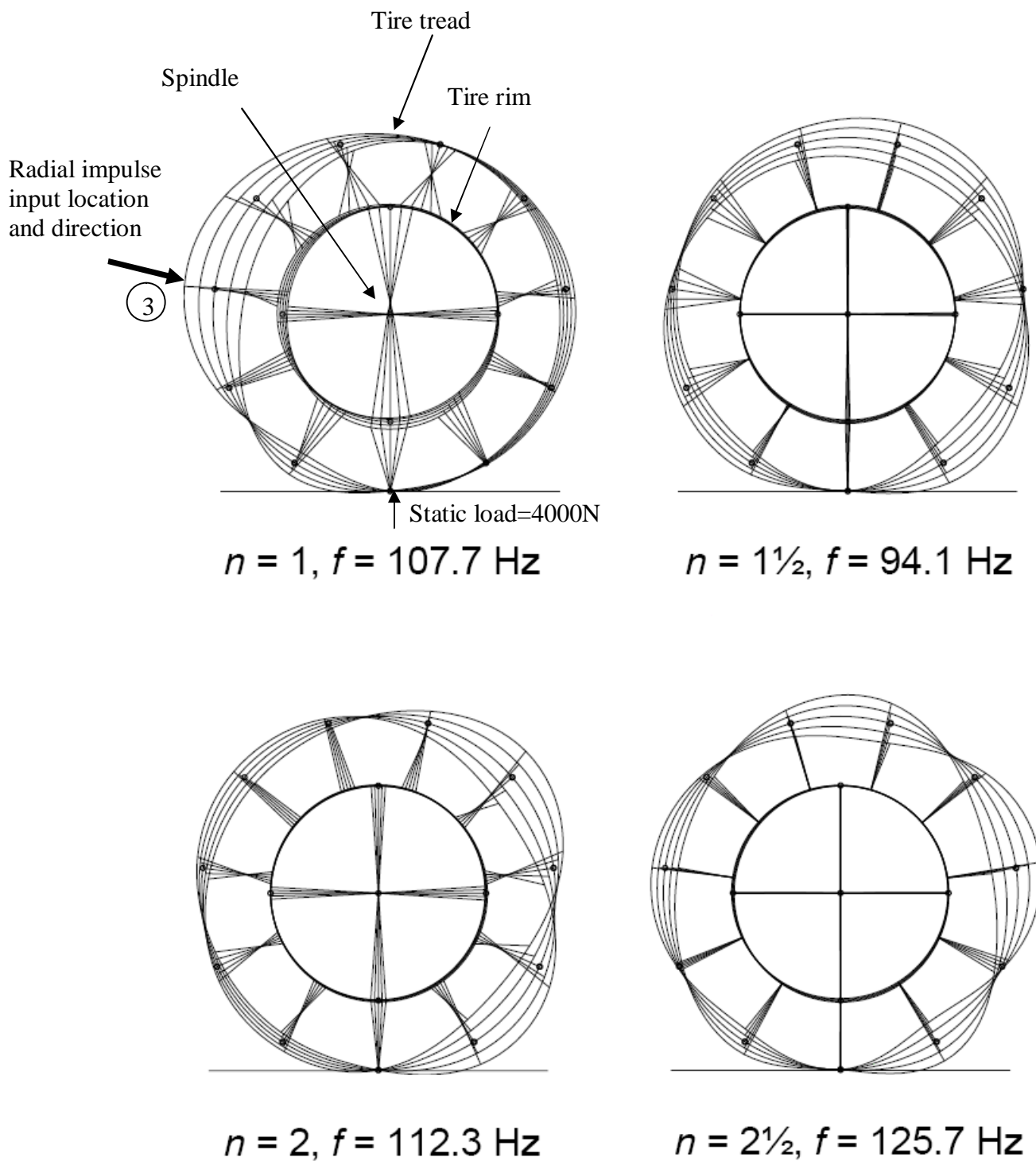
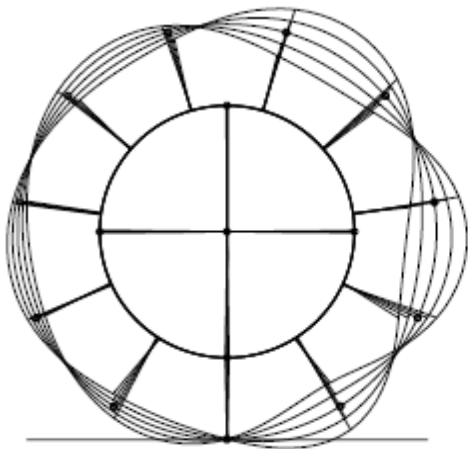
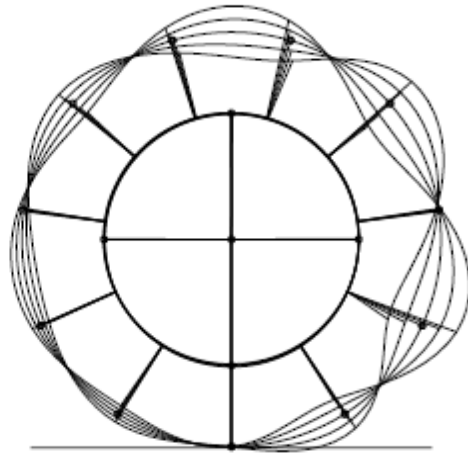


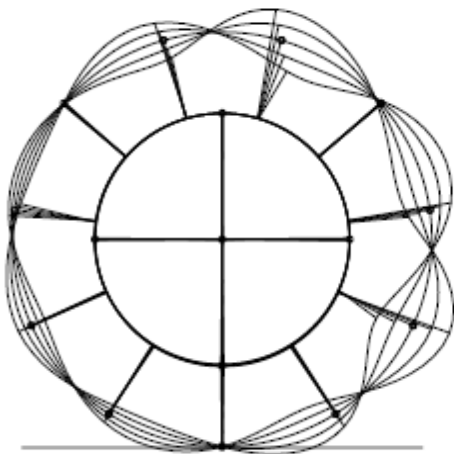
Figure 1.2: Modes of a standing tire from experimental modal analysis due to radial impulse at point 3: $F_z=4000\text{N}$ (Zegelaar, 1997).



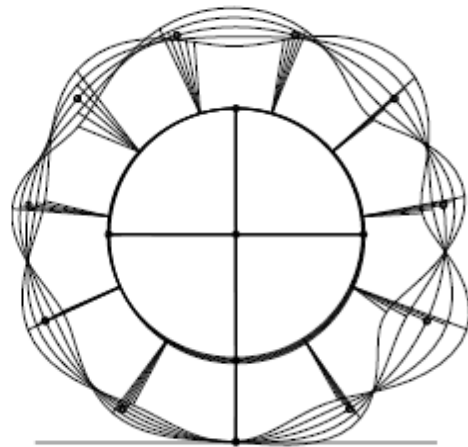
$n = 3, f = 140.9 \text{ Hz}$



$n = 3\frac{1}{2}, f = 156.8 \text{ Hz}$



$n = 4, f = 172.5 \text{ Hz}$



$n = 4\frac{1}{2}, f = 188.8 \text{ Hz}$

Figure 1.2 (continued): Modes of a standing tire from experimental modal analysis due to radial impulse at point 3: $F_z=4000\text{N}$ (Zegelaar, 1997).

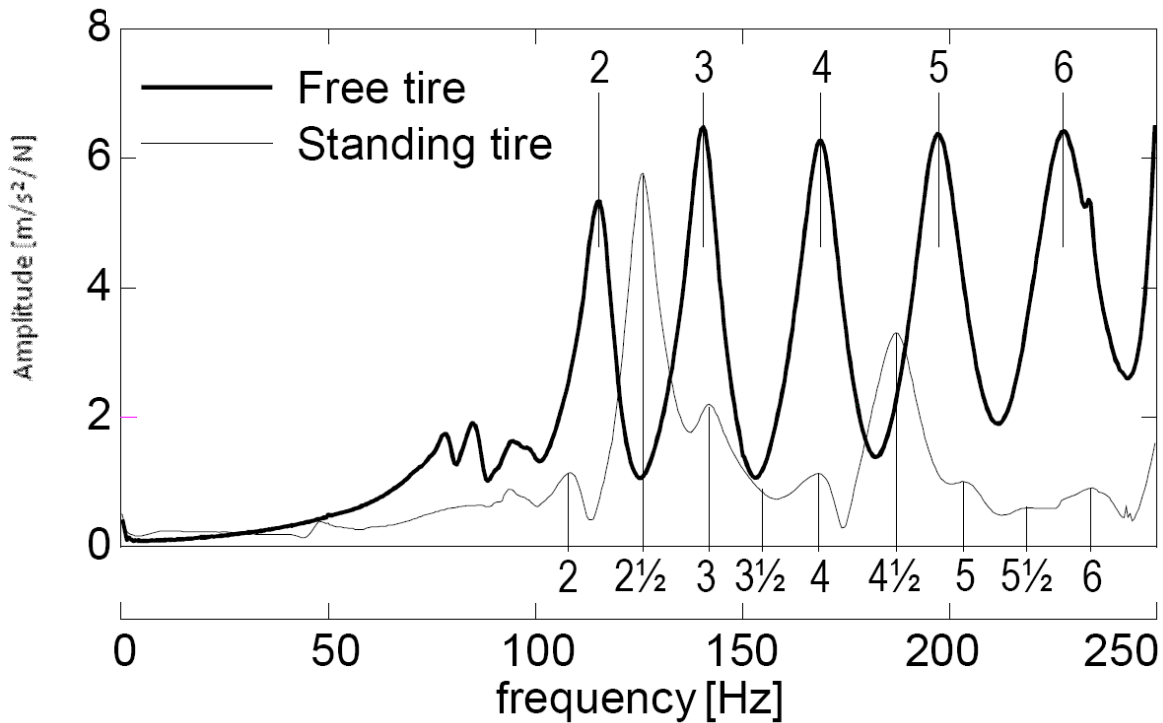


Figure 1.3: Measured frequency response functions in the radial direction at point 3 of Figure 1.1 due to a radial excitation at point 3 for two different boundary conditions (Zegelaar, 1997).

The mode numbering convention used in Zegelaar’s work is shown in Figure 1.3. The peaks in the frequency response function (FRF) correspond to the natural frequencies of the modes of a particular system. The modal peaks for the free tire are easy to see, with evenly spaced distinct peaks. These modes are numbered in ascending order. The modal peaks from the free tire (unloaded) are compared to the modes from the standing (loaded) tire. If a modal frequency for the standing tire lines up with that of the free tire, the standing tire mode is given the corresponding integer value used for the free tire mode. If a peak from the standing tire frequency response function does not line up with a peak in the free tire frequency response function, then the standing tire is classified by a real number with one half.

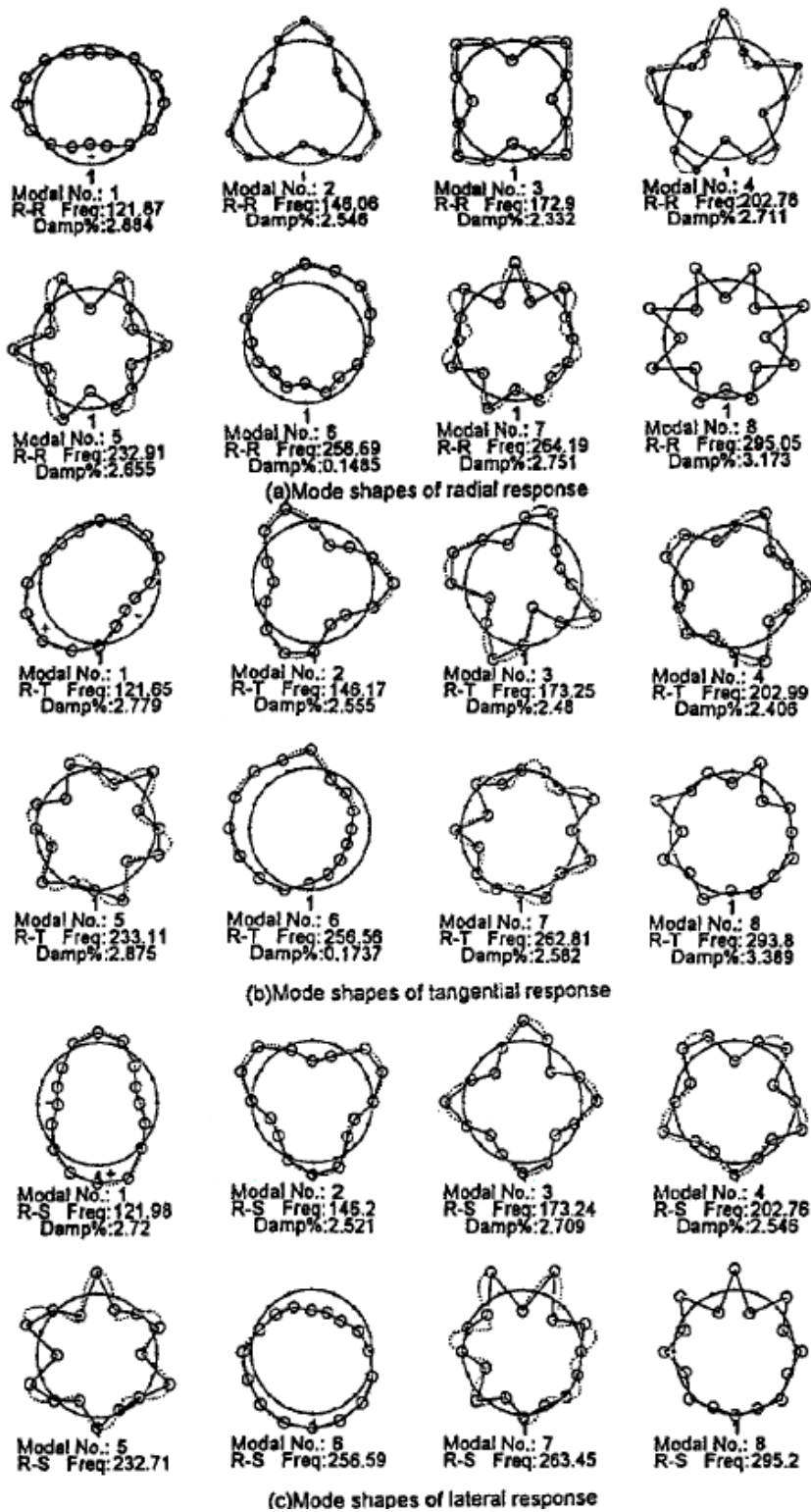


Figure 1.4: Mode shapes due to radial excitation (Yam *et al.*, 2000).

1.1.2 Tires: Modeling Efforts

The flexible ring model uses a circular beam that is supported by an elastic spring foundation to describe the motion of tread of the tire. The beam can bend and deform along its axis just as the tread of the tire would deform. So this model differs from the classic string model, in that the ring can deform (Pacjeka, 2005). The equations of motion of the flexible ring model are based on the PhD dissertation of Gong (1993).

The tire ring model, which is shown in Figure 1.5, is comprised of a circular ring that is supported on an elastic foundation. The flexible ring model allows for displacement of the ring elements beyond the standard spindle displacement as it takes into account the tire tread deformation. In Figure 1.6, the coordinate system used to develop this model is shown.

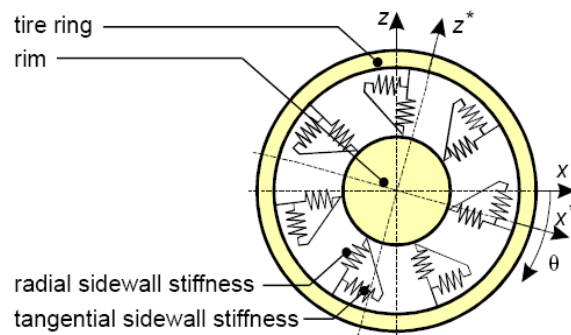


Figure 1.5: Tire ring model (Zegelaar, 1997).

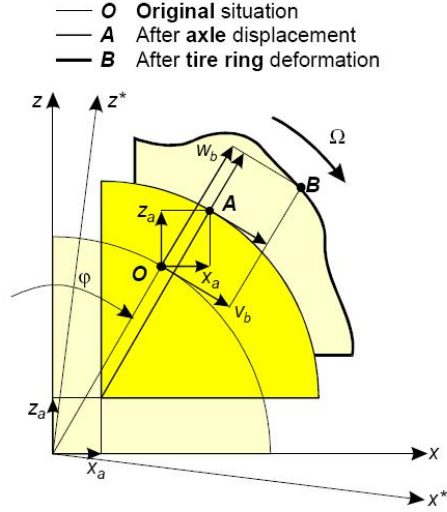


Figure 1.6: Tire ring, deformation field, and coordinate system used (Zegelaar, 1997).

The initial position on a ring element is shown as point **O**, the position reached after the spindle displacement is shown as point **A**, and the position reached after both spindle displacement and the tire ring deformation is shown by the point **B**. In the doctoral work of Gong (1993) the steps undertaken are provided. These steps are based on the strain displacement relations, strain energy, and virtual work for determining the equations of motion. The resulting equations have the form

$$\begin{aligned} \frac{EI}{R^4} \left(\frac{\partial^3 w_b}{\partial \theta^3} - \frac{\partial^2 v_b}{\partial \theta^2} \right) - \frac{EA}{R^2} \left(\frac{\partial w_b}{\partial \theta} + \frac{\partial^2 v_b}{\partial \theta^2} \right) + \frac{F_s}{R^2} \left(v_b - \frac{\partial w_b}{\partial \theta} \right) + \frac{p_0 b_R}{R} \left(\frac{\partial w_b}{\partial \theta} - v_b \right) \\ + c_{bv} \left(v_b + x_a \sin \theta + z_a \cos \theta - R \theta_a \right) + \rho A \left(\frac{\partial^2 v_b}{\partial t^2} + 2\Omega \frac{\partial w_b}{\partial t} - \Omega^2 v_b \right) = q_{cv} \end{aligned} \quad (1.1)$$

$$\begin{aligned} \frac{EI}{R^4} \left(\frac{\partial^4 w_b}{\partial \theta^4} - \frac{\partial^3 v_b}{\partial \theta^3} \right) + \frac{EA}{R^2} \left(w_b + \frac{\partial v_b}{\partial \theta} \right) + \frac{F_s}{R^2} \left(\frac{\partial v_b}{\partial \theta} - \frac{\partial^2 w_b}{\partial \theta^2} \right) - \frac{p_0 b_R}{R} \left(w_b + \frac{\partial v_b}{\partial \theta} \right) \\ + c_{bw} \left(w_b - x_a \cos \theta + z_a \sin \theta \right) + \rho A \left(\frac{\partial^2 w_b}{\partial t^2} - 2\Omega \frac{\partial v_b}{\partial t} - \Omega^2 w_b \right) = q_{cw} \end{aligned} \quad (1.2)$$

$$m_a \frac{\partial^2 x_a}{\partial t^2} + \pi R (c_{bv} + c_{bw}) x_a - R \int_0^{2\pi} (c_{bw} w_b \cos \theta - c_{bv} v_b \sin \theta) d\theta = -F_{ax} \quad (1.3)$$

$$m_a \frac{\partial^2 z_a}{\partial t^2} + \pi R (c_{bv} + c_{bw}) z_a + R \int_0^{2\pi} (c_{bw} w_b \sin \theta + c_{bv} v_b \cos \theta) d\theta = -F_{az} \quad (1.4)$$

$$I_{ay} \frac{\partial^2 \theta_a}{\partial t^2} + 2\pi c_{bv} R^3 \theta_a - R^2 \int_0^{2\pi} c_{bv} v_b d\theta = -M_{ay} \quad (1.5)$$

where the following notation has been used.

q_{cv}, q_{cw} : external distributed force on the ring

F_{ax}, F_{az} : external forces acting on the ring

M_{ay} : external torque acting on the ring

v_b, w_b : tangential and radial displacements

x_a, z_a : horizontal and vertical rim displacements

Ω : rotational speed

θ_a : small deviation of the angular displacement of the rim due to Ω

EI : bending stiffness of ring

E : Young's modulus of the ring material

I : inertia moment of the cross-section of the ring

$F_s = p_0 b_R R + \rho A R^2 \Omega^2$: pretension in the ring

c_{bv} : tangential sidewall stiffness

c_{bw} : tangential sidewall stiffness

R : radius of the ring

b_R : width of the ring

p_0 : tire inflation pressure

m_a : mass of rim

I_a : moment of inertia of rim

(see Figure 1.6 for the coordinate orientations)

In this thesis it is assumed that the distributed forces on the ring, the rim displacements, the angular displacement of the rim, and the rotational speed are all zero.

In addition, the substitution for the pretension in the ring is carried out.

$$F_s = p_0 b_R R + \rho A R^2 \Omega^2$$

This leads to the following two equations of motion:

$$\frac{EI}{R^4} \left(\frac{\partial^3 w_b}{\partial \theta^3} - \frac{\partial^2 v_b}{\partial \theta^2} \right) - \frac{EA}{R^2} \left(\frac{\partial w_b}{\partial \theta} + \frac{\partial^2 v_b}{\partial \theta^2} \right) + c_{bv} v_b + \rho A \frac{\partial^2 v_b}{\partial t^2} = 0 \quad (1.6)$$

$$\frac{EI}{R^4} \left(\frac{\partial^4 w_b}{\partial \theta^4} - \frac{\partial^3 v_b}{\partial \theta^3} \right) + \frac{EA}{R^2} \left(w_b + \frac{\partial v_b}{\partial \theta} \right) + \frac{p_0 b_R}{R} \left(-\frac{\partial^2 w_b}{\partial \theta^2} - w_b \right) + c_{bw} w_b + \rho A \frac{\partial^2 w_b}{\partial t^2} = 0 \quad (1.7)$$

1.1.3 Nonlinearities and Modal Analyses

There are principal assumptions that form a basis for modal analysis, which is strictly valid for linear systems. One of them is that the system invariants, including the natural frequencies, damping ratios, mode shapes, and frequency response functions are not affected by the level of input excitation applied during the test. A second assumption

is that there is no nonlinear coupling between the modes, that is, the response of one mode does not affect the response of another mode in a nonlinear fashion. Both of these assumptions can break down when nonlinearities are inherent in the system (e.g., Worden and Tomlinson, 2000). In nonlinear systems, various phenomena such as jumps, nonlinear resonances, and bifurcations can occur that can affect the results (Nayfeh and Balachandran, 1995).

There are a number of methods that have been used for examining the presence of nonlinearities in experimental modal testing. Sine sweep and harmonic input tests can be particularly useful for detecting effects like nonlinear resonances. Exciting the system at one-half, one-third, twice, and three times the linear natural frequency can reveal nonlinear resonances that are common in nonlinear systems (Zavodney, 1987). It is quite common for sinusoidal inputs at one frequency to excite a resonance at a different frequency in a nonlinear system. This does not happen in a linear system, and a slow sine sweep test of a harmonic excitation is useful to detect such an occurrence.

Superposition is only strictly valid for linear systems. The superposition principle can be used to detect nonlinearities in a system by observing deviations from linear superposition (Nayfeh and Balachandran, 1995). Nyquist plots are also a way to detect nonlinearities in a system. A Nyquist plot is a polar plot showing the gain and phase of a frequency response. For a linear system excited close to resonance and exhibiting a response that contains only one mode, Nyquist plots are circular. For a nonlinear system the Nyquist plots can become distorted into ellipses or other shapes (Zavodney, 1987).

Nonlinear resonances can be a problem in experimental modal analysis. The excitation of one mode at a particular frequency can lead to a response at another

frequency as well as participation of other modes. For a set of given damping and frequency values, it is possible for a system to undergo bifurcations in which a fixed point of a dynamical system loses stability and the system experiences a continuous exchange of energy from one mode to another. These nonlinear phenomena can occur at extremely low excitation levels (Zavodney, 1987).

1.1.4 Effective Road Profile Control (ERPC)

One important use for accurate tire models is in corrective signal response algorithms for experimental vehicle dynamics simulations. Effective Road Profile Control (ERPC) is a simulation control method developed by MTS Systems Corporation. ERPC makes use of the vehicle response with a non vehicle specific control algorithm to determine changes in a vehicle's performance over time. The Roadway Simulator group of the U.S. Army at the Aberdeen Testing Center, Aberdeen Proving Ground, Maryland is interested in this technique for carrying out experimental vehicle simulations. The principle behind ERPC is that by using a standard tire model one can determine the effective road profile (ERP) due to a random input signal. The ERP is then used as a feedback input to drive the simulation inputs. Normally, control algorithms require for a new vehicle road response to be taken for each vehicle for each test course being analyzed. With ERPC, this is not necessary. With an accurate tire model, it is expected that the ERP can be determined for any vehicle over any test course. The variance in the ERP is determined to find out when the performance characteristics of a vehicle have changed. This could occur due to a failure or wear-out of a suspension component.

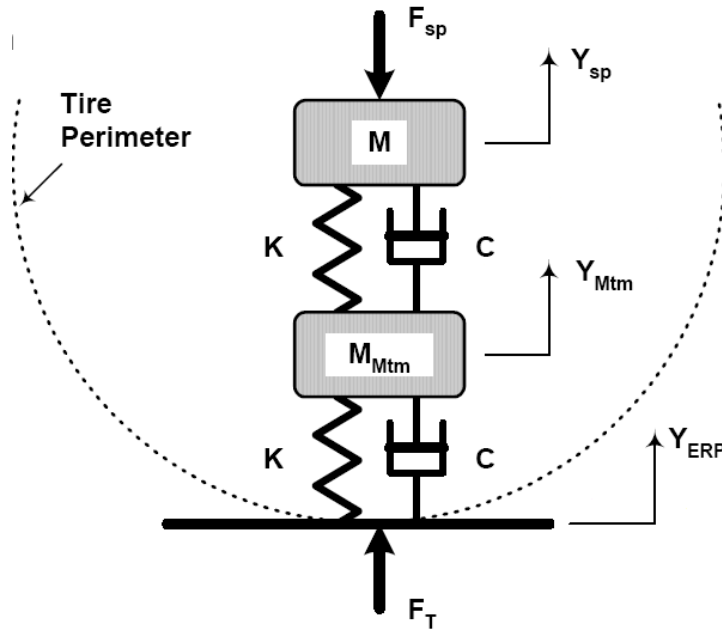


Figure 1.7: Mass-spring-damper tire model used in ERPC.

The current tire models being used for ERPC are simple single degree of freedom mass-spring-damper models in the vertical direction, see Figure 1.7. It may be possible to make the process more accurate by using a three-dimensional tire model based on the results of this thesis, where it is proposed to use both in plane and out of plane tire modes to determine the ERP.

The tire model is used to predict a specific road profile based upon a set of spindle dynamic response data. The control algorithm then changes the input forces to match an expected road profile. In this way, once one has a tire model in place for each vehicle the same effective road profile can be used for different vehicle configurations which result in different force inputs but correspond to the same road profile for a test course. The tire

model needs to enable both accuracy and efficiency. The control process necessitates that the prediction of the ERP from the spindle dynamics with the tire model must be computationally fast enough so that the control feedback can work in real time at high frequencies.

Another use for accurate tire modeling efforts is in dynamics modeling efforts. Tire models are required for all vehicle dynamics models. These models are created by using special software packages such as DADS, VirtualLab, and ADAMS dynamics modeling software. One of the largest sources of error in these models is the loads generated at the tire patch of the vehicles. Generic tire models are used to determine vertical, lateral, and longitudinal forces due to the rolling contact of the tire and the ground. If these tire models are not accurate, the loads and subsequent response of the rest of the vehicle can be significantly affected causing large errors in the overall response of the vehicle. Refined tire models are critical for improving the accuracy of these models. The results from this study will hopefully lead to a better understanding of the tire dynamics and eventually to more accurate tire models for use with these software packages, in particular, for heavily loaded vehicles.

1.2 Objectives and Scope

A main objective of this study is to determine the natural frequencies and mode shapes of a heavily loaded tire. These results are to eventually be used to for the creation of an accurate three-dimensional tire model for use in dynamics modeling and experimental input response control algorithms, that is, algorithms like ERPC. To

achieve this objective, an experiment was designed and conducted to measure the response of the tire tread to various input signals.

A second objective of this study is to determine if any non-linear characteristics are present in the response of the heavily loaded tire system and carry out an attempt to determine the forms and characterize them. Predictions made with the flexible ring model are compared with results obtained from the experimental modal analysis in an effort to understand the tire vibratory response characteristics.

1.3 Outline of Thesis

The rest of this thesis is organized as follows. In the second chapter, the experimental modal analysis work is described. The experiment setup and procedure are discussed in detail. The results are shown, and the mode shape information is examined. In the third chapter, the analysis is carried out with the flexible ring model. The predicted modal response from the flexible ring model is compared with the results obtained from the experimental modal analyses. Nonlinear terms are added to the flexible ring model and the resulting dynamics is studied to explain some of the observations made in the experiments. In the fourth chapter, the tire model for the Effective Road Profile Control algorithm is expanded into three dimensions. The feasibility of using tire modes found in the experimental modal analysis and the tire model used in the third chapter for the ERPC process is discussed. In the final chapter, concluding remarks are given along with suggestions for future work. An appendix containing the programs used in this work is also included

Chapter 2

Experimental Characterization

2.1 Experimental Setup

To determine the modes and mode shapes of the tire, experiments were performed by using a shaker table at the Aberdeen Test Center in Aberdeen Proving Grounds. The tire was mounted to the outer frame of the table and a plate fixed to the table was used to load the tire and subject it to various inputs. The fixture was machined out of steel and was clamped to the outer frame of the table. A plate was bolted to the shaker table by using a separate machined fixture to apply the loading input on the tire. The bolts holding the plate to the shaker table were tightened by using a hydraulic hammer. The plate and fixture were carefully aligned after every installation.

The tire was mounted with a MTS Spinning Wheel Integrated Force Transducer (SWIFT) to measure the forces and moments at the center of the tire. This transducer is attached between the hub and wheel, and it is used to measure the forces and moments being input into the hub and spindle by the tire. Accelerometers were mounted on the loading plate, the spindle of the tire, and at various points on the circumference of the tire. The accelerometers on the tire tread were placed at 45° , 75° , 90° , 120° , 150° , 180° , 210° , 240° , 270° , 285° , 315° , and 330° , as shown in Figure 2.1. As a reference, the loading plate was placed at 0° . The accelerometer blocks (including the accelerometers) weighed only a few ounces, compared to the tire, which weighed hundreds of pounds.

The depth of the tire tread and the size of the accelerometer blocks hindered attempts to attach the blocks to the tire tread in a conventional fashion. The accelerometers were mounted to the tire by using modeling clay that was pressed into the tread of the tire and molded around the accelerometer blocks. This mounting procedure took a few tests to get it right, but in the final tests, it was possible to use the clay was able to attach the accelerometers to the tire tread with only a slight change in the orientation of the blocks during a test. The problems experienced while attaching the accelerometers is further discussed in Section 2.3. Both SoMat and ATC's Advanced On-Board Computing System (ADOCS) data acquisition systems were used. The radial tire accelerations, spindle accelerations, and the SWIFT vertical force were recorded on the SoMat while the table accelerations and three SWIFT forces were acquired with the ADOCS system. In Table 2.1, the list of data channels collected during the experiments are listed.

The input signals used during the experiment were a 10-g impulse comprised of a 10ms saw tooth, a linear sine sweep from 5 Hz to 200 Hz, and a random excitation input. The experiments were repeated for tire pressures of 30psi, 40psi, and 50psi. The static load was kept around 9000 N. The static load is one of the uncontrolled variables in the test that caused some minor inconsistencies throughout the testing. The airbag used to apply the static load for the shaker table was unreliable and would lose pressure over the course of a test.

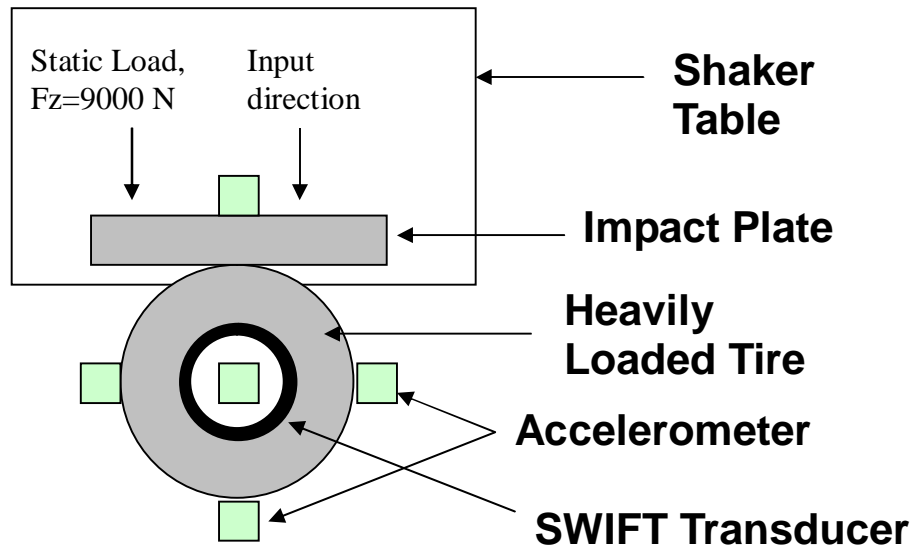


Figure 2.1: Experimental arrangement.

Table 2.1: Data channels.

SOMAT		ADOCS	
1	Radial Acceleration of Pt 1, x	1	SWITFT Force, Vert
2	Radial Acceleration of Pt 1, y	2	SWITFT Force, Lat
3	Radial Acceleration of Pt 1, z	3	SWITFT Force, Long
4	SWIFT Force, Vert	4	Table Acceleration, Lat
5	Radial Acceleration of Pt 2, x	5	Table Acceleration, Long
6	Radial Acceleration of Pt 2, y		
7	Radial Acceleration of Pt 2, z		
8	Radial Acceleration of Pt 3, x		
9	Radial Acceleration of Pt 3, y		
10	Radial Acceleration of Pt 3, z		
11	Radial Acceleration of Pt 4, x		
12	Radial Acceleration of Pt 4, y		
13	Radial Acceleration of Pt 4, z		
14	Spindle Acceleration, Vertical		
15	Spindle Acceleration, Lateral		
16	Spindle Acceleration, Longitudinal		

2.2 Assumptions Made

There are some assumptions underlying the analysis. The first is that the modes are decoupled or well separated in terms of their frequency responses. This means that we can excite each mode separately. It is speculated that this may not actually be the case, and that the analysis will prove or disprove this assumption. The previous work done in the subject of tire dynamics has used this assumption, and for standard passenger tires this assumption has held up through the analysis (Zegelaar, 1997). Well separated modes means that the peaks of the frequency response functions where the natural frequencies of the modes are located are not too close to each other that the identification of each separate mode becomes difficult. If the modes are well separated and decoupled they can be solved for separately as discussed in Section 2.4.

Another assumption that is made is that the spindle dynamics is negligible in comparison to the radial tire dynamics at the frequencies of interest. Spindle accelerations were taken and the analysis of the results is shown in Figure 2.6. In Figures 2.2 to 2.5, different frequency response functions are shown. The spindle dynamics is predominantly relegated to frequencies under 30 Hz. The modes of interest all have natural frequencies above 30 Hz, with only a few rigid body modes even being close to the spindle frequencies. The amplitude of the FRF of the spindle dynamics is also much lower than the amplitude of the radial tire dynamics for frequencies above 40 Hz. Thus, it is justifiable to assume that the spindle dynamics can be neglected in the analysis.

2.3 Sources of Error

As mentioned previously the static load on the tire was another source of error in the experiment. The static load was not constant as it dissipated throughout each test. The load was created by a large airbag within the shaker table apparatus. The airbag would lose pressure over every test and the static load would lose close to one thousand Newtons over the course of a test. The static load was reconfigured between each test but it was still a large source of inconsistency in the experiment. To offset the drift in the airbag load, the initial static load was increased to around 10,000 N so that the average load would stay close to 9,000 N.

The triaxial accelerometer blocks were attached to the tire by using modeling clay. A visual inspection was carried out before and after every test run but the alignment of each block did change during and between each test. The blocks could start to sag as the molding clay deformed during the test. As the clay deformed during the test the orientation of the accelerometer blocks changed slightly. The changes in the orientations of the blocks caused the measured accelerations to be skewed slightly as the directions of the accelerometer axes were not exactly the same for each position around the circumference of the tire. This variance was not recorded and was visually noticeable after the rest runs, and this is believed to be the leading cause of the variance in the peaks of the FRF's associated with a particular accelerometer location. The changes in the orientations of the accelerometers were below 10° over the course of a test. During some tests, one or more accelerometer completely detached from the tire as the clay fixture failed. These tests were repeated, although at least one test had a failed accelerometer block that was not detected in between tests.

The natural frequencies of the system correspond to the peaks in the frequency response functions (FRF's) between the radial accelerations measured around the tire and the table excitation acceleration. During the experiments, the data for the input acceleration of the table and the output accelerations at different locations on the tire were acquired by using two different data acquisition systems that had slightly different sampling rates. Without taking this difference into account the phase of the FRF, $H(\omega)$, between the table excitation, measured from the ADOCS, and the tire excitation, measured from the SoMat, grows toward infinity as the frequency increases during the sine sweep test.

$$H(\omega) = \frac{P_{A_r(SoMat)A_T(Adocs)}}{P_{A_T(Adocs)A_T(Adocs)}} \quad (2.1)$$

In equation (2.1), $A_r(SoMat)$ is the radial acceleration of the tire, $A_T(Adocs)$ is the table acceleration, P_{XX} is the power spectral density of X , and P_{YX} is the combined power spectral density of X and Y .

In order to correct the expression given by (2.1), the author multiplied the FRF between the wheel force and the radial tire excitation from the SoMat system with the FRF between the table acceleration and the wheel force from the ADOCS system. This resulted in

$$H_{new}(\omega) = \frac{P_{A_r(SoMat)F(SoMat)}}{P_{F(SoMat)F(SoMat)}} \frac{P_{F(Adocs)A_T(Adocs)}}{P_{A_T(Adocs)A_T(Adocs)}} \quad (2.2)$$

The vertical tire force was recorded with both systems. The resulting FRF, which is given by equation 2.2, is the FRF between the table acceleration and a radial tire

acceleration. This helped correct the phase problems that occurred during the original analysis.

2.4 Analysis Procedure

To determine the mode shapes of the system, it is assumed that the damping in the system is low and that the modes do not influence each other (there is no cross coupling between the modes) (Ewins, 2000). Thus the total response of the system is the sum of all of the modes of the system and their respective amplitudes. This can be written as

$$U(\theta, t) = \sum \alpha_i A_i(\theta, t) \quad (2.3)$$

In equation (2.3), $U(\theta, t)$ is the response of different points along the circumference of the tire, $A_i(\theta, t)$ is the modal response of the system, and α_i is the contribution of the i th mode to the response.

The peaks in the FRF's are fitted to individual mass-spring-damper (single degree-of-freedom) systems with natural frequency ω_n and damping factor ζ_n . The equation of motion for a single degree-of-freedom spring-mass-damper system is

$$m\ddot{x} + c\dot{x} + kx = f(x).$$

Defining the natural frequency and damping factor as

$$\omega_n = \sqrt{\frac{k}{m}} \quad (2.4)$$

$$\zeta_n = \frac{c}{2\sqrt{km}}$$

The equation of motion can be written as

$$\ddot{x} + 2\zeta_n \omega_n \dot{x} + \omega_n^2 x = g(x) \quad (2.5)$$

After performing a Laplace transform and setting the initial conditions to zero one obtains

$$s^2 X + 2\zeta_n \omega_n sX + \omega_n^2 X = h(s) \quad (2.6)$$

Setting $s = j\omega$, leads to

$$-\omega^2 X + 2j\zeta_n \omega_n \omega X + \omega_n^2 X = h(j\omega) \quad (2.7)$$

$$\frac{X(j\omega)}{h(j\omega)} = \frac{1}{-\omega^2 + 2j\zeta_n \omega_n \omega + \omega_n^2}$$

Based on this, the contribution of each mode, is given by

$$G_n(j\omega) = \frac{1}{\omega_n^2 + 2j\kappa_n \omega \omega_n - \omega^2}, \text{ where } 0.95\omega_n < \omega < 1.05\omega_n \quad (2.8)$$

The analysis is performed over a small band of frequencies, ω , around the natural frequency, ω_n of the considered mode. The total response of the system, $H_i(j\omega)$ the FRF of the i^{th} point, is the sum of the products of mode shape coefficients, $a_{i,n}$, and the modal excitations, $G_n(j\omega)$, that is

$$H_i(j\omega) = \sum_{n=1}^{n_m} a_{i,n} G_n(j\omega) \quad (2.9)$$

where n_m is the number of modes to be determined.

Solving for the mode shape, $a_{i,n}$, one obtains

$$a_{i,n} = \frac{\overline{G_n(j\omega)}^T H_i(j\omega)}{\overline{G_n(j\omega)}^T G_n(j\omega)}, \quad n = 1, \dots, n_m \quad (2.10)$$

where $0.95\omega_n < \omega < 1.05\omega_n$, and $\overline{G_n(j\omega)}$ is the complex conjugate of $G_n(j\omega)$. This equation help obtain an average mode shape in the frequency band in question. To

determine the actual mode shape, one must minimize the error between the actual FRFs,

H_i , and the calculated FRFs, $\sum_{n=1}^{n_m} a_{i,n} G_n(j\omega)$, by varying the parameter ζ_n .

The error associated with the system is given by

$$E_{i,n} = \|H_i(j\omega) - a_{i,n} G_n(j\omega)\|, (0.95\omega_n < \omega < 1.05\omega_n) \quad (2.11)$$

For twelve frequency locations, the total error for a mode is given by

$$E_n = \sum_{i=1}^{12} E_{i,n} \quad (2.12)$$

and, considering 5 modes, the total error for each ζ_n is

$$E = \sum_{n=1}^5 \sum_{i=1}^{12} E_{i,n} . \quad (2.13)$$

The ζ_n value that gives the lowest total error is determined for all values of ω_n from 10 Hz to 200 Hz. The values of ζ_n for each ω_n are compared with those associated with the peaks from the original FRFs. Since it has been assumed that there is no cross coupling between the modes, one can work with each mode separately. The peaks from the FRFs are not at exactly the same frequency for every location around the tire, see Figure 2.3. This is due to inconsistencies in the test set up, and possibly, nonlinearities in the system. The value for ω_n that gives the lowest ζ_n near a peak from the FRFs is taken to be a mode of the system. The circles in Figure 2.3 show the candidate regions for modes of the system. The analysis helps find the optimal values for ω_n and ζ_n to get the smallest error possible. In Table 2.2, the natural frequencies for the modes and their respective damping values determined from the sine sweep tests are shown. These values

are the optimal values that minimize the error between the measured and calculated FRFs as described above.

With the natural frequencies determined, one can now look at the modes themselves. The modal amplitudes are complex values that correspond to the magnitude and the lag of the oscillating point. These can be plotted as

$$u_{i,n}(t) = |a_{i,n}| \sin(t + \phi_{i,n}) \quad (2.14)$$

where $u_{i,n}(t)$ is the radial displacement of the i^{th} point of the n^{th} mode, $a_{i,n}$ is the modal amplitude, and $\phi_{i,n}$ is the phase of $a_{i,n}$.

The sine sweep data was used to determine the natural frequencies and mode shapes in this analysis. The first five mode shapes found are shown in the next section. The first mode is a vertical rigid body mode, while the second mode is a lateral rigid body mode.

2.5 Experimental Results

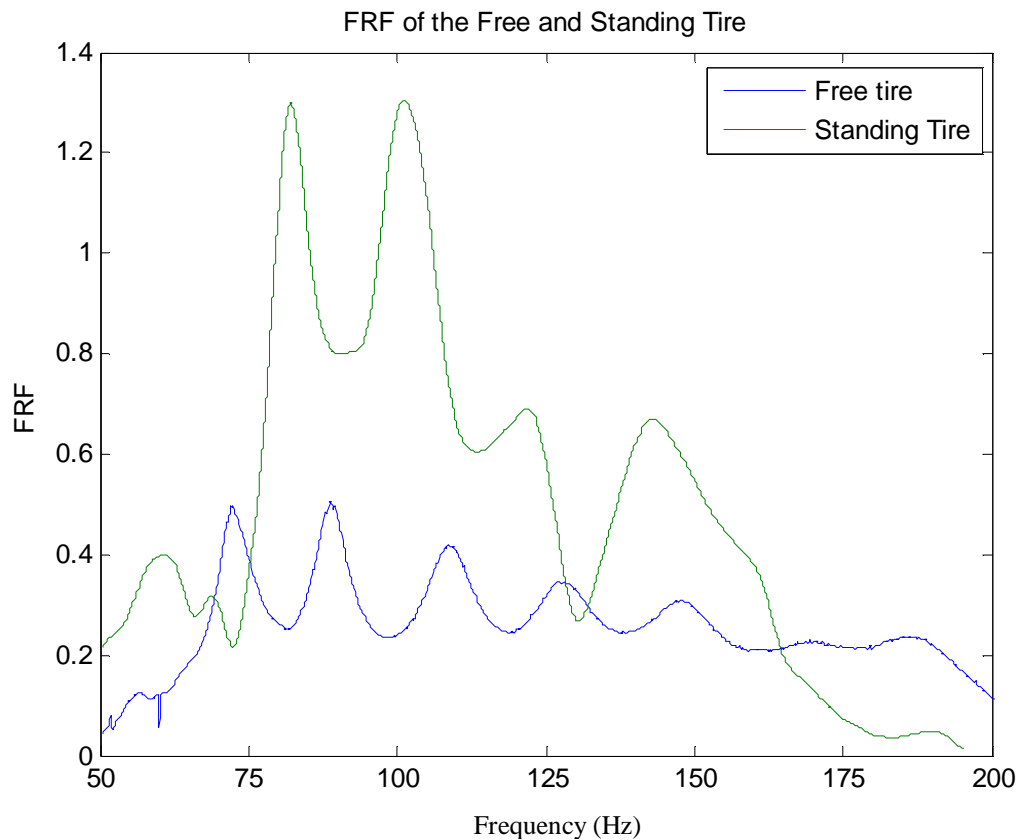


Figure 2.2: FRFs for the free and standing tire due to a modal hammer impulse

In Figure 2.2, a representative FRF is shown for the free tire for an input radial force from a modal hammer. The overall response for the free tire tests was insufficient to perform effective, complete modal analyses, since the input force from the modal hammer was too low to excite the entire tire. The free tire FRF has distinct peaks at steady intervals. These peaks correspond to the modes of the system. The standing tire does not have the same shape and it is clear that the peaks for the standing tire FRF do not match up with the peaks from the free tire FRF. If one uses the mode numbering scheme from Zegelaar (1997), the modes for the standing tire would all be half modes.

Table 2.2: Natural frequencies and damping factors associated with the first five modes found through

Mode	30psi	50psi	ζ (50psi)
1	33 Hz	34 Hz	0.06563
2	38Hz	40 Hz	0.11100
3	54 Hz	64 Hz	0.09919
4	72 Hz	80 Hz	0.03819
5	90 Hz	100 Hz	0.04678

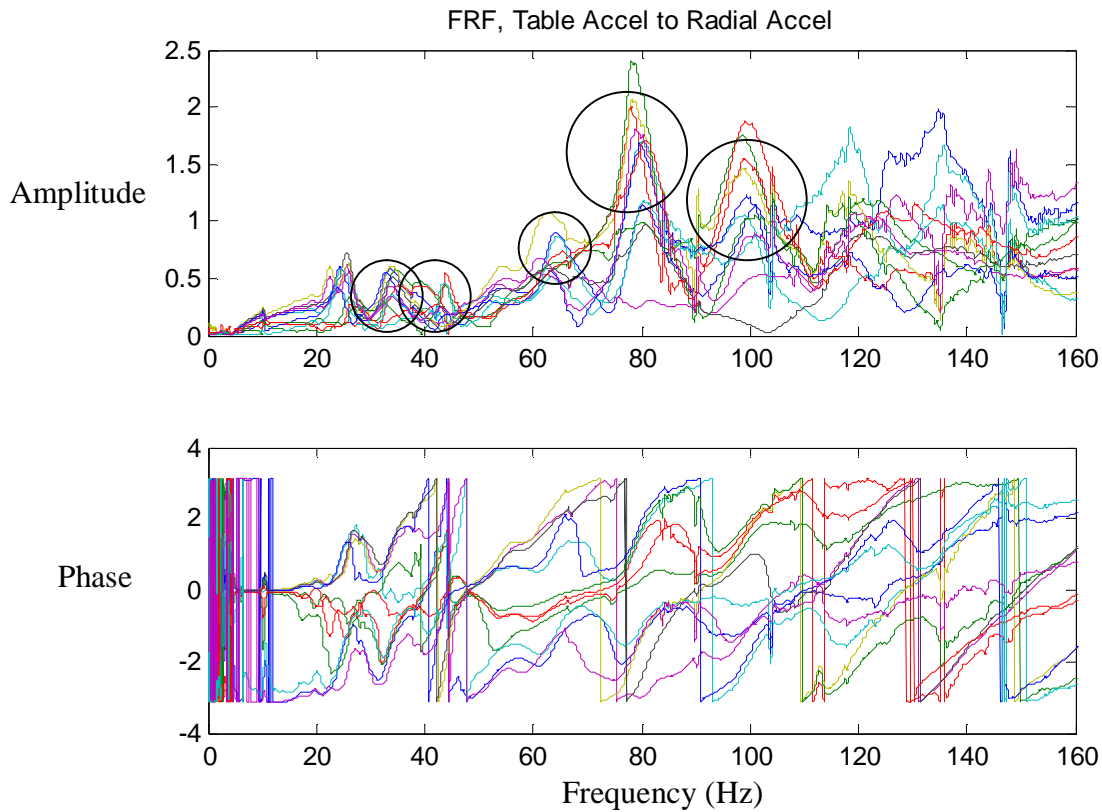


Figure 2.3: FRF of the radial acceleration to the input table acceleration. The circles show the areas of potential natural frequencies. Sine sweep test for the standing tire ($F_z=9000$ N) at 50 psi. Twelve different color plots are shown for the twelve accelerometers used in the experiments.

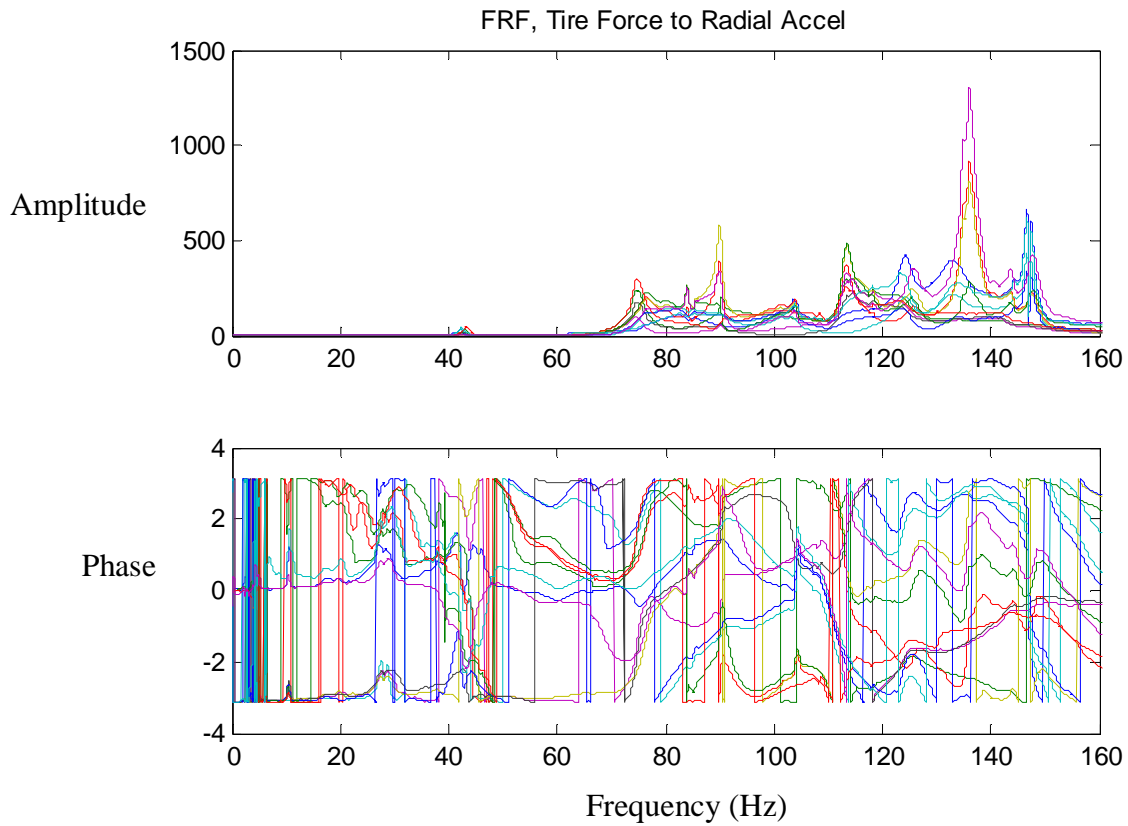


Figure 2.4: FRF of radial acceleration to vertical tire force. Sine sweep test for the standing tire ($F_z=9000$ N) at 50psi. Twelve different color plots are shown for the twelve accelerometers used in the experiments.

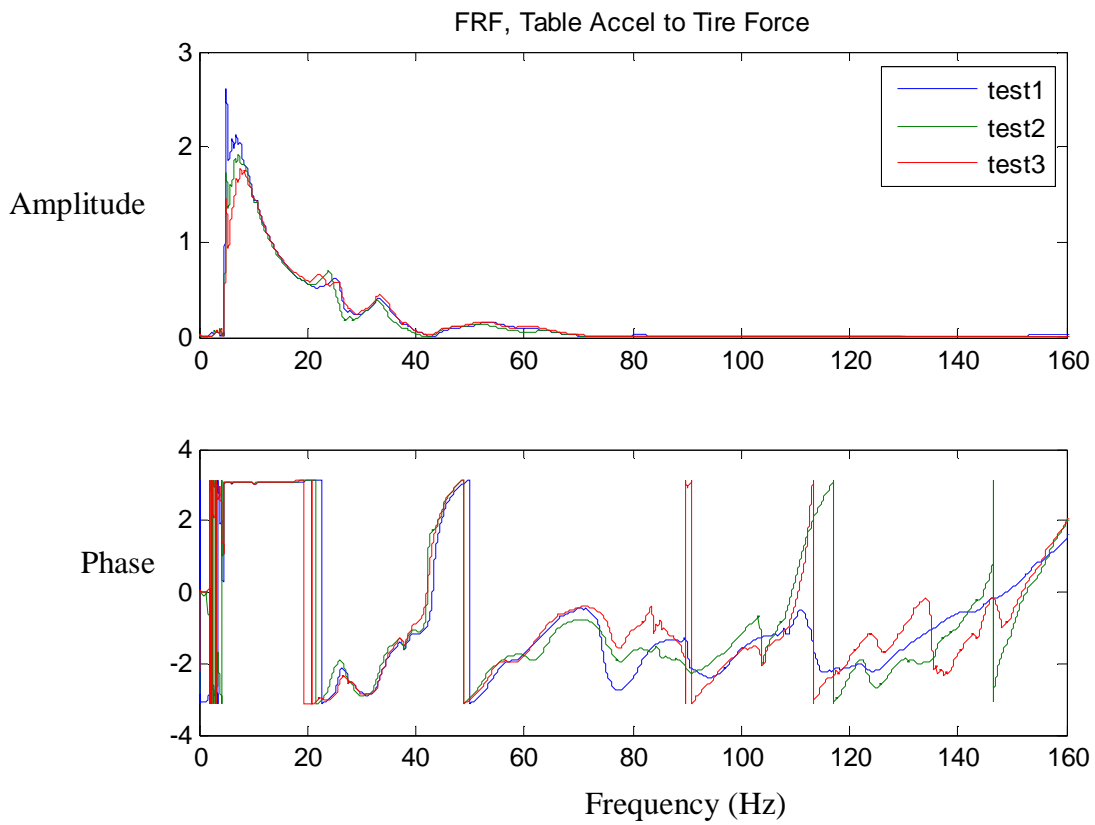


Figure 2.5: FRF of vertical tire force to table acceleration. Sine sweep test for the standing tire ($F_z=9000$ N) at 50psi. The three colors correspond to three different runs.

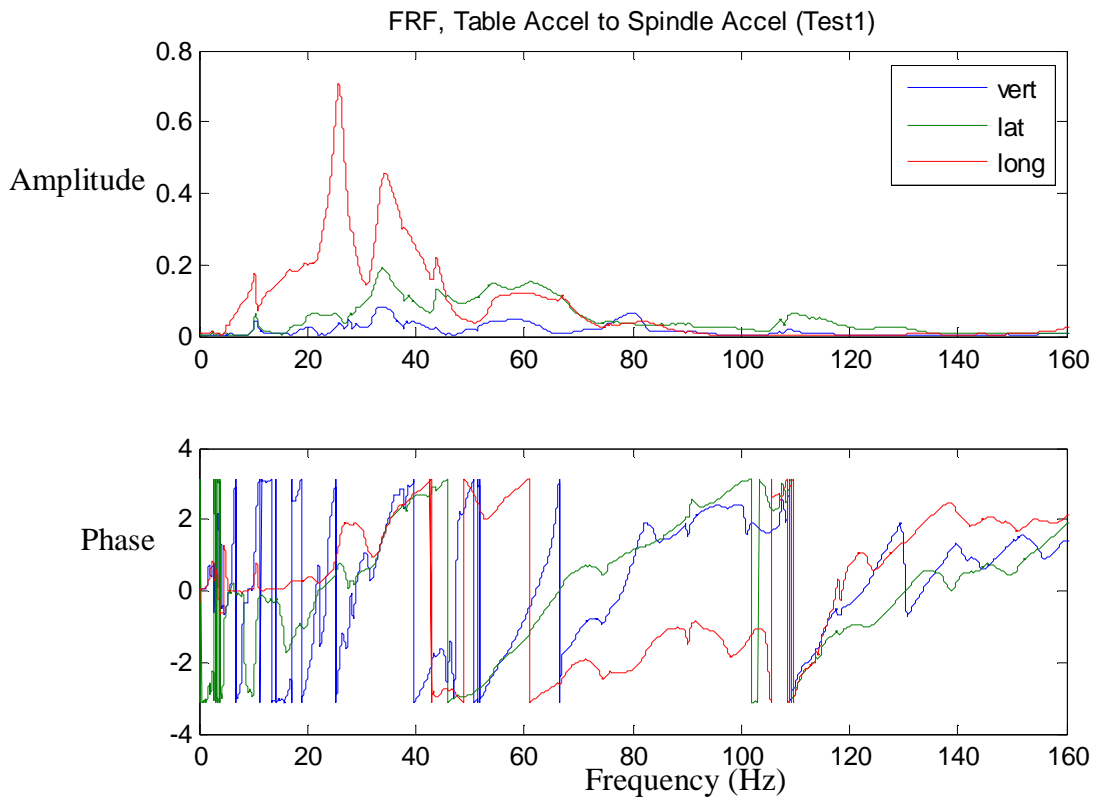


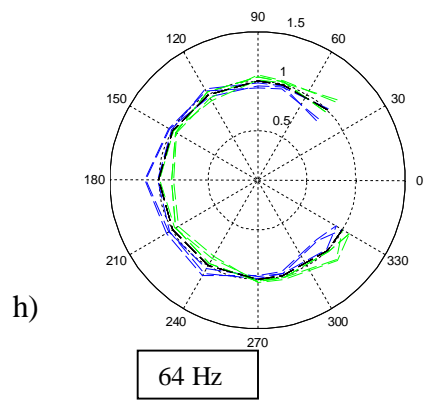
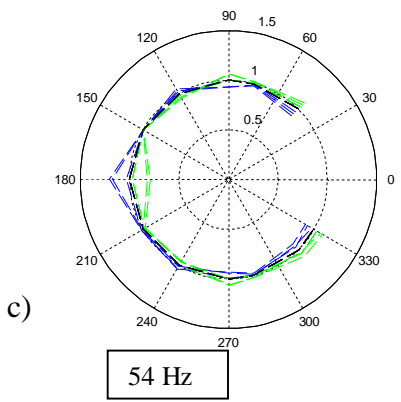
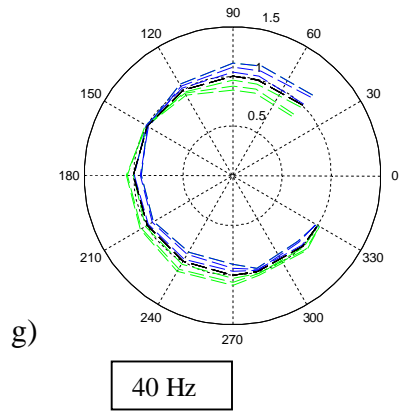
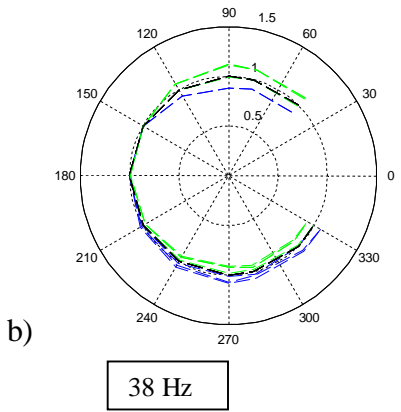
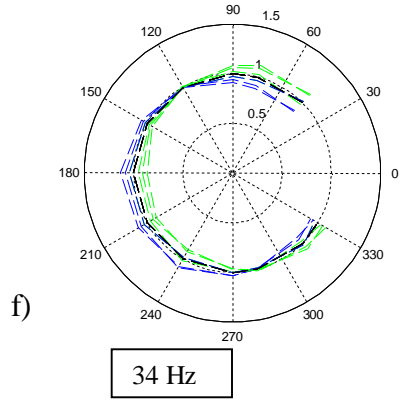
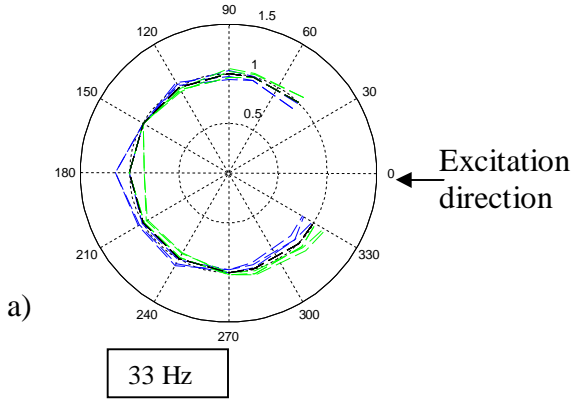
Figure 2.6: FRF of spindle acceleration to table acceleration. Sine sweep test for the standing tire ($F_z=9000$ N) at 50psi. The three different color plots correspond to three different accelerometer orientations.

In Figures 2.3 to 2.6, the frequency-response functions for various combinations of input and output measurements are shown. In Figure 2.3, the frequency-response functions that were obtained in the experimental model analyses are shown. Each FRF corresponds to a particular radial acceleration measurement on the tire and the table acceleration input from the shaker table. The sampling rate for all of the data channels was set to be 1000 Hz. The FRFs were calculated using the “tfestimate” command in MatLab. This command takes averages and is windowed using a Hamming window (MatLab, 2005).

Mode shapes of a heavily loaded tire.

30 psi

50 psi



30 psi

50 psi

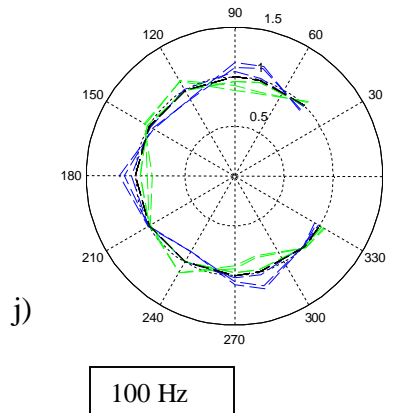
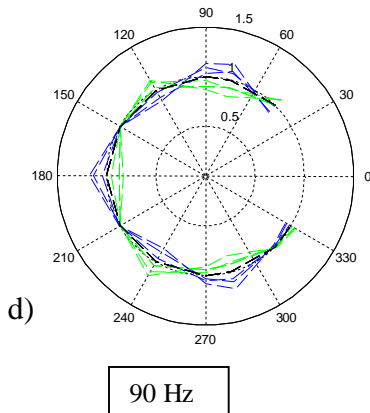
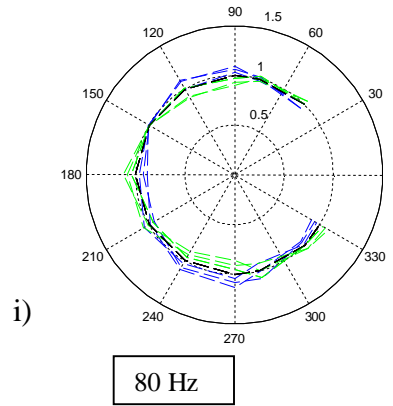
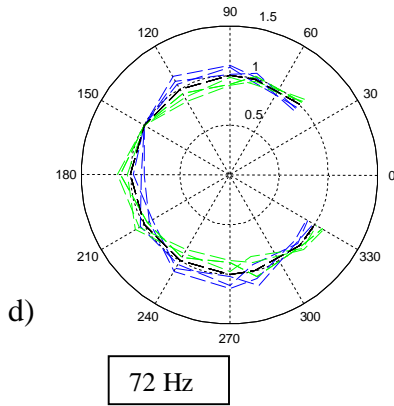


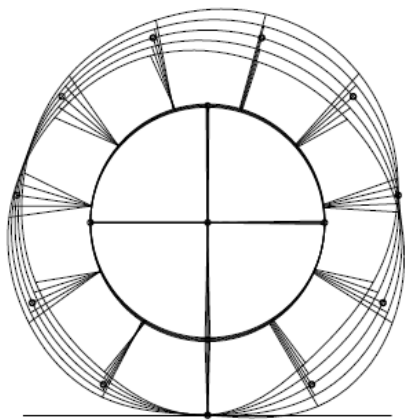
Figure 2.7: Mode Shapes for the standing tire ($F_z=9000N$). Sine sweep test. The two colors show the extremes of the mode shapes as it expands (one color) and contracts (the other)

In Figure 2.7, the rigid body modes and the first three flexible modes for the heavily loaded tire that is excited in the radial direction are shown for two different tire pressures, 30 psi and 50 psi. The arrow shows the direction of the input harmonic force corresponding with the vertical orientation of the tire. The first mode shown at 33Hz is a vertical rigid body mode while the next at 38 Hz is a horizontal rigid body mode. The

horizontal mode is unexpected given that the input force is limited to the vertical direction. The next three modes correspond to the first three flexible modes of the tire. The first mode, at 54 Hz, is fairly hard to make out but it corresponds to a $1\frac{1}{2}$ mode (94.1 Hz) from Zegelaar's work, shown for comparison in Figure 2.8. The 2nd mode, 72 Hz, is much easier to make out and this corresponds to a $2\frac{1}{2}$ mode (125.7 Hz) of Zegelaar (1997). The third mode at 90 Hz corresponds to a $3\frac{1}{2}$ mode (156.8 Hz) of Zegelaar (1997). The modes for the passenger tire are at frequencies nearly double those seen for the heavily loaded tire. The passenger tire analyses do not pick up the rigid body modes that this thesis analyses did for the heavily loaded tire.

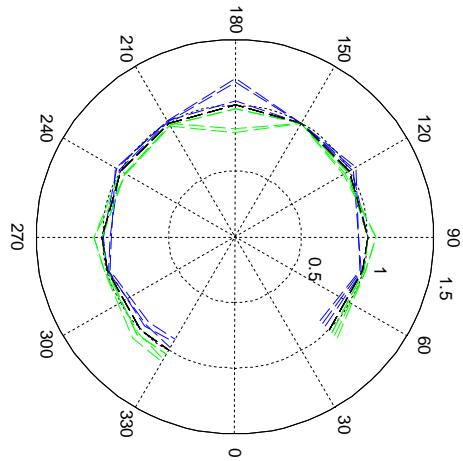
The modes for the passenger tire analyzed by Zegelaar (1997) are at significantly higher frequencies than those observed for the much stiffer and heavier tire considered in this thesis. The modes shown below are the results obtained by Zegelaar for a standing passenger tire.

**Passenger Tire,
Fz=4000N**

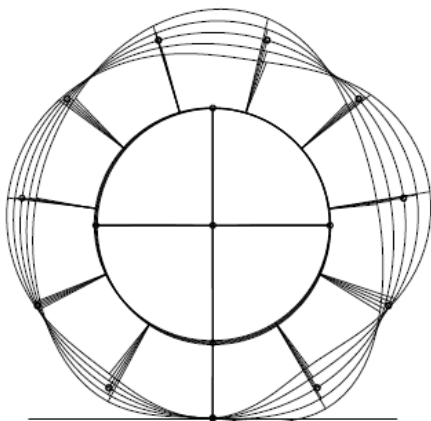


$$n = 1\frac{1}{2}, f = 94.1Hz$$

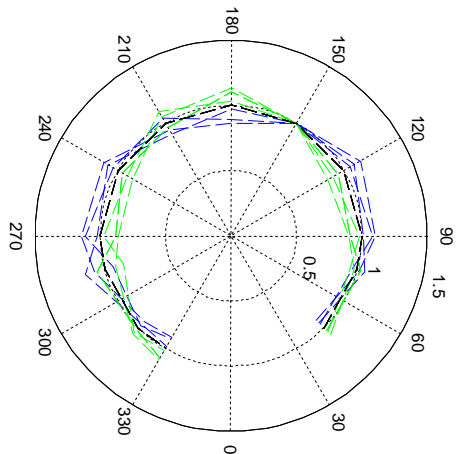
**Heavily Loaded Tire,
Fz=9000N**



$$n = 1\frac{1}{2}, f = 54Hz$$



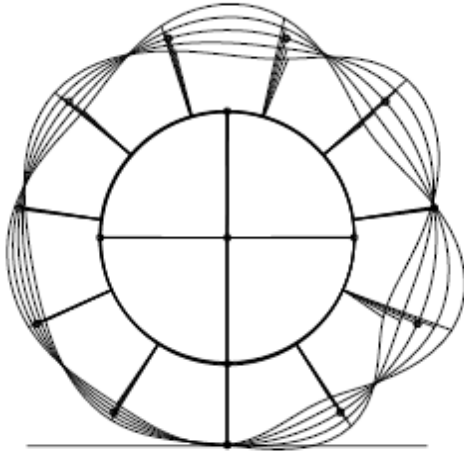
$$n = 2\frac{1}{2}, f = 125.7Hz$$



$$n = 2\frac{1}{2}, f = 72Hz$$

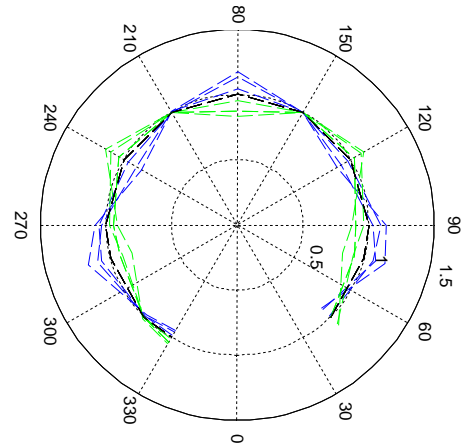
Figure 2.8: Comparison of passenger tire modes and heavily loaded vehicle tire modes

**Passenger Tire,
 $F_z=4000\text{N}$**



$$n = 3\frac{1}{2}, \quad f = 156.8\text{Hz}$$

**Heavily Loaded Tire,
 $F_z=9000\text{N}$**



$$n = 3\frac{1}{2}, \quad f = 90\text{Hz}$$

Figure 2.8 (continued): Comparison of passenger tire modes and heavily loaded vehicle tire modes

In Figure 2.9, the tangential mode shapes are shown. The tangential modes are harder to see than the radial modes. The tangential modes for the passenger car tire found by Yam *et al.* (2000), shown back in Figure 1.4, resemble slightly distorted versions of the radial modes. The modes found for the heavily loaded vehicle tire follow this trend, although they are more distorted. There are no rigid body modes present and the second modes shown, Figure 2.9 b and h, are discernible leaf modes with elongation in one direction and then in another direction orthogonal to the first. Further analysis into the mode shapes in the tangential and lateral directions is needed as all of the mode shapes are not clearly discernible.

In Figure 2.10, the FRFs between the tangential accelerations at different locations around the tire and the input table accelerations are shown. The FRFs for the tangential response contain much more noise than those for the radial response. This is especially noticeable in the phase plots for the FRFs. In Figure 2.11, the FRFs between the lateral accelerations at different points around the tire and the input table accelerations are shown. The frequencies of the first few flexible modes in the tangential and lateral directions start around 50-60 Hz. This is similar to the frequencies at which the modes for the radial direction were observed. In comparison to the tangential and lateral modes found by Yam *et al.* that started around 120 Hz, as shown in Figure 1.4.

Tangential (Longitudinal) Modes

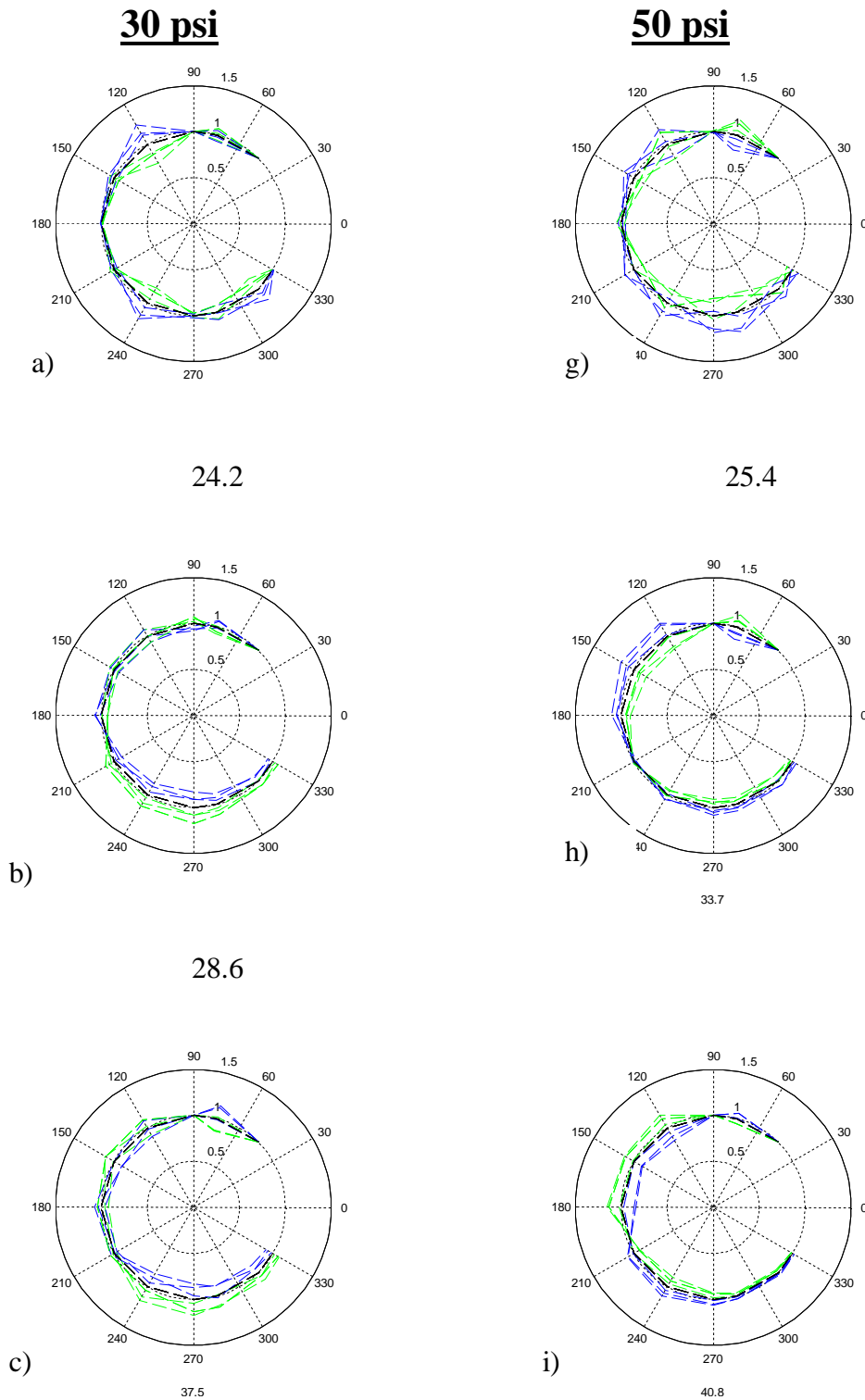


Figure 2.9: Tangential Mode Shapes for the standing tire ($F_z=9000\text{N}$). Sine sweep test.

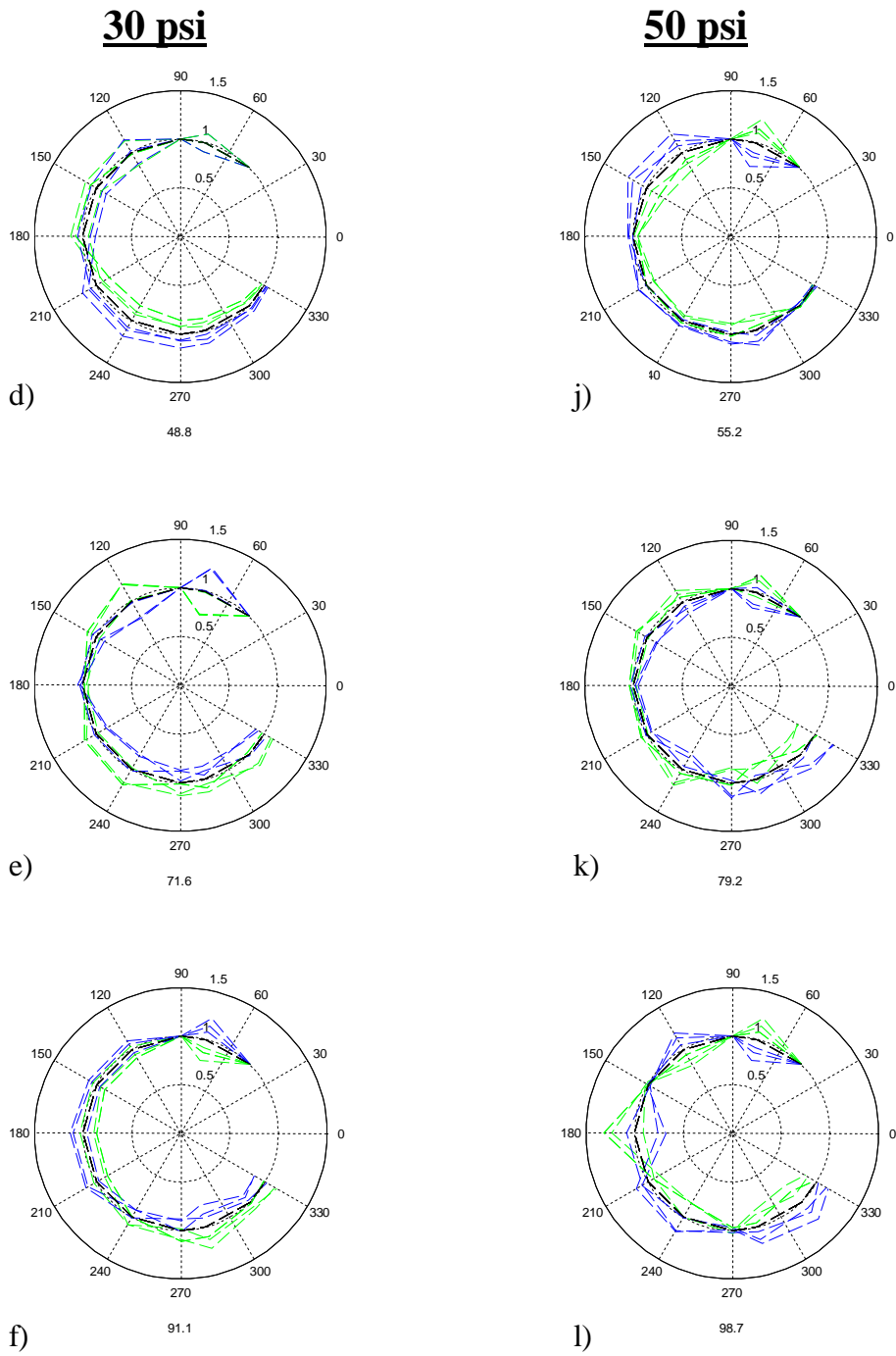


Figure 2.9 (continued): Tangential Mode Shapes for the standing tire ($F_z=9000\text{N}$). Sine sweep test.

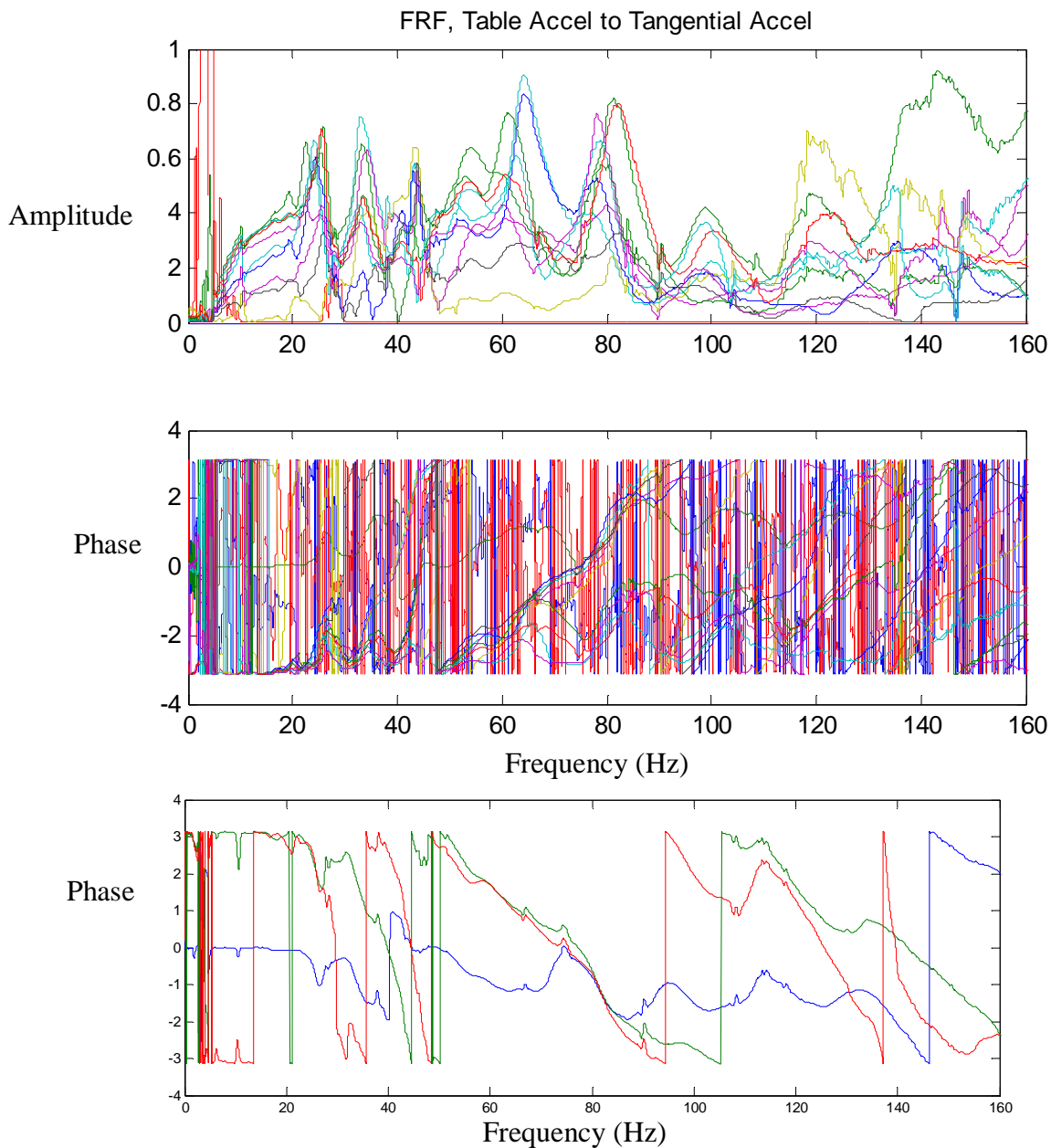


Figure 2.10: FRFs of tangential acceleration at different tire locations to table acceleration. Sine sweep test for the standing tire ($F_z=9000$ N) at 50psi. The different accelerometer locations around the tire are shown by a different color in the figure. All twelve sensor locations are present in the plot. The figure below shows the Phase of the FRF for only 3 points around the tire. The noisy channels were removed to give a clearer picture.

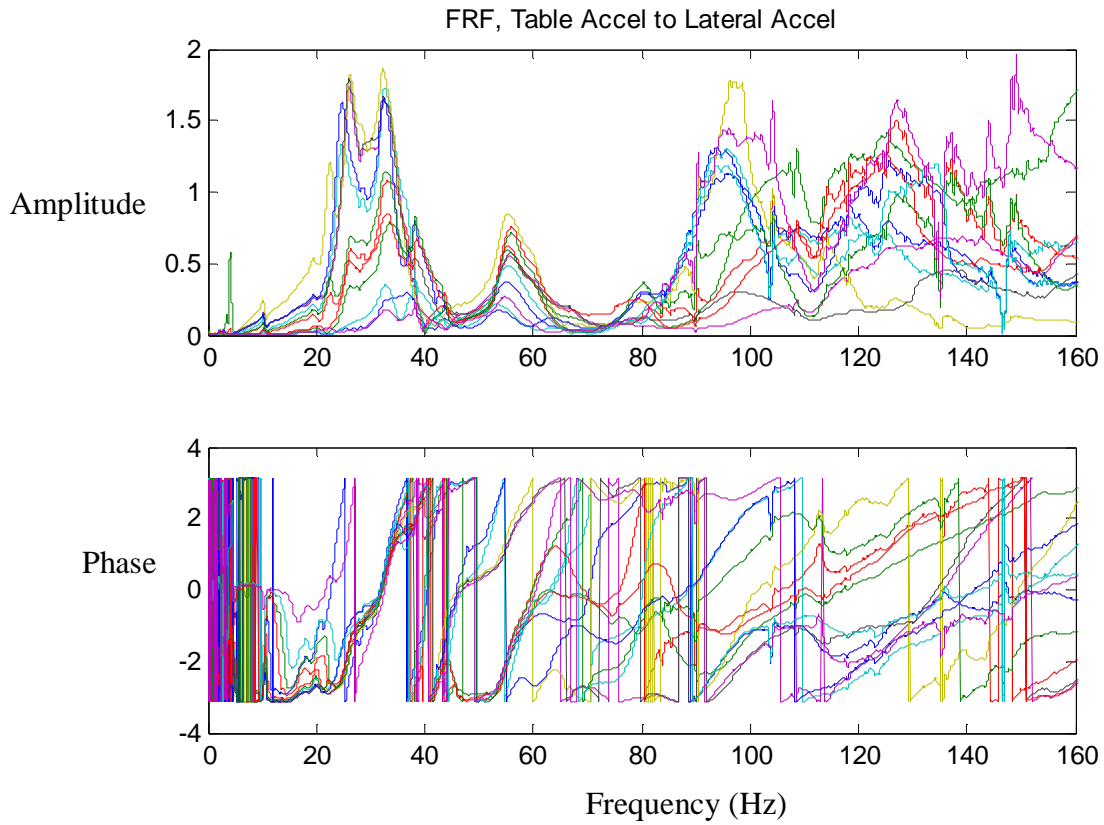


Figure 2.11: FRFs of lateral acceleration at different tire locations to table acceleration. Sine sweep test for the standing tire ($F_z=9000$ N) at 50psi. The different accelerometer locations around the tire are shown by a different color in the figure. All twelve sensor locations are present in the plot.

Chapter 3

Modeling Efforts and Comparisons with Experimental Results

In this chapter, a flexible ring model is used to make predictions and these predictions are compared with the experimental results presented in Chapter 2. Nonlinear terms are added to the flexible ring model and the resulting dynamics is studied to explain some of the observations made in the experiments. The comparisons made between the predicted modal response of the flexible ring model and the experimental results for the heavily loaded vehicle tire are used to try to identify nonlinear characteristics in the heavily loaded tire dynamics

3.1 Flexible Ring Model

As discussed in Chapter 1, the flexible ring model being used in this analysis was proposed by Gong (1993) and it takes the form

$$\frac{EI}{R^4} \left(\frac{\partial^3 w_b}{\partial \theta^3} - \frac{\partial^2 v_b}{\partial \theta^2} \right) - \frac{EA}{R^2} \left(\frac{\partial w_b}{\partial \theta} + \frac{\partial^2 v_b}{\partial \theta^2} \right) + c_{bv} v_b + \rho A \ddot{v}_b = 0$$
$$\frac{EI}{R^4} \left(\frac{\partial^4 w_b}{\partial \theta^4} - \frac{\partial^3 v_b}{\partial \theta^3} \right) + \frac{EA}{R^2} \left(w_b + \frac{\partial v_b}{\partial \theta} \right) + \frac{p_0 b_R}{R} \left(-\frac{\partial^2 w_b}{\partial \theta^2} - w_b \right) + c_{bw} w_b + \rho A \ddot{w}_b = 0 \quad (3.1)$$

where the parameters are as defined in Chapter 1.

For the modal analysis, the flexible ring model is used along with an added damping term, which in some cases has a complex component. The results are obtained by solving for the responses of the partial differential equations describing the flexible ring when it is subjected to a sine sweep input at the bottom edge of the tire. This represents the experimental setup where the tire is loaded by a plate in the vertical direction. The output response is then analyzed with the input sine function just as the experiment data were analyzed, by using a single degree-of-freedom system to fit a curve to every point around the tire in order to determine the modal amplitudes.

The partial differential equation from the flexible ring model was solved by using the MATLAB function “pdepe.” In MATLAB, the initial-boundary value problem for the parabolic PDE is solved in one dimension by using an iterative solver of the strong-form equation (MATLAB, 2005). The “pdepe” solver converts the PDEs to ODEs by using a second-order accurate spatial discretization method. The time integration is done with the function ode15s. After discretization, the elliptical partial-differential equations are converted to algebraic equations. The solver is an iterative solver that uses numerical time integration to determine the response of the system.

The function pdepe solves PDEs of the form described below:

$$c\left(x, t, u, \frac{\partial u}{\partial x}\right) \frac{\partial u}{\partial t} = x^{-m} \frac{\partial}{\partial x} \left(x^m f\left(x, t, u, \frac{\partial u}{\partial x}\right) \right) + s\left(x, t, u, \frac{\partial u}{\partial x}\right) \quad (3.2)$$

with the initial conditions

for $t = t_0$ and all x ; that is,

$$u(x, t_0) = u_0(x) \quad (3.3)$$

For all t and either $x=a$ or $x=b$, the solution satisfies the boundary conditions of the form:

$$p(x, t, u) + q(x, t) f\left(x, t, u, \frac{\partial u}{\partial x}\right) = 0 \quad (3.4)$$

The function pdepe solves PDEs involving first derivatives of time and up to second derivatives of space. The equations of motion for the flexible ring model include second derivatives of time and fourth derivatives of space. These terms must be reduced to first derivatives of time and, at most, second derivatives of space before they can be substituted into the “pdepe” function. In order to reduce the order of the equations, one must introduce a couple of new variables. The value of m in equation (3.2) is zero in this analysis.

For this analysis, five variables will be used as follows:

$$u_1 = v_b \quad (3.5 \text{ a})$$

$$u_2 = \frac{\partial v_b}{\partial t} \quad (3.5 \text{ b})$$

$$u_3 = w_b \quad (3.5 \text{ c})$$

$$u_4 = \frac{\partial w_b}{\partial t} \quad (3.5 \text{ d})$$

$$u_5 = \frac{\partial^2 w_b}{\partial \theta^2} - \frac{\partial v_b}{\partial \theta} \quad (3.5 \text{ e})$$

The equations of motion (equation 3.1) in terms of the variables \mathbf{u} transform to the following five equations, which are first order in time and at most second order in space in terms of the respective derivatives.

$$u_2 = \frac{\partial u_1}{\partial t} \quad (3.6 \text{ a})$$

$$\frac{EI}{R^4} \left(\frac{\partial u_5}{\partial \theta} \right) - \frac{EA}{R^2} \left(\frac{\partial u_3}{\partial \theta} + \frac{\partial^2 u_1}{\partial \theta^2} \right) + c_{bv} u_1 + \rho A \frac{\partial u_2}{\partial t} = 0 \quad (3.6 \text{ b})$$

$$u_4 = \frac{\partial u_3}{\partial t} \quad (3.6 \text{ c})$$

$$\frac{EI}{R^4} \left(\frac{\partial^2 u_5}{\partial \theta^2} \right) + \frac{EA}{R^2} \left(u_3 + \frac{\partial u_1}{\partial \theta} \right) + \frac{p_0 b_R}{R} \left(-\frac{\partial^2 u_3}{\partial \theta^2} - u_3 \right) + c_{bw} u_3 + \rho A \frac{\partial u_4}{\partial t} = 0 \quad (3.6 \text{ d})$$

$$u_5 = \frac{\partial^2 u_3}{\partial \theta^2} - \frac{\partial u_1}{\partial \theta} \quad (3.6 \text{ e})$$

The coefficients, initial conditions, and boundary conditions to be used in equation (3.2) for “pdepe” are as follows:

$$c = \begin{bmatrix} 1 \\ \rho A \\ 1 \\ \rho A \\ 0 \end{bmatrix} \quad (3.7)$$

$$f = - \begin{bmatrix} 0 \\ \frac{EA}{R^2} \frac{\partial u_1}{\partial \theta} \\ 0 \\ \frac{EI}{R^4} \frac{\partial u_5}{\partial \theta} - \frac{p_0 b_R}{R} \frac{\partial u_3}{\partial \theta} \\ \frac{\partial u_3}{\partial \theta} \end{bmatrix} \quad (3.8)$$

$$s = - \begin{bmatrix} -u_2 \\ \frac{EI}{R^4} \frac{\partial u_5}{\partial \theta} - \frac{EA}{R^2} \frac{\partial u_3}{\partial \theta} + c_{bv} u_1 \\ -u_4 \\ \frac{EA}{R^2} u_3 - \frac{p_0 b_R}{R} u_3 + c_{bw} u_3 + \frac{EA}{R^2} \frac{\partial u_1}{\partial \theta} \\ -u_5 - \frac{\partial u_1}{\partial \theta} \end{bmatrix} \quad (3.9)$$

The boundary conditions corresponding to the experiments of Chapter 2 read as follows:

$$v_b(5^\circ) = v_b(355^\circ) = 0 \quad (3.10a)$$

$$\dot{v}_b(5^\circ) = \dot{v}_b(355^\circ) = 0 \quad (3.10b)$$

$$w_b(5^\circ) = w_b(355^\circ) = 0.01 * \sin(2\pi t(\alpha t + d)) - 0.03 \quad (3.10c)$$

$$\dot{w}_b(5^\circ) = \dot{w}_b(355^\circ) = 0.01 * \cos(2\pi t(\alpha t + d))(2\pi(\alpha t + d) + 2\pi t \alpha) \quad (3.10d)$$

$$\frac{\partial w_b(5^\circ)}{\partial \theta} = \frac{\partial w_b(355^\circ)}{\partial \theta} = 0 \quad (3.10e)$$

The initial conditions are written as

$$w_b(5^\circ, 0) = w_b(355^\circ, 0) = -0.03 \quad (3.11a)$$

$$\dot{w}_b(5^\circ, 0) = \dot{w}_b(355^\circ, 0) = 0.01 * 2\pi d \quad (3.11b)$$

For all other θ

$$v_b(\theta, 0) = \dot{v}_b(\theta, 0) = w_b(\theta, 0) = \dot{w}_b(\theta, 0) = 0 \quad (3.11c)$$

For the MATLAB code, the initial and boundary conditions are constructed as shown below.

Initial conditions:

$$u(5^\circ, t_0) = u(355^\circ, t_0) = \begin{bmatrix} 0 \\ 0 \\ -0.03 \\ 0.01 * 2\pi d \\ 0 \end{bmatrix} \quad (3.12a)$$

$$u(x, t_0) = u(x, t_0) = \begin{bmatrix} 0 \\ 0 \\ 0 \\ 0 \\ 0 \end{bmatrix} \quad (3.12b)$$

Boundary conditions:

$$p(5^\circ t, u) = \begin{bmatrix} u_1(x = 5^\circ) \\ u_2(x = 5^\circ) \\ u_3(x = 5^\circ) - 0.01 * \sin(2\pi t(\alpha t + d)) + 0.03 \\ u_4(x = 5^\circ) - 0.01 * \cos(2\pi t(\alpha t + d))(2\pi(\alpha t + d) + 2\pi t \alpha) \\ 0 \end{bmatrix} \quad (3.13a)$$

$$p(355^\circ t, u) = \begin{bmatrix} u_1(x=355^\circ) \\ u_2(x=355^\circ) \\ u_3(x=355^\circ) - 0.01 * \sin(2\pi(\alpha t + d)) + 0.03 \\ u_4(x=355^\circ) - 0.01 * \cos(2\pi(\alpha t + d))(2\pi(\alpha t + d) + 2\pi\alpha) \\ 0 \end{bmatrix} \quad (3.13b)$$

$$q(5^\circ t, u) = q(355^\circ t, u) = \begin{bmatrix} 0 \\ 0 \\ 0 \\ 0 \\ 1 \end{bmatrix} \quad (3.13c)$$

For $\theta = 5^\circ$

$$\begin{bmatrix} u_1(x=5^\circ) \\ u_2(x=5^\circ) \\ u_3(x=5^\circ) - 0.01 * \sin(2\pi(\alpha t + d)) + 0.03 \\ u_4(x=5^\circ) - 0.01 * \cos(2\pi(\alpha t + d))(2\pi(\alpha t + d) + 2\pi\alpha) \\ 0 \end{bmatrix} + \begin{bmatrix} 0 \\ 0 \\ 0 \\ 0 \\ 1 \end{bmatrix} \cdot \begin{bmatrix} 0 \\ -\frac{EA \partial u_1}{R^2 \partial \theta} \\ 0 \\ \frac{EI \partial u_5}{R^4 \partial \theta} - \frac{p_0 b_R}{R} \frac{\partial u_3}{\partial \theta} \\ \frac{\partial u_3}{\partial \theta} \end{bmatrix} = \begin{bmatrix} 0 \\ 0 \\ 0 \\ 0 \\ 0 \end{bmatrix} \quad (3.13d)$$

For $\theta = 355^\circ$

$$\begin{bmatrix} u_1(x=355^\circ) \\ u_2(x=355^\circ) \\ u_3(x=355^\circ) - 0.01 * \sin(2\pi(\alpha t + d)) + 0.03 \\ u_4(x=355^\circ) - 0.01 * \cos(2\pi(\alpha t + d))(2\pi(\alpha t + d) + 2\pi\alpha) \\ 0 \end{bmatrix} + \begin{bmatrix} 0 \\ 0 \\ 0 \\ 0 \\ 1 \end{bmatrix} \cdot \begin{bmatrix} 0 \\ -\frac{EA \partial u_1}{R^2 \partial \theta} \\ 0 \\ \frac{EI \partial u_5}{R^4 \partial \theta} - \frac{p_0 b_R}{R} \frac{\partial u_3}{\partial \theta} \\ \frac{\partial u_3}{\partial \theta} \end{bmatrix} = \begin{bmatrix} 0 \\ 0 \\ 0 \\ 0 \\ 0 \end{bmatrix} \quad (3.13e)$$

The points around the circumference of the tire are discretized into a set of one hundred and one equally distributed points around the tire starting at 5° from the bottom of the tire and ending at 355° from the bottom of the tire. The gap in the solution at the bottom of

the tire mimics the contact patch where the tire is loaded by the ground (or test fixture). The MATLAB file used to perform these analyses and the coefficients used are provided in the Appendix.

The initial and boundary conditions presented above describe a fixed sine sweep input at the bottom of the tire that takes the form

$$u = 0.01\sin(2\pi t(\alpha t + d)) - 0.03 \quad (3.14)$$

The sine sweep has amplitude of .01 meters, and this sweep has an initial loaded offset of .03 meters. The variables α and d are varied throughout the test runs in order to excite the desired range of frequencies.

An attempt was also made to analyze the flexible ring model with added damping and nonlinear stiffness terms. Damping terms took the form

$$f = K_d \dot{w}_b \quad (3.15)$$

where K_d is the damping coefficient, which could take real or imaginary values.

Nonlinear cubic stiffness terms took the form

$$f = K_n w_b^3 \quad (3.16)$$

where K_n is the stiffness coefficient and took strictly real values.

These additional terms were added to the Matlab function in the “s” coefficient in equation (3.9). The new “s” coefficient reads as

$$s = \begin{bmatrix} \frac{EI}{R^4} \frac{\partial u_5}{\partial \theta} - \frac{EA}{R^2} \frac{\partial u_3}{\partial \theta} + c_{bv} u_1 \\ -u_4 \\ \frac{EA}{R^2} u_3 - \frac{p_0 b_R}{R} u_3 + c_{bv} u_3 + \frac{EA}{R^2} \frac{\partial u_1}{\partial \theta} + Ku_4 \\ -u_5 - \frac{\partial u_1}{\partial \theta} \end{bmatrix} \quad (3.17a)$$

with the damping terms, and as

$$s = \begin{bmatrix} \frac{EI}{R^4} \frac{\partial u_5}{\partial \theta} - \frac{EA}{R^2} \frac{\partial u_3}{\partial \theta} + c_{bv} u_1 \\ -u_4 \\ \frac{EA}{R^2} u_3 - \frac{p_0 b_R}{R} u_3 + c_{bv} u_3 + \frac{EA}{R^2} \frac{\partial u_1}{\partial \theta} + Ku_3^3 \\ -u_5 - \frac{\partial u_1}{\partial \theta} \end{bmatrix} \quad (3.17b)$$

with the cubic stiffness terms.

3.2 Parameters and Numerical Solution

Table 3.1: Parameters used in model studies following Zegelaar (1997)

parameter	symbol	value	unit
bending stiffness tire ring	EI	4.0	N m^2
extensional stiffness tire ring	EA	$4.9 \cdot 10^6$	N
tire ring radius	R	0.300	m
inside tire width	b_0	0.152	m
inflation pressure	p_0	$2.2 \cdot 10^5$	N/m^2
tangential sidewall stiffness	c_{bv}	$6.49 \cdot 10^5$	N/m^2
radial sidewall stiffness	c_{bw}	$1.93 \cdot 10^6$	N/m^2
horizontal tread stiffness	c_{cx}	$25 \cdot 10^6$	N/m^2
vertical tread stiffness	c_{cz}	$75 \cdot 10^6$	N/m^2
moment of inertia rim	I_{ay}	0.35	kg m^2
mass density tire ring	ρA	3.81	kg/m
half the contact length	a	0.0535	m
number of tread elements	n_e	100	-
number of modes	n_m	30	-

In Table 3.1, the parameters used for these analyses are shown. These are the same as those used by Zegelaar (1997) for a passenger vehicle tire. The author was unable to determine accurate values for many parameters for the heavily loaded tire. Since the parameter values do not correspond to the heavily loaded tire of this analysis,

the goal is to carry out a qualitative comparison with the experimental results showed earlier. The frequencies of the modes are not expected to match up, but the mode shapes and the general profile of the frequency response functions may.

The analysis was attempted by using the flexible ring model with only the radial direction terms. These attempts showed results that were not reasonable for the system in question. This analysis showed that the flexible ring model is not valid for only one variable when the tangential displacement is neglected.

If the errors that accumulated during the experiment had been handled better, the spread of the FRFs could have come out looking more like those of the analytical model. It is easy to pick out the peaks of the FRFs for the flexible ring model since there are no errors stemming from the test setup and the orientations of all measured points around the tire are identical. The sharp peaks in the flexible ring model also suggest that the actual tire system has a significantly larger amount of damping.

In most modal experiments, the phase values at the peaks of the FRFs and the output response tend to be around 90. The fact that the phase of the FRFs for the experimental data are spread over the entire phase band and was not around 90 degrees suggest that there may be complex damping in the system that could spread the phase response (Ewins, 2000).

3.3 Model Results

In this section, the results obtained from the MATLAB PDE solver are shown for the flexible ring model when it is excited by a harmonic excitation at the base of the tire.

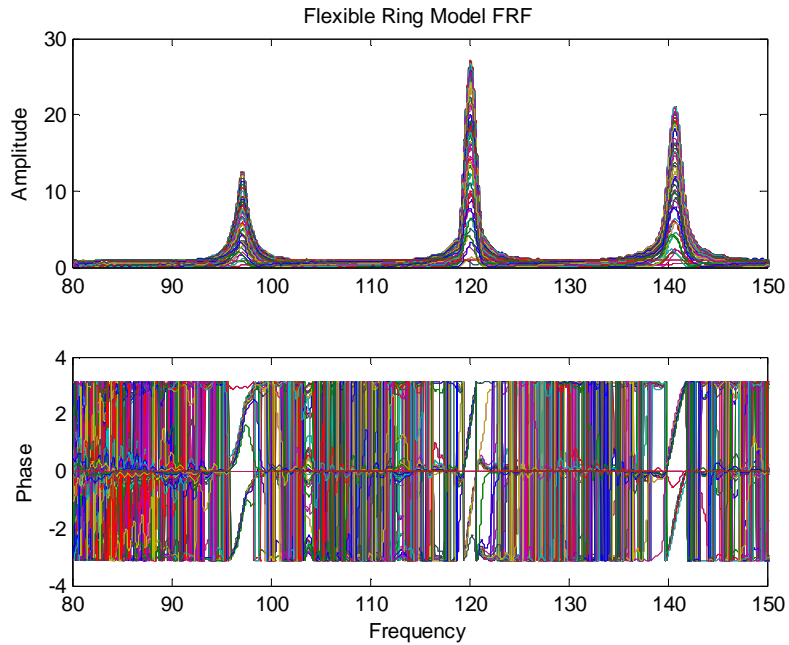
The modal response is obtained for the basic flexible ring model as well as for the flexible ring model with added real damping, complex damping, and cubic stiffness terms. The FRFs between the radial displacements at multiple locations around the tire and the input displacements at the base of the tire are obtained and presented.

In Figure 3.1, the modal response for the flexible ring model with no damping is shown. The flexible modes shapes for the flexible ring model with no damping are shown in Figure 3.2. In Figures 3.3, 3.4, and 3.5 the modal response FRFs for the flexible ring model with added complex damping, combined damping, and cubic stiffness terms respectively are shown.

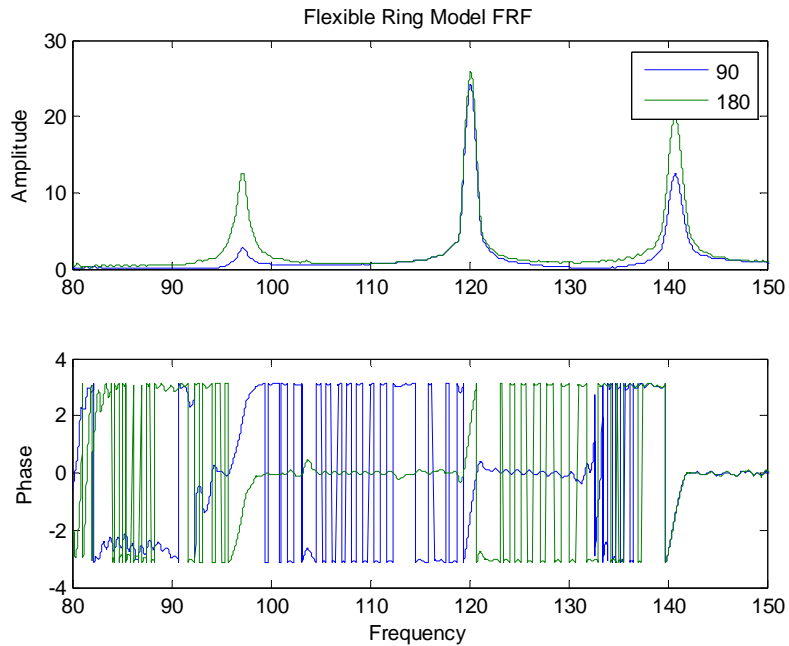
In Table 3.2, a summary of the systems solved is shown. The nature and amplitude of the nonlinear terms, the frequency range solved, and the frequencies of the first three modes are presented. The flexible ring model system with regular damping of magnitude $1.0E+4$ Ns/m is over damped as seen in Figure 3.4. The flexible ring model systems with complex damping were all missing the first mode from the normal flexible ring model with no damping that corresponds to the rigid mode of the tire.

Table 3.2: Flexible Ring Model Results Summary

Type	Amplitude, K	Frequency range solved	Frequency of the 1st mode	Frequency of the 2nd mode	Frequency of the 3rd mode	note
Normal	-	80-150	97.19	120.2	140.8	
Damping	$1.0E+3$ Ns/m	0-250	97.2	120.2	140.8	
Damping	$1.0E+4$ Ns/m	0-250	-	-	-	overdamped
Cubic Stiffness	$1.0E+6$ N/m ³	0-200	100.2	121.6	140.6	No change
Cubic Stiffness	$1.0E+7$ N/m ³	0-200	100.2	121.6	140.6	No change
Cubic Stiffness	$1.0E+8$ N/m ³	0-200	99.8	122.2	145	
Damping	$1.0E+5j$ Ns/m	0-250	-	38.2	47.6	no rigid mode
Damping	$1.0E+6j$ Ns/m	0-10	-	4.26	5.28	no rigid mode
Damping	$5.0E+5j$ Ns/m	0-5	-	8.15	9.8	no rigid mode

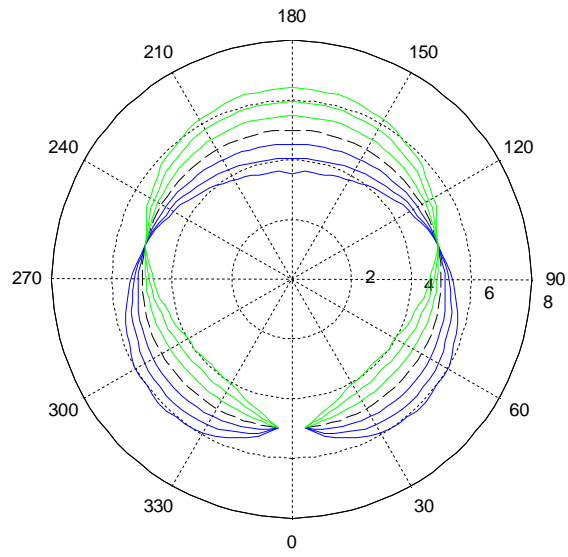


a) FRFs for one hundred and one equally distributed points around the tire.

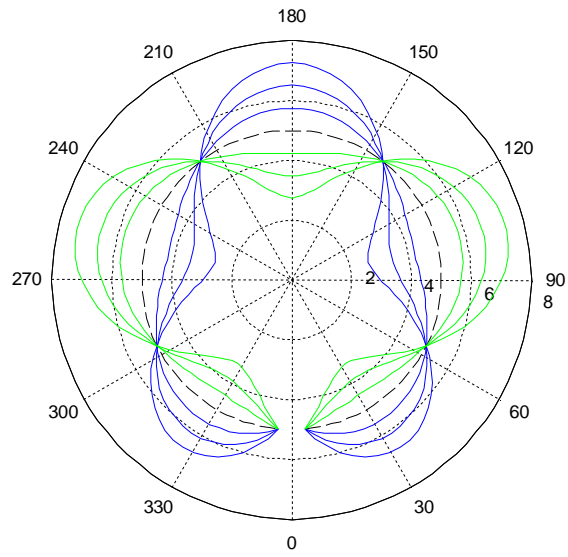


b) Representative plots at 90° and 180° .

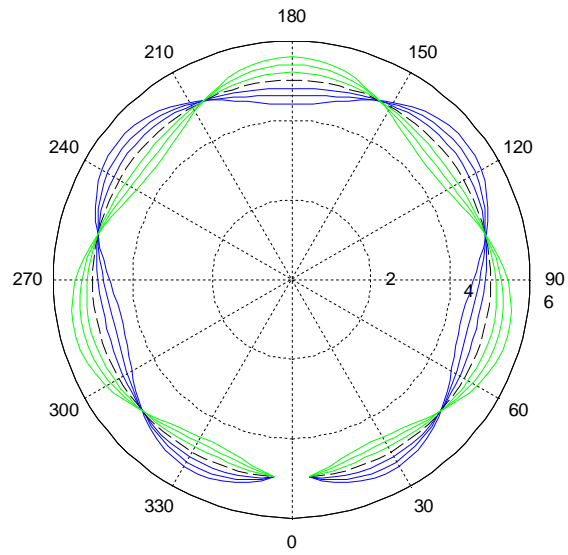
Figure 3.1: FRFs of radial displacement at different locations on the tire to input displacement. Predictions of the flexible ring model are shown. The different locations around the tire where the flexible ring model predictions were made are shown by a different color. The red line with amplitude of one for all frequencies correspond to the points at the base of the tire where the input was applied, hence, the corresponding FRF magnitude is 1.



a) 1st flexible mode, 97.19 Hz, flexible ring model with no damping

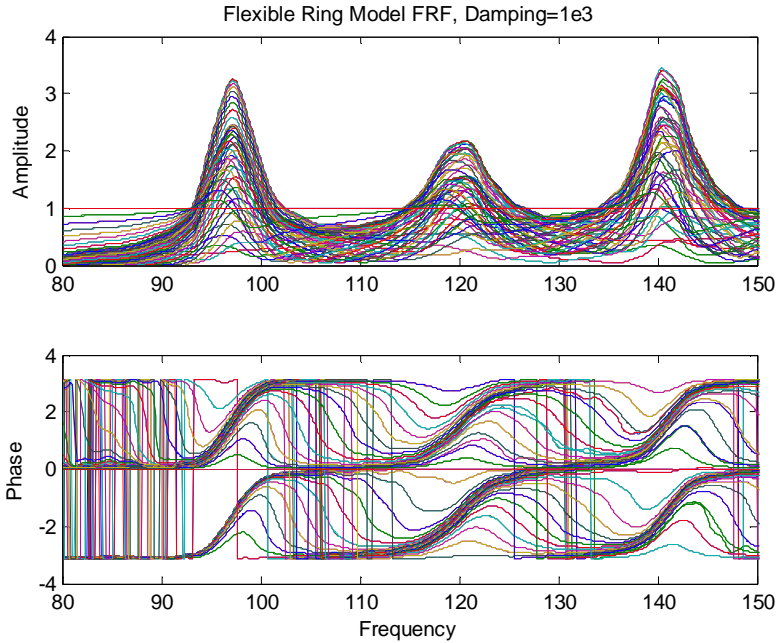


b) 2nd flexible mode, 120.2 Hz, flexible ring model with no damping

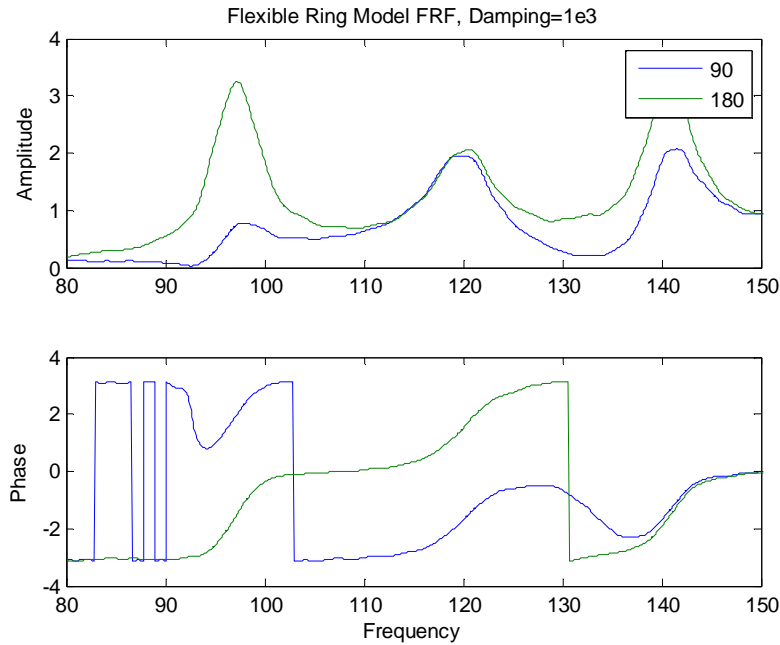


c) 3rd flexible mode, 140.8 Hz, flexible ring model with no damping

Figure 3.2: First three modes predicted by the flexible ring model with no damping. The dashed line in each figure corresponds to the nominal position, and the lines in blue and green correspond to the extremes of the mode shape motions.

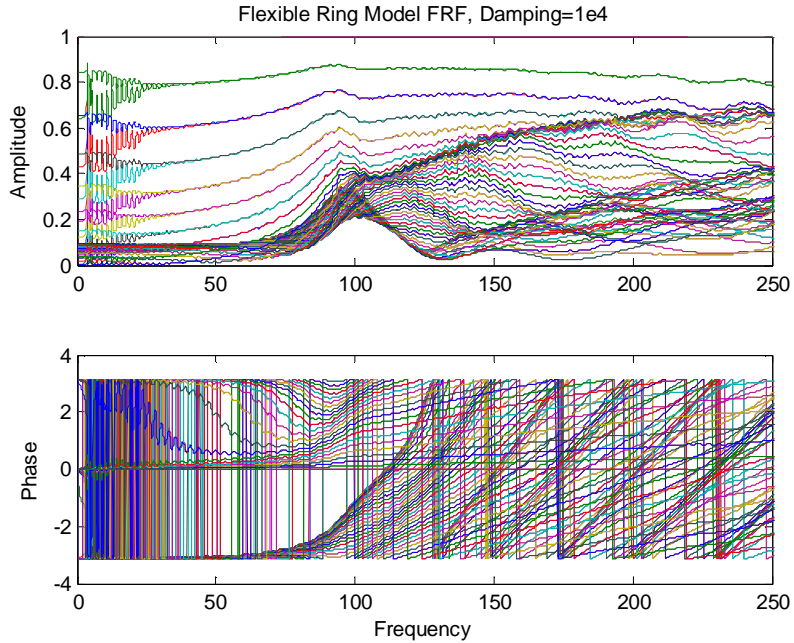


a) FRFs for one hundred and one equally distributed points around the tire.

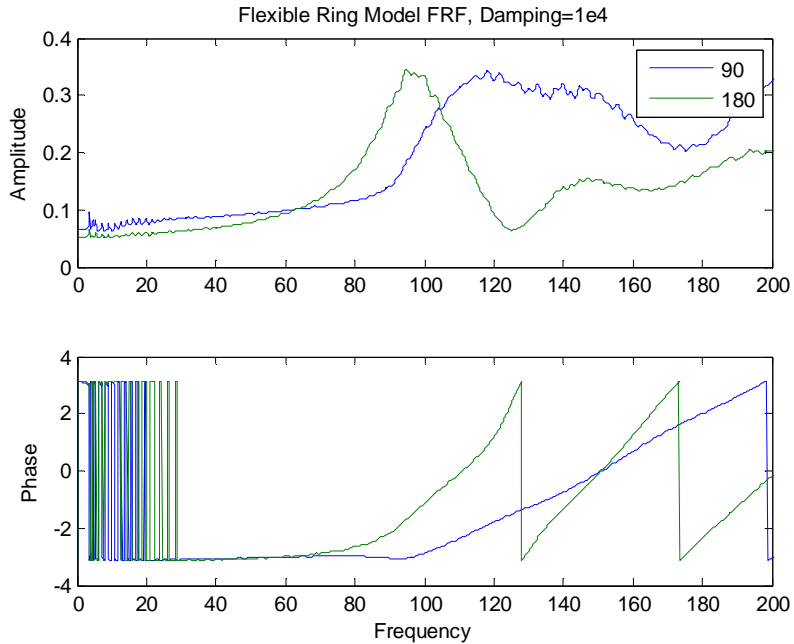


b) Representative plots at 90° and 180°.

Figure 3.3: FRFs of radial displacement at different locations on the tire to input displacement. Predictions of the flexible ring model with regular damping, with magnitude 1e3 Ns/m, are shown. The different locations around the tire where the flexible ring model predictions were made are shown by a different color. The red line with amplitude of one for all frequencies correspond to the points at the base of the tire where the input was applied, hence, the corresponding FRF magnitude is 1.

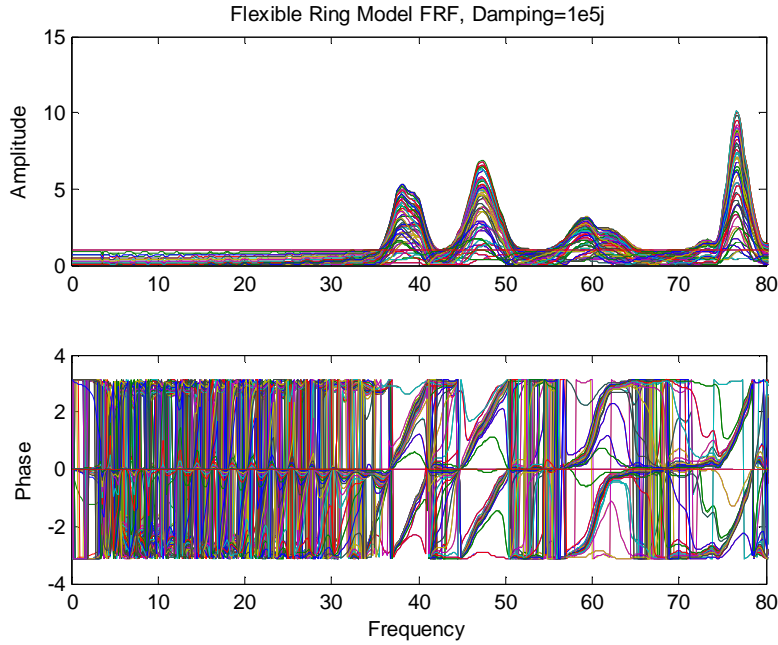


a) FRFs for one hundred and one equally distributed points around the tire.

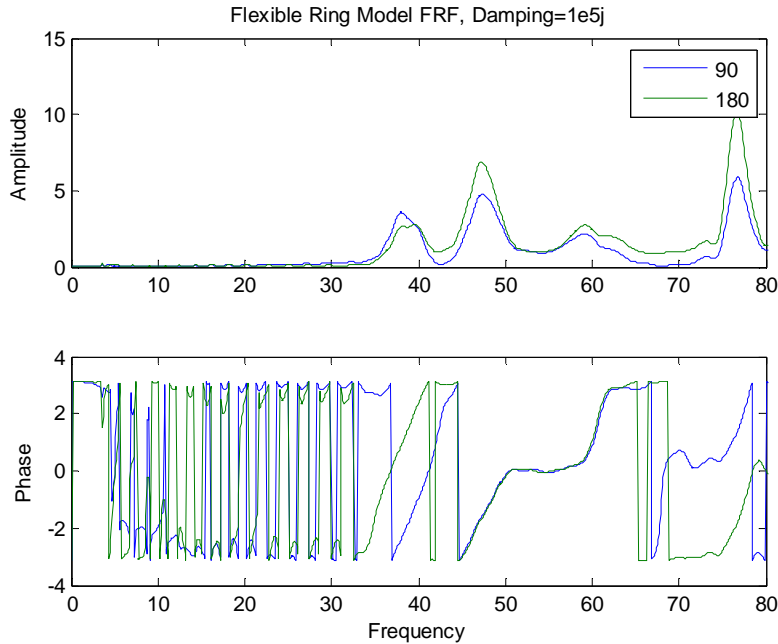


b) Representative plots at 90° and 180° .

Figure 3.4: FRFs of radial displacement at different locations on the tire to input displacement. Predictions of the flexible ring model with regular damping, with magnitude $1e4$ Ns/m, are shown. The different locations around the tire where the flexible ring model predictions were made are shown by a different color. The red line with amplitude of one for all frequencies correspond to the points at the base of the tire where the input was applied, hence, the corresponding FRF magnitude is 1.

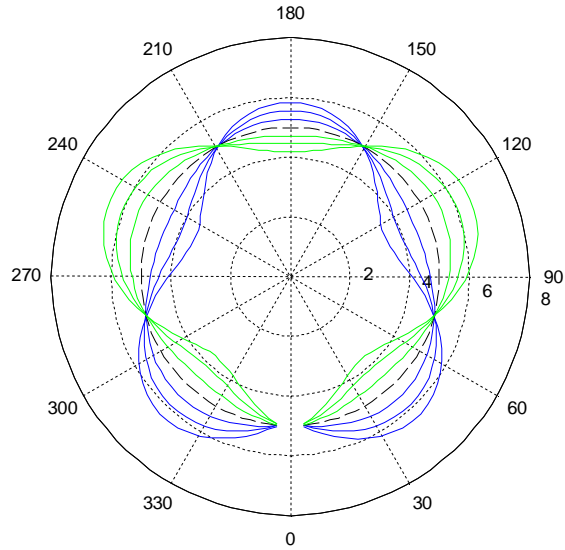


a) FRFs for one hundred and one equally distributed points around the tire.

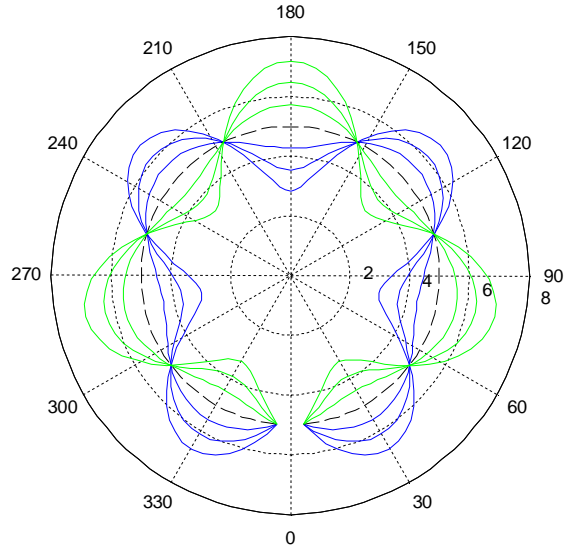


b) Representative plots at 90° and 180° .

Figure 3.5: FRFs of radial displacement at different locations on the tire to input displacement. Predictions of the flexible ring model with complex damping, with magnitude $1e5j$ Ns/m, are shown. The different locations around the tire where the flexible ring model predictions were made are shown by a different color. The red line with amplitude of one for all frequencies correspond to the points at the base of the tire where the input was applied, hence, the corresponding FRF magnitude is 1.

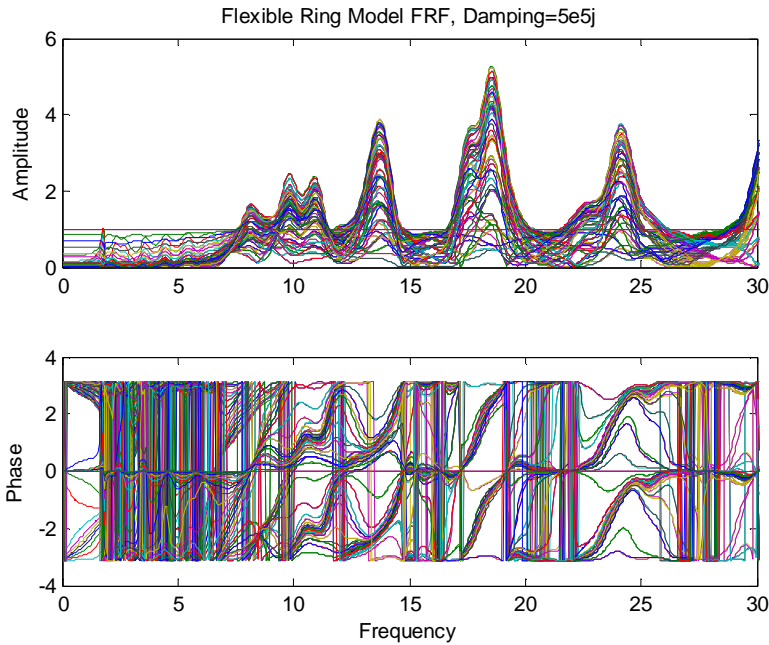


a) 2nd flexible mode, 38.2 Hz, flexible ring model with complex damping $K_d=1e5j$

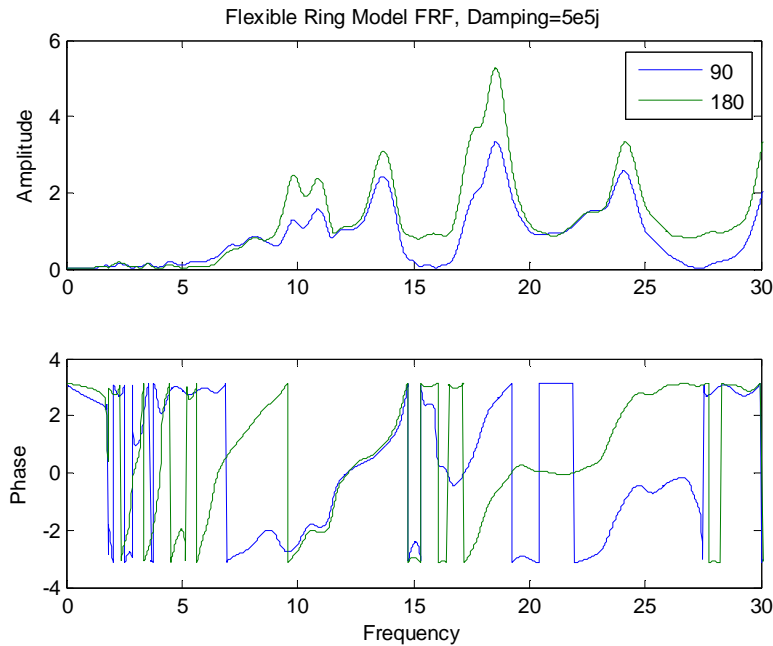


b) 3rd flexible mode, 47.6 Hz, flexible ring model with complex damping $K_d=1e5j$

Figure 3.6: First three modes predicted by the flexible ring model with complex damping of magnitude $K_d=1e5j$. The dashed line in each figure corresponds to the nominal position, and the lines in blue and green correspond to the extremes of the mode shape motions.

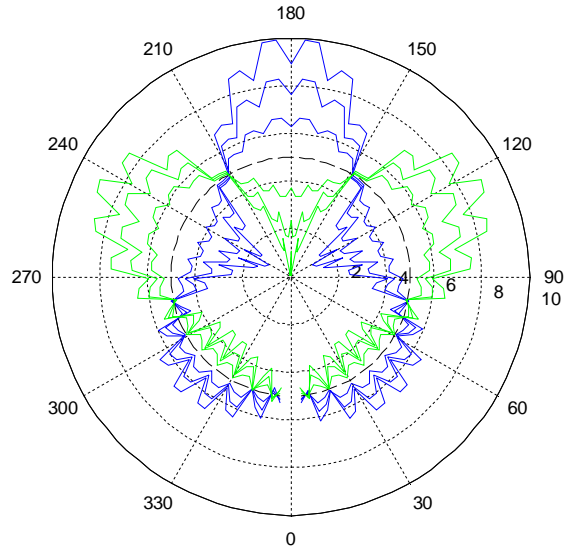


a) FRFs for one hundred and one equally distributed points around the tire.

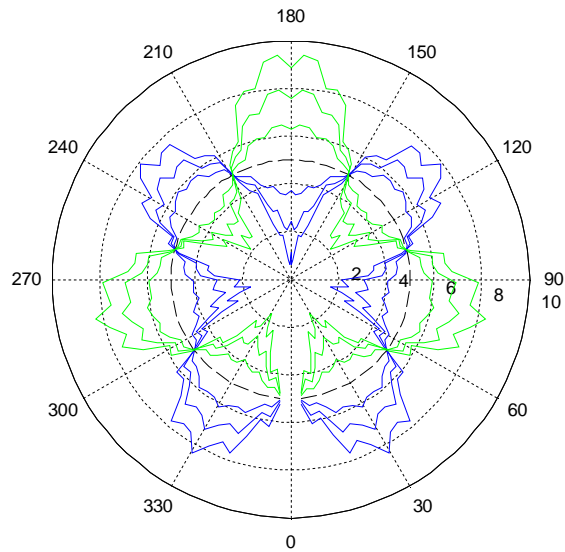


b) Representative plots at 90° and 180° .

Figure 3.7: FRFs of radial displacement at different locations on the tire to input displacement. Predictions of the flexible ring model with complex damping, with magnitude $5e5j$ Ns/m, are shown. The different locations around the tire where the flexible ring model predictions were made are shown by a different color. The red line with amplitude of one for all frequencies correspond to the points at the base of the tire where the input was applied, hence, the corresponding FRF magnitude is 1.

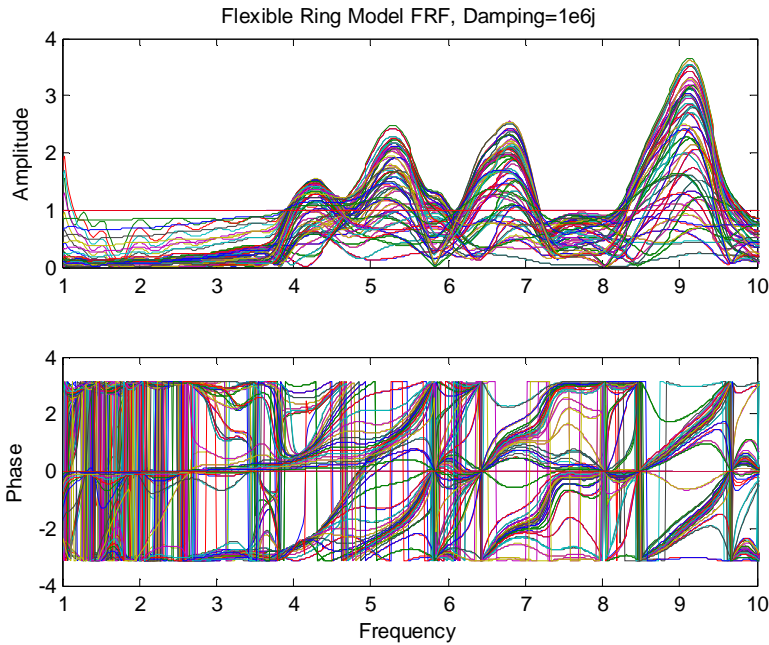


a) 2nd flexible mode, 8.15 Hz, flexible ring model with complex damping $K_d=5e5j$

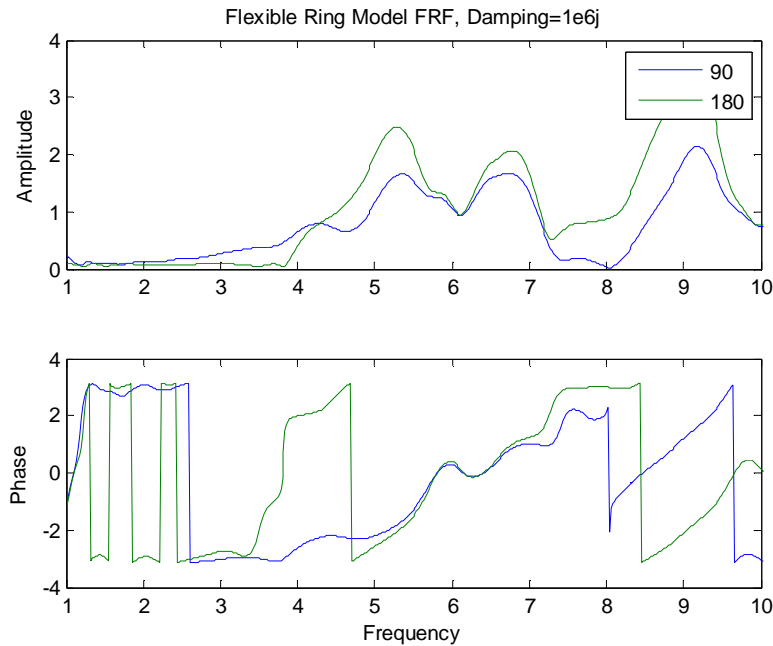


b) 3rd flexible mode, 9.80 Hz, flexible ring model with complex damping $K_d=5e5j$

Figure 3.8: First three modes predicted by the flexible ring model with complex damping of magnitude $K_d=5e5j$. The dashed line in each figure corresponds to the nominal position, and the lines in blue and green correspond to the extremes of the mode shape motions.

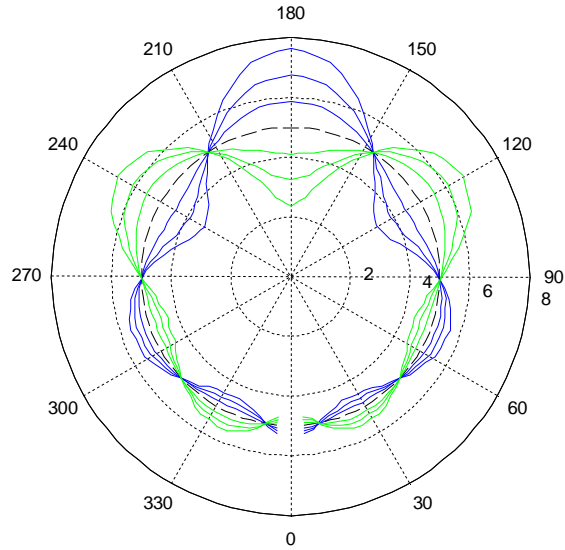


a) FRFs for one hundred and one equally distributed points around the tire.

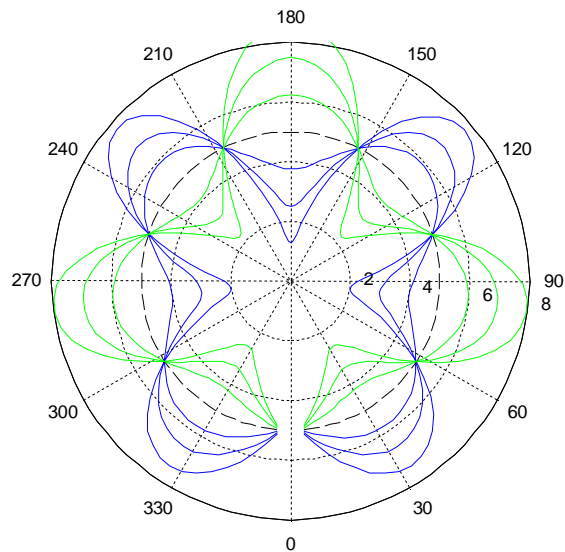


b) Representative plots at 90° and 180° .

Figure 3.9: FRFs of radial displacement at different locations on the tire to input displacement. Predictions of the flexible ring model with complex damping, with magnitude $1e6j$ Ns/m, are shown. The different locations around the tire where the flexible ring model predictions were made are shown by a different color. The red line with amplitude of one for all frequencies correspond to the points at the base of the tire where the input was applied, hence, the corresponding FRF magnitude is 1.

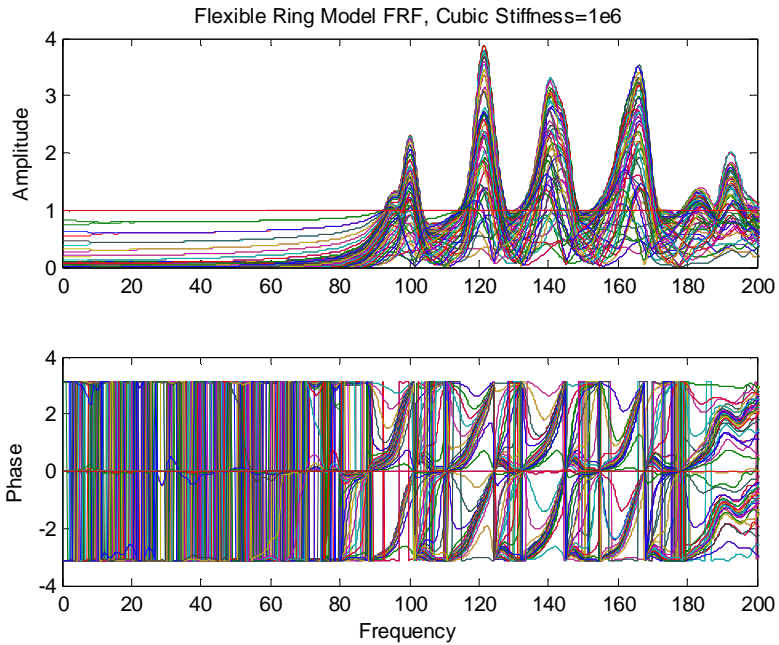


a) 2nd flexible mode, 4.26 Hz, flexible ring model with complex damping $K_d=1e6j$

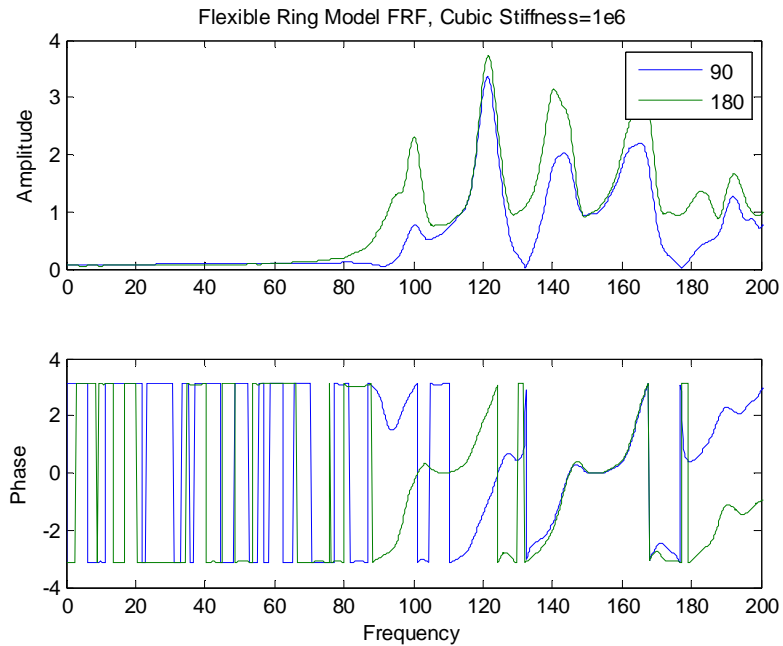


b) 3rd flexible mode, 5.28 Hz, flexible ring model with complex damping $K_d=1e6j$

Figure 3.10: First three modes predicted by the flexible ring model with complex damping of magnitude $K_d=1e6j$. The dashed line in each figure corresponds to the nominal position, and the lines in blue and green correspond to the extremes of the mode shape motions.

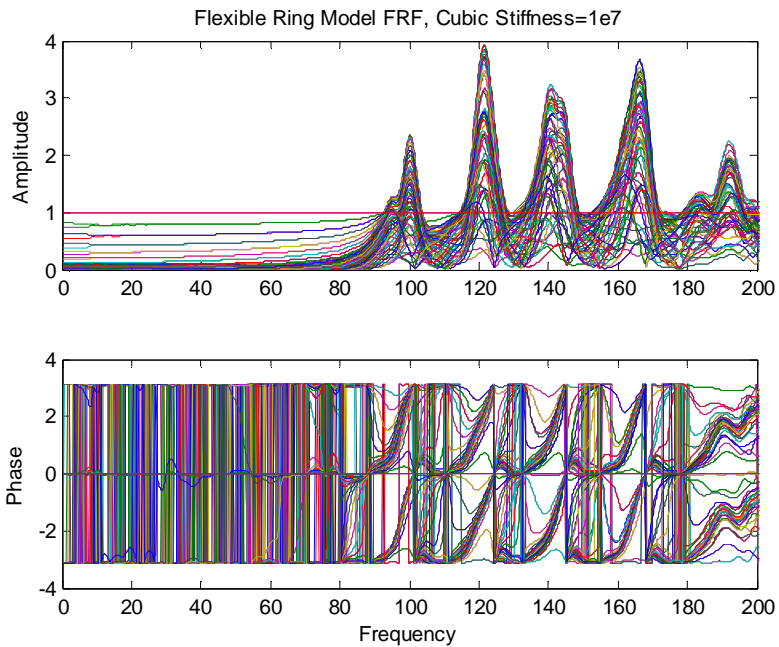


a) FRFs for one hundred and one equally distributed points around the tire.

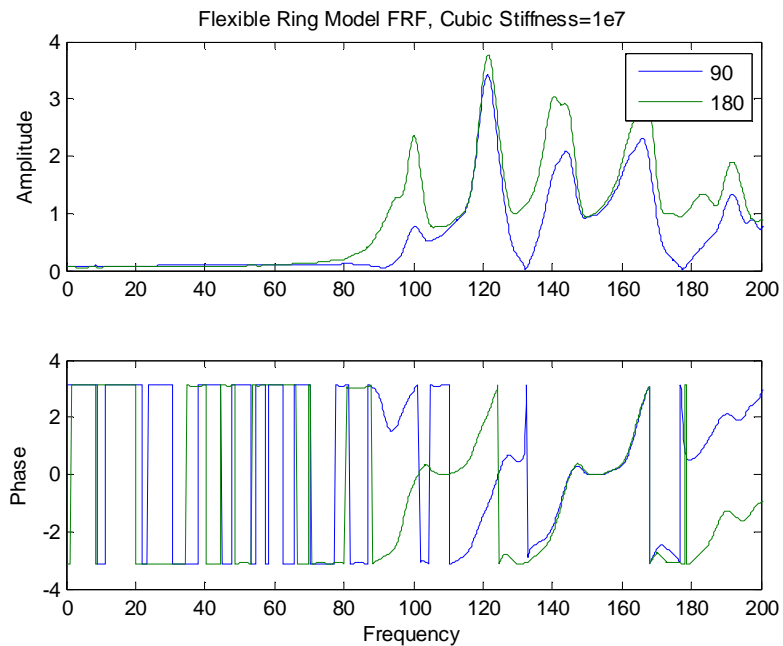


b) Representative plots at 90° and 180° .

Figure 3.11: FRFs of radial displacement at different locations on the tire to input displacement. Predictions of the flexible ring model with cubic stiffness, with magnitude $1e6 \text{ N/m}^3$, are shown. The different locations around the tire where the flexible ring model predictions were made are shown by a different color. The red line with amplitude of one for all frequencies correspond to the points at the base of the tire where the input was applied, hence, the corresponding FRF magnitude is 1.

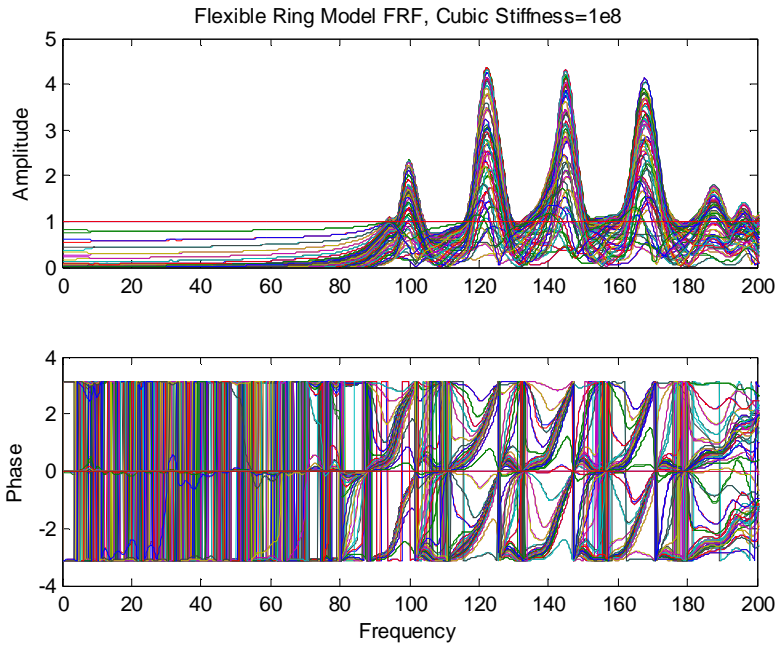


a) FRFs for one hundred and one equally distributed points around the tire.

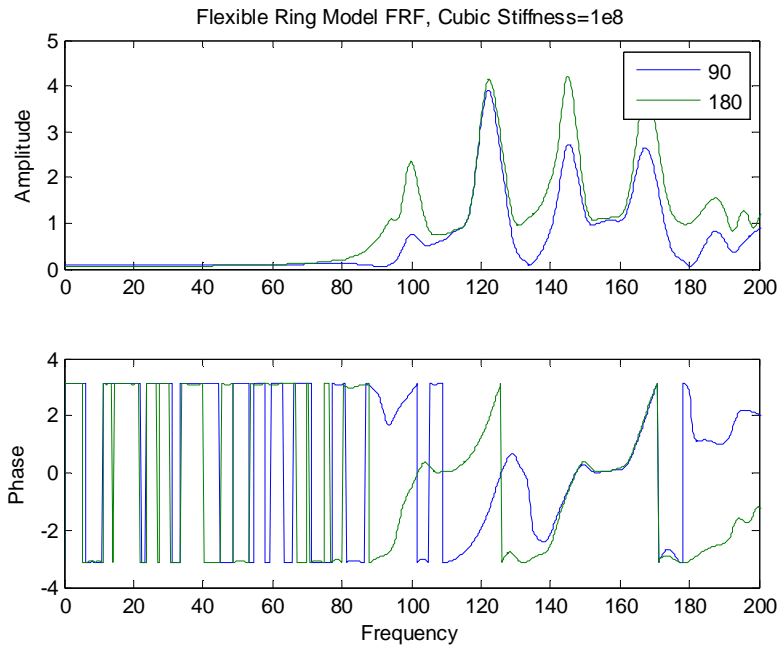


b) Representative plots at 90° and 180°.

Figure 3.12: FRFs of radial displacement at different locations on the tire to input displacement. Predictions of the flexible ring model with cubic stiffness, with magnitude $1e7 \text{ N/m}^3$, are shown. The different locations around the tire where the flexible ring model predictions were made are shown by a different color. The red line with amplitude of one for all frequencies correspond to the points at the base of the tire where the input was applied, hence, the corresponding FRF magnitude is 1.



a) FRFs for one hundred and one equally distributed points around the tire.



b) Representative plots at 90° and 180° .

Figure 3.13: FRFs of radial displacement at different locations on the tire to input displacement. Predictions of the flexible ring model with cubic stiffness, with magnitude $1e8 \text{ N/m}^3$, are shown. The different locations around the tire where the flexible ring model predictions were made are shown by a different color. The red line with amplitude of one for all frequencies correspond to the points at the base of the tire where the input was applied, hence, the corresponding FRF magnitude is 1.

The natural frequencies for the loaded original flexible ring model from this analysis matched the results from Zegelaar's work for the passenger tire, in which natural frequencies of 98.1 Hz, 121.8 Hz, and 143.9 Hz were observed for the first three modes (Zegelaar, 1997). The natural frequencies for the flexible ring model with added nonlinear terms did not change significantly unless there was complex damping present in the system.

The frequency response functions for the flexible ring model with no damping, conventional damping, and nonlinear stiffness terms all have fairly sharp peaks and they do not have the slight peak variations from one point on the tire to the next that the results of the experimental modal analyses for the heavily loaded tire show, see Figures 3.1, 3.3, 3.11, 3.12, and 3.13. The addition of these terms does not affect the overall shapes of the frequency response functions or the mode shapes. The modes appear at consistent frequency intervals from one another. The cubic stiffness terms did not significantly affect the natural frequencies of the modes until the magnitude reached $1e8N/m^3$.

When a larger complex damping term is added to the flexible ring model, a large change in the frequency response function is seen. In Figure 3.8, there is a lot of noise in the response of the system due to the sine sweep input. The mode shapes should be smooth curves and the noise can be attributed to inaccuracies in the numerical solution provided by the 'pdepe' function in MATLAB. In Figure 3.7 and Figure 3.9, the amplitude and the phase of the frequency-response functions are shown for the flexible ring model with a large complex damping term. The modal frequencies are no longer at consistent frequency intervals, and the peaks of the frequency response function for all of the points around the circumference of the tire do not all match up around the natural

frequencies as was seen in the previous cases. This phenomenon is very similar to what was observed in the experimental modal analyses. The variance was attributed to errors accumulated during the experimental setup but it could also be caused by a large complex damping inherent in the system (Ewins, 2000). The present analysis is not conclusive about the influence of nonlinearities. Further studies are needed to understand them.

Chapter 4

Extension of ERPC Framework

4.1 Transfer Function for a Multi-Degree-of-Freedom Tire Model

The current ERPC tire model uses a single degree-of-freedom model to represent the tire system, as shown in Figure 4.1. The different parameters shown in this figure are as follows:

M_1 : mass of the sprung mass, M

M_2 : effective tire mass in the vertical direction, M_{Mtm}

x_{sp} : vertical displacement of the spindle mass

x_0 : vertical displacement of the tire mass

x_R : vertical displacement of the road

The goal of the tire model is to determine x_R in terms of the spindle displacement, x_{sp} , and the spindle force, F_{sp} . The relationships between the road displacement and the spindle displacement and forces are used in the ERPC process to predict the road profile for a measured set of spindle parameters. The equations of motion for the two masses are given by

$$M_1 \ddot{x}_{sp} + K_{xx}(x_{sp} - x_0) + C_{xx}(\dot{x}_{sp} - \dot{x}_0) = F_{sp}(t) \quad (4.1)$$

$$M_2 \ddot{x}_0 + K_{xx}(x_0 - x_R) + C_{xx}(\dot{x}_0 - \dot{x}_R) + K_{xx}(x_0 - x_{sp}) + C_{xx}(\dot{x}_0 - \dot{x}_{sp}) = 0 \quad (4.2)$$

After carrying out Laplace transforms of equations (4.1) and (4.2) and setting the initial conditions to zero, the result is

$$X_{sp}(s^2 M_1 + K_{xx} + sC_{xx}) - F_{sp}(s) = X_0(K_{xx} + sC_{xx}) \quad (4.3)$$

$$(s^2 M_2 + 2K_{xx} + 2sC_{xx})X_0 - X_R(K_{xx} + sC_{xx}) - X_{sp}(K_{xx} + sC_{xx}) = 0 \quad (4.4)$$

Solving for X_0 from (4.3) leads to

$$X_0 = \frac{X_{sp}(s^2 M_1 + K_{xx} + sC_{xx}) - F_{sp}(s)}{(K_{xx} + sC_{xx})} \quad (4.5)$$

On substituting (4.5) into (4.4), the result is

$$X_R = (s^2 M_2 + 2K_{xx} + 2sC_{xx}) \frac{X_{sp}(s^2 M_1 + K_{xx} + sC_{xx}) - F_{sp}(s)}{(K_{xx} + sC_{xx})^2} - X_{sp} \quad (4.6)$$

This is the formula used for prediction of the Effective Road Profile in the ERPC scheme.

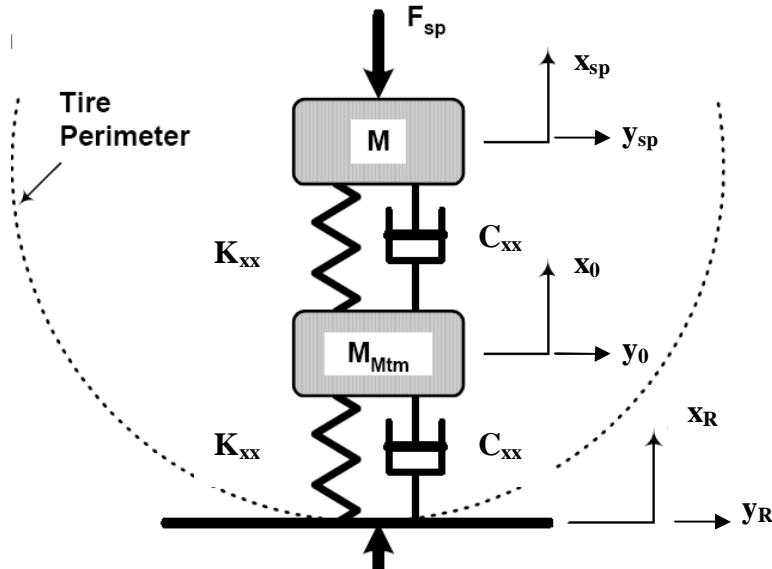


Figure 4.1: Spring and damper tire model used in ERPC.

When an additional degree of freedom is included in the longitudinal directions, the system gets a little more complex. The upper portion of the tire model between the spindle and the tire mass is not directly connected by an axial spring-damper system in the longitudinal direction. It is instead connected by a torsional spring about the mass M , as shown in Figure 4.2. The location of the tire mass stays the same for the vertical and longitudinal directions; it is between the spindle and the road contact point. This makes things a little more complicated since the spring and damper values are not the same between the spindle and the tire mass and the tire mass and road, in the longitudinal direction. The parameters used for the longitudinal direction areas follows:

M_3 : effective tire mass in the longitudinal (y) direction

I_1 : rotational inertia of the sprung mass, M

y_{sp} : longitudinal displacement of the spindle

y_0 : longitudinal displacement of the tire mass

y_R : longitudinal displacement of the road

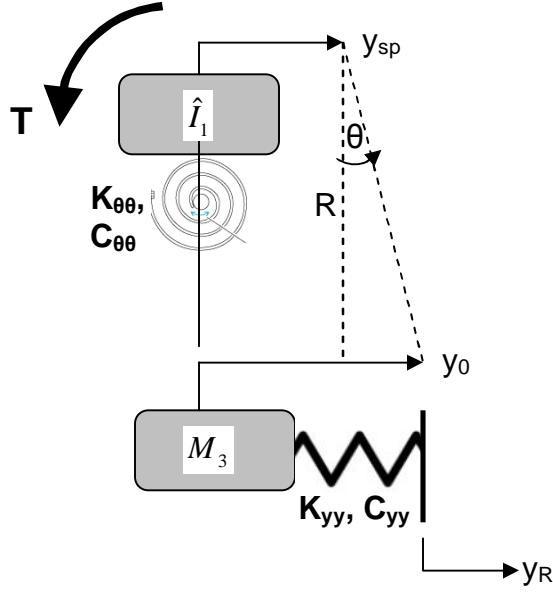


Figure 4.2: Spring and damper tire model for use in ERPC in the longitudinal direction.

The equations of motion for the longitudinal direction are

$$\hat{I}_1(\ddot{\theta}_{sp}) + \hat{K}_{\theta\theta}(\theta_{sp}) + \hat{C}_{\theta\theta}(\dot{\theta}_{sp}) = T(t) \quad (4.7)$$

$$M_3\ddot{y}_0 + K_{yy}(y_0 - y_R) + C_{yy}(\dot{y}_0 - \dot{y}_R) + \hat{K}_{\theta\theta}(\theta_{sp}) + \hat{C}_{\theta\theta}(\dot{\theta}_{sp}) = 0 \quad (4.8)$$

where θ_{sp} can be approximated as

$$\theta_{sp} = \frac{y_0 - y_{sp}}{R} \quad (4.9)$$

and the coefficients $\hat{K}_{\theta\theta}$ and $\hat{C}_{\theta\theta}$ have the appropriate dimensions.

After substituting (4.9) into (4.7) and (4.8) and altering the coefficients to absorb R, the respective equations become

$$I_1(\ddot{y}_0 - \ddot{y}_{sp}) + K_{\theta\theta}(y_0 - y_{sp}) + C_{\theta\theta}(\dot{y}_0 - \dot{y}_{sp}) = T(t) \quad (4.10)$$

$$M_3\ddot{y}_0 + K_{yy}(y_0 - y_R) + C_{yy}(\dot{y}_0 - \dot{y}_R) + K_{\theta\theta}(y_0 - y_{sp}) + C_{\theta\theta}(\dot{y}_0 - \dot{y}_{sp}) = 0 \quad (4.11)$$

After carrying out Laplace transforms of equations (4.10) and (4.11) and setting the initial conditions to zero, the result is

$$T(s) = Y_0(K_{\theta\theta} + sC_{\theta\theta} - s^2I_1) - Y_{sp}(K_{\theta\theta} + sC_{\theta\theta} - s^2I_1) \quad (4.12)$$

$$(s^2M_3 + K_{yy} + sC_{yy} + K_{\theta\theta} + sC_{\theta\theta})Y_0 - Y_R(K_{yy} + sC_{yy}) - Y_{sp}(K_{\theta\theta} + sC_{\theta\theta}) = 0 \quad (4.13)$$

Solving for Y_0 from equation (4.12), the result is

$$Y_0 = \frac{T(s) + Y_{sp}(K_{\theta\theta} + sC_{\theta\theta} - s^2I_1)}{(K_{\theta\theta} + sC_{\theta\theta} - s^2I_1)} \quad (4.14)$$

On substituting (4.14) into (4.13), the result is

$$Y_R = (s^2M_3 + K_{yy} + sC_{yy} + K_{\theta\theta} + sC_{\theta\theta}) \frac{T(s) + Y_{sp}(K_{\theta\theta} + sC_{\theta\theta} - s^2I_1)}{(K_{\theta\theta} + sC_{\theta\theta} - s^2I_1)(K_{yy} + sC_{yy})} - Y_{sp} \frac{(K_{\theta\theta} + sC_{\theta\theta})}{(K_{yy} + sC_{yy})} \quad (4.15)$$

The tire model becomes complex when one starts to include coupling terms involving the vertical and longitudinal motions. If one assumes that there is no coupling between the spindle and the tire mass, but that there is coupling between the tire mass and the road, the equations of motion simplify to

$$M_1\ddot{x}_{sp} + K_{xx}(x_{sp} - x_0) + C_{xx}(\dot{x}_{sp} - \dot{x}_0) = F_{sp}(t) \quad (4.16)$$

$$I_1(\ddot{y}_0 - \ddot{y}_{sp}) + K_{\theta\theta}(y_0 - y_{sp}) + C_{\theta\theta}(\dot{y}_0 - \dot{y}_{sp}) = T(t) \quad (4.17)$$

$$M_2\ddot{x}_0 + K_{xx}(x_0 - x_R) + C_{xx}(\dot{x}_0 - \dot{x}_R) + K_{xx}(x_0 - x_{sp}) + C_{xx}(\dot{x}_0 - \dot{x}_{sp}) + K_{xy}(y_0 - y_R) + C_{xy}(\dot{y}_0 - \dot{y}_R) = 0 \quad (4.18)$$

$$M_3\ddot{y}_0 + K_{yy}(y_0 - y_R) + C_{yy}(\dot{y}_0 - \dot{y}_R) + K_{\theta\theta}(y_0 - y_{sp}) + C_{\theta\theta}(\dot{y}_0 - \dot{y}_{sp}) + K_{yx}(x_0 - x_R) + C_{yx}(\dot{x}_0 - \dot{x}_R) = 0 \quad (4.19)$$

After carrying out Laplace transforms and setting the initial conditions to zero, the result is

$$X_{sp}(s^2 M_1 + K_{xx} + sC_{xx}) - F_{sp}(s) = X_0(K_{xx} + sC_{xx}) \quad (4.20)$$

$$Y_0(K_{\theta\theta} + sC_{\theta\theta} - s^2 I_1) - T_{sp}(K_{\theta\theta} + sC_{\theta\theta} - s^2 I_1) = T(s) \quad (4.21)$$

$$(s^2 M_2 + 2K_{xx} + 2sC_{xx})X_0 - X_R(K_{xx} + sC_{xx}) - X_{sp}(K_{xx} + sC_{xx}) + (Y_0 - Y_R)(K_{xy} + sC_{xy}) = 0 \quad (4.22)$$

$$(s^2 M_3 + K_{yy} + sC_{yy} + K_{\theta\theta} + sC_{\theta\theta})Y_0 - Y_R(K_{yy} + sC_{yy}) - Y_{sp}(K_{\theta\theta} + sC_{\theta\theta}) + (X_0 - X_R)(K_{yx} + sC_{yx}) = 0 \quad (4.23)$$

It is possible to solve these equations for X_R and Y_R , but it is easier to deal with system matrix form; that is,

$$\begin{aligned} \begin{bmatrix} M_1 & 0 \\ 0 & -I_1 \end{bmatrix} \begin{Bmatrix} \ddot{x}_{sp} \\ \ddot{y}_{sp} \end{Bmatrix} + \begin{bmatrix} 0 & 0 \\ 0 & I_1 \end{bmatrix} \begin{Bmatrix} \ddot{x}_0 \\ \ddot{y}_0 \end{Bmatrix} + \begin{bmatrix} K_{xx} & 0 \\ 0 & -K_{\theta\theta} \end{bmatrix} \begin{Bmatrix} x_{sp} \\ y_{sp} \end{Bmatrix} + \begin{bmatrix} -K_{xx} & 0 \\ 0 & K_{\theta\theta} \end{bmatrix} \begin{Bmatrix} x_0 \\ y_0 \end{Bmatrix} \\ + \begin{bmatrix} C_{xx} & 0 \\ 0 & -C_{\theta\theta} \end{bmatrix} \begin{Bmatrix} \dot{x}_{sp} \\ \dot{y}_{sp} \end{Bmatrix} + \begin{bmatrix} -C_{xx} & 0 \\ 0 & C_{\theta\theta} \end{bmatrix} \begin{Bmatrix} \dot{x}_0 \\ \dot{y}_0 \end{Bmatrix} = \begin{Bmatrix} F_{sp}(t) \\ T(t) \end{Bmatrix} \end{aligned} \quad (4.24)$$

$$\begin{aligned} \begin{bmatrix} M_2 & 0 \\ 0 & M_3 \end{bmatrix} \begin{Bmatrix} \ddot{x}_0 \\ \ddot{y}_0 \end{Bmatrix} + \begin{bmatrix} -K_{xx} & K_{x\theta} \\ K_{\theta x} & -K_{\theta\theta} \end{bmatrix} \begin{Bmatrix} x_{sp} \\ y_{sp} \end{Bmatrix} + \begin{bmatrix} 2K_{xx} & K_{xy} \\ K_{yx} & K_{yy} + K_{\theta\theta} \end{bmatrix} \begin{Bmatrix} x_0 \\ y_0 \end{Bmatrix} + \begin{bmatrix} -K_{xx} & -K_{xy} \\ -K_{yx} & -K_{yy} \end{bmatrix} \begin{Bmatrix} x_R \\ y_R \end{Bmatrix} \\ + \begin{bmatrix} -C_{xx} & 0 \\ 0 & -C_{\theta\theta} \end{bmatrix} \begin{Bmatrix} \dot{x}_{sp} \\ \dot{y}_{sp} \end{Bmatrix} + \begin{bmatrix} 2C_{xx} & C_{xy} \\ C_{yx} & C_{yy} + C_{\theta\theta} \end{bmatrix} \begin{Bmatrix} \dot{x}_0 \\ \dot{y}_0 \end{Bmatrix} + \begin{bmatrix} -C_{xx} & -C_{xy} \\ -C_{yx} & -C_{yy} \end{bmatrix} \begin{Bmatrix} \dot{x}_R \\ \dot{y}_R \end{Bmatrix} = \begin{Bmatrix} 0 \\ 0 \end{Bmatrix} \end{aligned}$$

If we assume that there is coupling between the spindle and the tire mass, the equations of motion become

$$\begin{aligned} \begin{bmatrix} M_1 & 0 \\ 0 & -I_1 \end{bmatrix} \begin{Bmatrix} \ddot{x}_{sp} \\ \ddot{y}_{sp} \end{Bmatrix} + \begin{bmatrix} 0 & 0 \\ 0 & I_1 \end{bmatrix} \begin{Bmatrix} \ddot{x}_0 \\ \ddot{y}_0 \end{Bmatrix} + \begin{bmatrix} K_{xx} & -K_{x\theta} \\ K_{\theta x} & -K_{\theta\theta} \end{bmatrix} \begin{Bmatrix} x_{sp} \\ y_{sp} \end{Bmatrix} + \begin{bmatrix} -K_{xx} & K_{x\theta} \\ -K_{\theta x} & K_{\theta\theta} \end{bmatrix} \begin{Bmatrix} x_0 \\ y_0 \end{Bmatrix} \\ + \begin{bmatrix} C_{xx} & -C_{x\theta} \\ C_{\theta x} & -C_{\theta\theta} \end{bmatrix} \begin{Bmatrix} \dot{x}_{sp} \\ \dot{y}_{sp} \end{Bmatrix} + \begin{bmatrix} -C_{xx} & C_{x\theta} \\ -C_{\theta x} & C_{\theta\theta} \end{bmatrix} \begin{Bmatrix} \dot{x}_0 \\ \dot{y}_0 \end{Bmatrix} = \begin{Bmatrix} F_{sp}(t) \\ T(t) \end{Bmatrix} \end{aligned} \quad (4.25)$$

$$\begin{aligned} \begin{bmatrix} M_2 & 0 \\ 0 & M_3 \end{bmatrix} \begin{Bmatrix} \ddot{x}_0 \\ \ddot{y}_0 \end{Bmatrix} + \begin{bmatrix} -K_{xx} & K_{x\theta} \\ K_{\theta x} & -K_{\theta\theta} \end{bmatrix} \begin{Bmatrix} x_{sp} \\ y_{sp} \end{Bmatrix} + \begin{bmatrix} 2K_{xx} & K_{xy} - K_{x\theta} \\ K_{yx} - K_{\theta x} & K_{yy} + K_{\theta\theta} \end{bmatrix} \begin{Bmatrix} x_0 \\ y_0 \end{Bmatrix} + \begin{bmatrix} -K_{xx} & -K_{xy} \\ -K_{yx} & -K_{yy} \end{bmatrix} \begin{Bmatrix} x_R \\ y_R \end{Bmatrix} \\ + \begin{bmatrix} -C_{xx} & +C_{x\theta} \\ C_{\theta x} & -C_{\theta\theta} \end{bmatrix} \begin{Bmatrix} \dot{x}_{sp} \\ \dot{y}_{sp} \end{Bmatrix} + \begin{bmatrix} 2C_{xx} & C_{xy} - C_{x\theta} \\ C_{yx} - C_{\theta x} & C_{yy} + C_{\theta\theta} \end{bmatrix} \begin{Bmatrix} \dot{x}_0 \\ \dot{y}_0 \end{Bmatrix} + \begin{bmatrix} -C_{xx} & -C_{xy} \\ -C_{yx} & -C_{yy} \end{bmatrix} \begin{Bmatrix} \dot{x}_R \\ \dot{y}_R \end{Bmatrix} = \begin{Bmatrix} 0 \\ 0 \end{Bmatrix} \end{aligned} \quad (4.26)$$

After taking Laplace transforms and setting the initial conditions to zero, the result is

$$\begin{bmatrix} s^2 M_1 + K_{xx} + sC_{xx} & -K_{x\theta} - sC_{x\theta} \\ K_{\theta x} + sC_{\theta x} & -s^2 I_1 - K_{\theta\theta} - sC_{\theta\theta} \end{bmatrix} \begin{Bmatrix} X_{sp} \\ Y_{sp} \end{Bmatrix} + \begin{bmatrix} -K_{xx} - sC_{xx} & K_{x\theta} + sC_{x\theta} \\ -K_{\theta x} - sC_{\theta x} & s^2 I_1 + K_{\theta\theta} + sC_{\theta\theta} \end{bmatrix} \begin{Bmatrix} X_0 \\ Y_0 \end{Bmatrix} = \begin{Bmatrix} F_{sp}(s) \\ T(s) \end{Bmatrix} \quad (4.27)$$

$$\begin{bmatrix} s^2 M_2 + 2K_{xx} + 2sC_{xx} & K_{xy} - K_{x\theta} + sC_{xy} - sC_{x\theta} \\ K_{yx} - K_{\theta x} + sC_{yx} - sC_{\theta x} & s^2 M_3 + K_{yy} + K_{\theta\theta} + sC_{yy} + sC_{\theta\theta} \end{bmatrix} \begin{Bmatrix} X_0 \\ Y_0 \end{Bmatrix} + \begin{bmatrix} -K_{xx} - sC_{xx} & +K_{x\theta} + sC_{x\theta} \\ K_{\theta x} + sC_{\theta x} & -K_{\theta\theta} - sC_{\theta\theta} \end{bmatrix} \begin{Bmatrix} X_{sp} \\ Y_{sp} \end{Bmatrix} \\ + \begin{bmatrix} -K_{xx} - sC_{xx} & -K_{xy} - sC_{xy} \\ -K_{yx} - sC_{yx} & -K_{yy} - sC_{yy} \end{bmatrix} \begin{Bmatrix} X_R \\ Y_R \end{Bmatrix} = \begin{Bmatrix} 0 \\ 0 \end{Bmatrix} \quad (4.28)$$

Solving for $\begin{Bmatrix} X_0 \\ Y_0 \end{Bmatrix}$ and letting $A_{ij} = K_{ij} + sC_{ij}$, leads to

$$\begin{Bmatrix} X_0 \\ Y_0 \end{Bmatrix} = \begin{bmatrix} -A_{xx} & A_{x\theta} \\ -A_{\theta x} & s^2 I_1 + A_{\theta\theta} \end{bmatrix}^{-1} \begin{Bmatrix} F_{sp}(s) \\ T(s) \end{Bmatrix} - \begin{bmatrix} -A_{xx} & A_{x\theta} \\ -A_{\theta x} & s^2 I_1 + A_{\theta\theta} \end{bmatrix}^{-1} \begin{bmatrix} s^2 M_1 + A_{xx} & -A_{x\theta} \\ A_{\theta x} & -s^2 I_1 - A_{\theta\theta} \end{bmatrix} \begin{Bmatrix} X_{sp} \\ Y_{sp} \end{Bmatrix} \quad (4.29)$$

$$\begin{Bmatrix} X_0 \\ Y_0 \end{Bmatrix} = - \begin{bmatrix} s^2 M_2 + 2A_{xx} & A_{xy} - A_{x\theta} \\ A_{yx} - A_{\theta x} & s^2 M_3 + A_{yy} + A_{\theta\theta} \end{bmatrix}^{-1} \begin{bmatrix} -A_{xx} & A_{x\theta} \\ A_{\theta x} & A_{\theta\theta} \end{bmatrix} \begin{Bmatrix} X_{sp} \\ Y_{sp} \end{Bmatrix} \\ - \begin{bmatrix} s^2 M_2 + 2A_{xx} & A_{xy} - A_{x\theta} \\ A_{yx} - A_{\theta x} & s^2 M_3 + A_{yy} + A_{\theta\theta} \end{bmatrix}^{-1} \begin{bmatrix} -A_{xx} & -A_{xy} \\ -A_{yx} & -A_{yy} \end{bmatrix} \begin{Bmatrix} X_R \\ Y_R \end{Bmatrix} \quad (4.30)$$

One can then solve for $\begin{Bmatrix} X_R \\ Y_R \end{Bmatrix}$ by using

$$\begin{bmatrix} s^2 M_2 + 2A_{xx} & A_{xy} - A_{x\theta} \\ A_{yx} - A_{\theta x} & s^2 M_3 + A_{yy} + A_{\theta\theta} \end{bmatrix}^{-1} \begin{bmatrix} -A_{xx} & -A_{xy} \\ -A_{yx} & -A_{yy} \end{bmatrix} \begin{Bmatrix} X_R \\ Y_R \end{Bmatrix} \\ = \\ \left(\begin{bmatrix} -A_{xx} & A_{x\theta} \\ -A_{\theta x} & s^2 I_1 + A_{\theta\theta} \end{bmatrix}^{-1} \begin{bmatrix} s^2 M_1 + A_{xx} & -A_{x\theta} \\ A_{\theta x} & -s^2 I_1 - A_{\theta\theta} \end{bmatrix} - \begin{bmatrix} s^2 M_2 + 2A_{xx} & A_{xy} - A_{x\theta} \\ A_{yx} - A_{\theta x} & s^2 M_3 + A_{yy} + A_{\theta\theta} \end{bmatrix}^{-1} \begin{bmatrix} -A_{xx} & A_{x\theta} \\ A_{\theta x} & A_{\theta\theta} \end{bmatrix} \right) \begin{Bmatrix} X_{sp} \\ Y_{sp} \end{Bmatrix} \\ - \begin{bmatrix} -A_{xx} & A_{x\theta} \\ -A_{\theta x} & s^2 I_1 + A_{\theta\theta} \end{bmatrix}^{-1} \begin{Bmatrix} F_{sp}(s) \\ T(s) \end{Bmatrix} \quad (4.31)$$

While solvable this system is much more complicated than the single-degree-of-freedom model with no coupling that is currently being used in ERPC.

4.2 Connections with Earlier Work

Determining the value for the parameters in the tire stiffness model is not very complicated for a single degree-of-freedom system. It is much more complicated to determine the parameters for a multi-degree-of-freedom system. The coupling stiffness and damping terms are especially difficult to determine. The previous work done in the earlier chapters of this thesis can be used to help determine these parameters.

The natural frequencies and mode shapes of the tire obtained in the experimental modal analysis can be used to help determine the stiffness and mass parameters to be used with the tire stiffness model for ERPC. The coupling terms are not be easily extractable but that is a possibility for future work.

The flexible ring model proposed in Chapter 3 with added damping values can also be used to determine the parameters needed for the ERPC tire stiffness model. By performing a parameter study on the flexible ring model, the stiffness terms could be identified for use in the ERPC model. Further investigation into finding an accurate value for the complex damping term used in the flexible ring model may also lead to accurate damping terms for use in the ERPC tire model.

One way to incorporate the modal analysis data into the ERPC process is to use a modal superposition method for the tire model. Once one knows the modes, the response of the system can be defined as some linear combination of its modes. If one knows all of the modes of the tire in all directions, one would just need an accurate way to determine the modal excitations for a given input signal to determine the tire tread

response. The modal excitation for a given mode is the amount that mode is excited by a given input. Since one is interested in only the displacement of the tire contact patch, one can limit the points on the spatial profile to just to those at the contact patch, which would make the computations much easier. The only hard part is to determine the modal excitations for a given input signal.

Chapter 5

Concluding Remarks

5.1 Contributions to the Field

The work in this thesis is one of the first on vibration characteristics of heavily loaded vehicle tires. The experimental modal analysis and the resulting natural frequencies and mode shapes obtained provide some information reported for the first time for this class of vehicle tire. Natural frequencies and mode shapes were obtained in the radial, tangential, and longitudinal directions, and this information can be used in any number of vehicle handling and durability studies. The mode shapes are similar to those found in passenger vehicles but located at much lower frequencies, and the modes could be easier to excite during normal operations. The spacing of the natural frequencies for the heavily loaded vehicle tire differs from the spacing of the corresponding modes for a passenger vehicle tire. The profile of the FRFs used to determine the natural frequencies and mode shapes also differ significantly from a heavily loaded vehicle tire to a passenger vehicle tire. Also, in the experiments, some coupling between modes in different spatial directions was observed. This has not been reported before for passenger vehicle tires.

The flexible ring model has been studied along with the addition of complex damping terms and nonlinear terms in the form of cubic stiffness terms. The addition of

these nonlinear terms may explain some of the differences between the response of passenger car tires and heavily loaded vehicle tires seen in the experimental modal analysis. However, further work is needed before any conclusive statements can be made. The flexible ring model with a large amount of complex damping has response FRFs that look qualitatively similar to those found in the experimental modal analysis for a heavily loaded vehicle tire.

The study into expanding the single degree-of-freedom tire model used in ERPC into one with multiple degrees of freedom and inclusion of coupling between the degrees of freedom could enhance the accuracy of the model if coupling is found to be significant in heavily loaded vehicle tires. This tire model could also be used in various dynamics modeling packages where any increase in the accuracy of tire models greatly increases the accuracy of the predicted response of the vehicle. The Army Materiel Systems Analysis Activity at the Aberdeen Proving Grounds, MD uses many such dynamics modeling packages, such as DADS, VirtualLab, and ADAMS, where accurate tire models are necessary for performing physics of failure analyses on military vehicles.

5.2 Suggestions for Future Work

There is a lot of work that remains to be done for the characterization of heavily loaded vehicle tires. The experimental modal analysis performed in this thesis helps understand the modes and mode shapes for the heavily loaded tire in all three dimensions. However, one of the main assumptions used in the analysis is that there is no coupling between the modes of the tire. The coupling between motion along different directions is

an area where more analysis is needed. Determining a method to perform experimental modal analysis on the data gathered for this thesis while taking into account possible coupling effects between the modes along different directions in the system would be a large endeavor and a definite possible area for future work.

The analytical model presented in this paper is the flexible ring model proposed by Gong (1993). The parameters used in the analysis are not quantitatively relevant to the heavily loaded tire analyzed. The refining of these parameters for the heavily loaded tire is needed, if the model is to be used effectively to determine the response of the heavily loaded tire. The effect of the complex damping term needs to be studied. In this thesis, it was shown that by adding a complex damping term to the flexible ring model, a large difference is made in the response of the tire and it could be indicative of the irregular tire response in the experimental modal analysis. Determining an accurate value for the complex damping term could be very useful for the eventual incorporation of the multi-degree-of-freedom tire model in the ERPC process.

In this thesis, the author has looked at a very simple form of coupling in the tire stiffness model that could be used in the ERPC process. Further investigations into possible coupling terms and multi-degree-of-freedom tire models would be of great benefit to the ERPC efforts at the Roadway Simulator in Aberdeen Proving Ground, Maryland. The refinement of the multi-degree-of-freedom model and the parameters used within is also an area that could use more work in the future.

Appendix and Programs

loadRPCdata_generic_all_Accel

This program loads the data obtained from testing and then performs the experimental modal analysis by creating FRF's, fitting single-degree-of-freedom systems to each point around the tire and approximating the modal amplitudes by minimizing the resulting error. The modal analysis is repeated for a large frequency range and the natural frequencies are picked up as the minimum of the errors.

```
clear

%*****
% YOU MUST ADD THE atcplotter FOLDER TO YOU MATLAB PATH BEFORE YOU RUN THIS
% M-FILE
%*****

load 50psi_sweep.mat %Insert file name and directory here
% [userData.timeHistory, full_scales, units, desc, samplePeriod] =
RPCread3([filename]);
% % generate time vector and channel list
% numSamples = size(userData.timeHistory, 1);
% userData.time = (0:(numSamples-1)) * samplePeriod;
% chan_list = chanlist(desc);

num1=size(sweep_50psi_1_somat.data);
time1 = (0:(num1(1)-1))/1000 ;
num1a=size(sweep_50psi_1_adocs.data);
time1a = (0:(num1a(1)-1))/1000 ;
num2=size(sweep_50psi_2_somat.data);
time2 = (0:(num2(1)-1))/1000 ;
num2a=size(sweep_50psi_2_adocs.data);
time2a = (0:(num2a(1)-1))/1000 ;
num3=size(sweep_50psi_3_somat.data);
time3 = (0:(num3(1)-1))/1000 ;
num3a=size(sweep_50psi_3_adocs.data);
time3a = (0:(num3a(1)-1))/1000 ;

% [B,A]=butter(2,5*2*pi,'high','s')
% [B,A]=butter(2,[5 150]/500)
[B,A]=butter(2,5/500,'high');

%somat

A1x1 = filtfilt(B,A,sweep_50psi_1_somat.data(:,1));
A1y1 = filtfilt(B,A,sweep_50psi_1_somat.data(:,2));
A1z1 = filtfilt(B,A,sweep_50psi_1_somat.data(:,3));
A2x1 = filtfilt(B,A,sweep_50psi_1_somat.data(:,5));
A2y1 = filtfilt(B,A,sweep_50psi_1_somat.data(:,6));
A2z1 = filtfilt(B,A,sweep_50psi_1_somat.data(:,7));
A3x1 = filtfilt(B,A,sweep_50psi_1_somat.data(:,8));
```

```

A3y1 = filtfilt(B,A,sweep_50psi_1_somat.data(:,9));
A3z1 = filtfilt(B,A,sweep_50psi_1_somat.data(:,10));
A4x1 = filtfilt(B,A,sweep_50psi_1_somat.data(:,11));
A4y1 = filtfilt(B,A,sweep_50psi_1_somat.data(:,12));
A4z1 = filtfilt(B,A,sweep_50psi_1_somat.data(:,13));
F1=filtfilt(B,A,sweep_50psi_1_somat.data(:,4));

```

```

A1x2 = filtfilt(B,A,sweep_50psi_2_somat.data(:,1));
A1y2 = filtfilt(B,A,sweep_50psi_2_somat.data(:,2));
A1z2 = filtfilt(B,A,sweep_50psi_2_somat.data(:,3));
A2x2 = filtfilt(B,A,sweep_50psi_2_somat.data(:,5));
A2y2 = filtfilt(B,A,sweep_50psi_2_somat.data(:,6));
A2z2 = filtfilt(B,A,sweep_50psi_2_somat.data(:,7));
A3x2 = filtfilt(B,A,sweep_50psi_2_somat.data(:,8));
A3y2 = filtfilt(B,A,sweep_50psi_2_somat.data(:,9));
A3z2 = filtfilt(B,A,sweep_50psi_2_somat.data(:,10));
A4x2 = filtfilt(B,A,sweep_50psi_2_somat.data(:,11));
A4y2 = filtfilt(B,A,sweep_50psi_2_somat.data(:,12));
A4z2 = filtfilt(B,A,sweep_50psi_2_somat.data(:,13));
F2=filtfilt(B,A,sweep_50psi_2_somat.data(:,4));

```

```

A1x3 = filtfilt(B,A,sweep_50psi_3_somat.data(:,1));
A1y3 = filtfilt(B,A,sweep_50psi_3_somat.data(:,2));
A1z3 = filtfilt(B,A,sweep_50psi_3_somat.data(:,3));
A2x3 = filtfilt(B,A,sweep_50psi_3_somat.data(:,5));
A2y3 = filtfilt(B,A,sweep_50psi_3_somat.data(:,6));
A2z3 = filtfilt(B,A,sweep_50psi_3_somat.data(:,7));
A3x3 = filtfilt(B,A,sweep_50psi_3_somat.data(:,8));
A3y3 = filtfilt(B,A,sweep_50psi_3_somat.data(:,9));
A3z3 = filtfilt(B,A,sweep_50psi_3_somat.data(:,10));
A4x3 = filtfilt(B,A,sweep_50psi_3_somat.data(:,11));
A4y3 = filtfilt(B,A,sweep_50psi_3_somat.data(:,12));
A4z3 = filtfilt(B,A,sweep_50psi_3_somat.data(:,13));
F3=filtfilt(B,A,sweep_50psi_3_somat.data(:,4));

```

```

%adocs

```

```

Fvert1=filtfilt(B,A,sweep_50psi_1_adocs.data(:,1));
Flat1=filtfilt(B,A,sweep_50psi_1_adocs.data(:,2));
Flong1=filtfilt(B,A,sweep_50psi_1_adocs.data(:,3));
ATlat1=filtfilt(B,A,sweep_50psi_1_adocs.data(:,4));
ATlong1=filtfilt(B,A,sweep_50psi_1_adocs.data(:,5));

```

```

Fvert2=filtfilt(B,A,sweep_50psi_2_adocs.data(:,1));
Flat2=filtfilt(B,A,sweep_50psi_2_adocs.data(:,2));
Flong2=filtfilt(B,A,sweep_50psi_2_adocs.data(:,3));
ATlat2=filtfilt(B,A,sweep_50psi_2_adocs.data(:,4));
ATlong2=filtfilt(B,A,sweep_50psi_2_adocs.data(:,5));

```

```

Fvert3=filtfilt(B,A,sweep_50psi_3_adocs.data(:,1));
Flat3=filtfilt(B,A,sweep_50psi_3_adocs.data(:,2));
Flong3=filtfilt(B,A,sweep_50psi_3_adocs.data(:,3));
ATlat3=filtfilt(B,A,sweep_50psi_3_adocs.data(:,4));
ATlong3=filtfilt(B,A,sweep_50psi_3_adocs.data(:,5));

```

```

% fits

```

```

%%1
% tli=24;
% pli=tli*1000+1;
% tlf=600;

```



```

% p1f=t1f*1000+1;
% dt1=9.347+.062-.0420;
% dp1=dt1*1000;
%
% F1f=F1(p1i:p1f);
% time1f=time1(p1i:p1f);
% Flong1f=Flong1(p1i+dp1:p1f+dp1);
%
% ATlong1f=ATlong1(p1i+dp1:p1f+dp1);
% Aly1f=Aly1(p1i:p1f);
% A2y1f=A2y1(p1i:p1f);
% A3y1f=A3y1(p1i:p1f);
% A4y1f=A4y1(p1i:p1f);

% [T1y1f,w1y]=tfestimate(ATlong1f,Aly1f,[],[],[],1000);
% [T2y1f,w2y]=tfestimate(ATlong1f,A2y1f,[],[],[],1000);
% [T3y1f,w3y]=tfestimate(ATlong1f,A3y1f,[],[],[],1000);
% [T4y1f,w4y]=tfestimate(ATlong1f,A4y1f,[],[],[],1000);
[T1y1,w1y]=tfestimate(F1,Aly1,[],[],[],1000);
[T2y1,w2y]=tfestimate(F1,A2y1,[],[],[],1000);
[T3y1,w3y]=tfestimate(F1,A3y1,[],[],[],1000);
[T4y1,w4y]=tfestimate(F1,A4y1,[],[],[],1000);
%2
% t2i=15;
% p2i=t2i*1000+1;
% t2f=600;
% p2f=t2f*1000+1;
% dt2=.4750+.012-.023+.006+.056;
% dp2=dt2*1000;
%
% F2f=F2(p2i:p2f);
% time2f=time2(p2i:p2f);
% Flong2f=Flong2(p2i+dp2:p2f+dp2);
%
% ATlong2f=ATlong2(p2i+dp2:p2f+dp2);
% Aly2f=Aly2(p2i:p2f);
% A2y2f=A2y2(p2i:p2f);
% A3y2f=A3y2(p2i:p2f);
% A4y2f=A4y2(p2i:p2f);

% [T1y2f,w1y]=tfestimate(ATlong2f,Aly2f,[],[],[],1000);
% [T2y2f,w2y]=tfestimate(ATlong2f,A2y2f,[],[],[],1000);
% [T3y2f,w3y]=tfestimate(ATlong2f,A3y2f,[],[],[],1000);
% [T4y2f,w4y]=tfestimate(ATlong2f,A4y2f,[],[],[],1000);
[T1y2,w1y]=tfestimate(F2,Aly2,[],[],[],1000);
[T2y2,w2y]=tfestimate(F2,A2y2,[],[],[],1000);
[T3y2,w3y]=tfestimate(F2,A3y2,[],[],[],1000);
[T4y2,w4y]=tfestimate(F2,A4y2,[],[],[],1000);
%3
% t3i=15;
% p3i=t3i*1000+1;
% t3f=600;
% p3f=t3f*1000+1;
% dt3=0-1.345+.028;
% dp3=dt3*1000;
%
% F3f=F3(p3i:p3f);
% time3f=time3(p3i:p3f);
% Flong3f=Flong3(p3i+dp3:p3f+dp3);
%
% ATlong3f=ATlong3(p3i+dp3:p3f+dp3);
% Aly3f=Aly3(p3i:p3f);
% A2y3f=A2y3(p3i:p3f);

```

```

% A3y3f=A3y3(p3i:p3f);
% A4y3f=A4y3(p3i:p3f);

% [T1y3f,w1y]=tfestimate(ATlong3f,A1y3f,[],[],[],1000);
% [T2y3f,w2y]=tfestimate(ATlong3f,A2y3f,[],[],[],1000);
% [T3y3f,w3y]=tfestimate(ATlong3f,A3y3f,[],[],[],1000);
% [T4y3f,w4y]=tfestimate(ATlong3f,A4y3f,[],[],[],1000);
[T1y3,w1y]=tfestimate(F3,A1y3,[],[],[],1000);
[T2y3,w2y]=tfestimate(F3,A2y3,[],[],[],1000);
[T3y3,w3y]=tfestimate(F3,A3y3,[],[],[],1000);
[T4y3,w4y]=tfestimate(F3,A4y3,[],[],[],1000);

[T1,W1y]=tfestimate(ATlong1,Flong1,[],[],[],1000);
[T2,W2y]=tfestimate(ATlong2,Flong2,[],[],[],1000);
[T3,W3y]=tfestimate(ATlong3,Flong3,[],[],[],1000);

T1y1f=T1y1.*T1;
T2y1f=T2y1.*T1;
T3y1f=T3y1.*T1;
T4y1f=T4y1.*T1;
T1y2f=T1y2.*T2;
T2y2f=T2y2.*T2;
T3y2f=T3y2.*T2;
T4y2f=T4y2.*T2;
T1y3f=T1y3.*T3;
T2y3f=T2y3.*T3;
T3y3f=T3y3.*T3;
T4y3f=T4y3.*T3;

[C,D]=butter(2,5/500,'low')
HH(5,:)=filtfilt(C,D,T1y1f);
HH(7,:)=filtfilt(C,D,T2y1f);
HH(2,:)=filtfilt(C,D,T3y1f);
HH(10,:)=filtfilt(C,D,T4y1f);
HH(4,:)=filtfilt(C,D,T1y2f);
HH(8,:)=filtfilt(C,D,T2y2f);
HH(1,:)=filtfilt(C,D,T3y2f);
HH(11,:)=filtfilt(C,D,T4y2f);
HH(6,:)=filtfilt(C,D,T1y3f);
HH(9,:)=filtfilt(C,D,T2y3f);
HH(3,:)=filtfilt(C,D,T3y3f);
HH(12,:)=filtfilt(C,D,T4y3f);

% H11=HH(5,1:2.5e5);
% H21=HH(7,1:2.5e5);
% H31=HH(2,1:2.5e5);
% H41=HH(10,1:2.5e5);
% H12=HH(4,1:2.5e5);
% H22=HH(8,1:2.5e5);
% H32=HH(1,1:2.5e5);
% H42=HH(11,1:2.5e5);
% H13=HH(6,1:2.5e5);
% H23=HH(9,1:2.5e5);
% H33=HH(3,1:2.5e5);
% H43=HH(12,1:2.5e5);
% w01=linspace(w0(1)*.95,w0(1)*1.05,100);
% w02=linspace(w0(2)*.95,w0(2)*1.05,100);
% w03=linspace(w0(3)*.95,w0(3)*1.05,100);
% w04=linspace(w0(4)*.95,w0(4)*1.05,100);
% w05=linspace(w0(5)*.95,w0(5)*1.05,100);
W11=w1y;

```

```

ii11=0;
ii12=0;
ii21=0;
ii22=0;
ii31=0;
ii32=0;
ii41=0;
ii42=0;
ii51=0;
ii52=0;

mm=1;
Wcount1=resample(W11,1,1);
Wcount=Wcount1(1:25000);

w=[Wcount1';Wcount1';Wcount1';Wcount1';Wcount1';Wcount1';Wcount1';Wcount1';Wcount1';Wcount1';Wcount1';Wcount1'];
Jj=0;
% w1=58.6
w01=linspace(80,140,101)
w02=linspace(43,68.4+2,7)
w03=linspace(75,82+2,7)
w04=linspace(84,101+2,7)
w05=linspace(90,55,11)

for j1=1:101
for j2=1:1
for j3=1:1
for j4=1:1
for j5=1:1

nn11=1;
nn12=4;
nn21=1;
nn22=4;
nn31=1;
nn32=4;
nn41=1;
nn42=4;
nn51=1;
nn52=4;
% w0=[w01(j1),w02(j2),w03(j3),w04(j4),w05(j5)]
% w0=[52.1470,69.6147,81.4533,90.9244,101.3838]
w0=[w01(j1),100,100,100,100]
% w0=[44,53.28,63.31,79,93.88]
Jj=Jj+1

for i=1:5
W0(i,:)=linspace(w0(i)*.95,w0(i)*1.05,100);
end

for j=1:5
for i=1:100
count(i,j)=find(min(abs(Wcount-W0(j,i)))==abs(Wcount-W0(j,i)));
end
end
% k=1

```

```

kk1=linspace(0,10,4);
kk2=linspace(0,10,4);
kk3=linspace(0,10,4);
kk4=linspace(0,10,4);
kk5=linspace(0,10,4);
% if Jj==1
%     mm=1
% else
%     mm=20
% end

for ii=mm:20
if ii==1
kk1=linspace(0,10,4);
kk2=linspace(0,10,4);
kk3=linspace(0,10,4);
kk4=linspace(0,10,4);
kk5=linspace(0,10,4);
else
    kk1=linspace(kkk1(ii11),kkk1(ii12),4);
kk2=linspace(kkk2(ii21),kkk2(ii22),4);
kk3=linspace(kkk3(ii31),kkk3(ii32),4);
kk4=linspace(kkk4(ii41),kkk4(ii42),4);
kk5=linspace(kkk5(ii51),kkk5(ii52),4);
end

kkk1=kk1;
kkk2=kk2;
kkk3=kk3;
kkk4=kk4;
kkk5=kk5;

% k=linspace(0,.2,6);

% k=linspace(0,.2,6);
% kk1=linspace(.2532,.2573,6);
% kk2=linspace(.1158,.1199,6);
% kk3=linspace(.0379,.0420,6);
% kk4=linspace(.0474,.0515,6);
% kk5=linspace(.0648,.0689,6);

% 1:4,3,4,4,3
% 2:2,5,3,4,3

kk=0;
for i1=nn11:nn12
% for i2=nn21:nn22
%     for i3=nn31:nn32
%         for i4=nn41:nn42
%             for i5=nn51:nn52
for i2=1:1
for i3=1:1
for i4=1:1
for i5=1:1
kk=kk+1;
kkk(kk,1)=i1;
kkk(kk,2)=i2;
kkk(kk,3)=i3;
kkk(kk,4)=i4;
kkk(kk,5)=i5;

```

```

k1(1)=kk1(i1);
k1(2)=kk2(i2);
k1(3)=kk3(i3);
k1(4)=kk4(i4);
k1(5)=kk5(i5);

% 32,31,33,12,11,13,21,22,23,41,42,43

% for r=1:10000
%     k=linspace(-5,5,10000);

for l=1:5
    for o=1:100
        G(l,o)=1./(w0(l)^2+2*sqrt(-1)*k1(l)*w0(l).*W0(l,o)-W0(l,o).^2);
%     G(l,o)=1./(w0(l)^2+2*k(m)*w0(l).*W0(l,o)+W0(l,o).^2);
%     GP(m,l)=mean(angle(G(l,:)));
    end
end
% end

for p=1:5
    for n=1:12
        for j=1:100
            Wplot(n,j)=Wcount(count(j,p));
            H(n,j)=HH(n,(count(j,p)));
%            HP(m,n)=mean(angle(H(n,:)));
%            G(i,:)=1./(w1^2+2*i*k(1)*w01*w1-w01.^2);
%            G(n,j)=1./
        end
    end

    for q=1:12

        a(q,p)=(conj(G(p,:))*H(q,:).')/(conj(G(p,:))*G(p,:).');
        E(q,p)=norm(real((H(q,:)-a(q,p)*G(p,:))));
        Ei(q,p)=norm(imag((H(q,:)-a(q,p)*G(p,:))));
        En(q,p)=norm((H(q,:)-a(q,p)*G(p,:)));
        EE(kk,p)=sum(E(:,p));
        EEE(kk,q)=sum(E(q,:));
        EEEE(kk)=sum(sum(E));
        EEi(kk,p)=sum(Ei(:,p));
        EEEi(kk,q)=sum(Ei(q,:));
        EEEEi(kk)=sum(sum(Ei));
        EEn(kk,p)=sum(En(:,p));
        EEEEn(kk,q)=sum(En(q,:));
        EEEEEn(kk)=sum(sum(En));

    end
end

% b=[zeros(1,7);a(12,:);a;zeros(1,7)];

```

```

%
end
    end
end
end

end

b=[zeros(1,5);a(12,:);a;zeros(1,5)];
% plot(Wcount1(1000:100000),abs(HH(:,(1000:100000))'))
Emin=min(EEEEEn)
Kk=find(min(EEEEEn)==EEEEn)
kmin=kkk(Kk,:)
if ii==20
nn11=kmin(1);
nn12=kmin(1);
nn21=kmin(2);
nn22=kmin(2);
nn31=kmin(3);
nn32=kmin(3);
nn41=kmin(4);
nn42=kmin(4);
nn51=kmin(5);
nn52=kmin(5);
else
ii11=kmin(1)-1;
ii12=kmin(1)+1;
ii21=kmin(2)-1;
ii22=kmin(2)+1;
ii31=kmin(3)-1;
ii32=kmin(3)+1;
ii41=kmin(4)-1;
ii42=kmin(4)+1;
ii51=kmin(5)-1;
ii52=kmin(5)+1;
end

if ii11==0
    ii11=1;
elseif ii12==5
    ii12=4;
end
if ii21==0
    ii21=1;
elseif ii22==5
    ii22=4;
end
if ii31==0
    ii31=1;
elseif ii32==5
    ii32=4;
end
if ii41==0
    ii41=1;
elseif ii42==5
    ii42=4;
end
if ii51==0
    ii51=1;
elseif ii52==5
    ii52=4;
end
end

```

```

end
kkmin=[kk1(kmin(1)),kk2(kmin(2)),kk3(kmin(3)),kk4(kmin(4)),kk5(kmin(5))]
Emin=min(EEEEEn)
Eminj(Jj)=Emin
kkminj(Jj,:)=kkmin
    end
    end
end
end

% %
plot(W11,abs(T1y1f),W11,abs(T2y1f),W11,abs(T3y1f),W11,abs(T4y1f),W11,abs(T1y2f),
W11,abs(T2y2f),W11,abs(T3y2f),W11,abs(T4y2f),W11,abs(T1y3f),W11,abs(T2y3f),W1
1,abs(T3y3f),W11,abs(T4y3f))
T=[0,30,45,75,90,120,150,180,210,240,270,285,315,330,360]*pi/180;
% T1=[45,75,90,120,150,180,210,240,270,285,315,330]*pi/180;
% note, the column number is the appropriate channel name in chan_list
% Fvert=filtfilt(B,A,userData.timeHistory(:,1));
% Flat=filtfilt(B,A,userData.timeHistory(:,2));
% Flong=filtfilt(B,A,userData.timeHistory(:,3));
% ATlat=filtfilt(B,A,userData.timeHistory(:,4));
% ATlong=filtfilt(B,A,userData.timeHistory(:,5));
% you need to change the variable name and the column number to get the
% appropriate data vector

% [T1y,w1y]=tfestimate(F,A1y,[],[],[],1000);
% [T2y,w2y]=tfestimate(F,A2y,[],[],[],1000);
% [T3y,w3y]=tfestimate(F,A3y,[],[],[],1000);
% [T4y,w4y]=tfestimate(F,A4y,[],[],[],1000);
% plot(w1y,abs(T1y),w2y,abs(T2y),w3y,abs(T3y),w4y,abs(T4y))
% % plot(w1y,angle(T1y),w2y,angle(T2y),w3y,angle(T3y),w4y,angle(T4y))
% legend('1','2','3','4')
%
% [Pxx1,W1]=pwelch(A1y,[],[],[],1000);
% [Pxx2,W2]=pwelch(A2y,[],[],[],1000);
% [Pxx3,W3]=pwelch(A3y,[],[],[],1000);
% [Pxx4,W4]=pwelch(A4y,[],[],[],1000);
% plot(W1,Pxx1)

```

pdetestboth_sweep3.m

This program performs the modal analysis on the flexible ring modal with a complex damping term added in.

```
function pdex4
m = 0;
% x = [0 0.005 0.01 0.05 0.1 0.2 0.5 0.7 0.9 0.95 0.99 0.995 1];
% t = [0 0.005 0.01 0.05 0.1 0.5 1 1.5 2];
x=linspace(5*pi/180,355*pi/180,101);
% x=linspace(0,360*pi/180,11);
% t=linspace(0,10*pi/22,101);
co=4001
t=linspace(0,16,co);
aa=1;
d=0;
xxx=sin(2*pi*t.*(aa*t+d)).*0.01-.03;
xx=xxx(1:co);
options=odeset('RelTol',1e-3,'AbsTol',[1e-4],'NormControl','on');
% options=odeset('RelTol',1e-4,'AbsTol',[1e-6],'NormControl','on');
sol = pdepe(m,@pdex4pde,@pdex4ic,@pdex4bc,x,t,options);
size(sol)
u1 = sol(1:co,:,1);
u2 = sol(1:co,:,2);
u3 = sol(1:co,:,3);
u4 = sol(1:co,:,4);
save pdesweep_fixed_normal100_0_20_damp_3e3

% -----
function [c,f,s] = pdex4pde(x,t,u,DuDx)
EI=4;
EA=4.9e6;
R=.3;
p0=2.2e5;
br=.152;
cbw=1.93e6;
cbv=6.49e5;
% pA=3.81;
pA=3.81*1e2;
a1=EI/R^4;
a2=p0*br/R;
a3=(EA/R^2-p0*br/R+cbw);
% a4=pA*1e1;
K=3e3*(1+0*i);
% K=0;
% sqrt(5*(EA/R^2-p0*br/R+cbw)/pA)/2/pi
AAA=EA/R^2-p0*br/R+cbw;
% W=sqrt(a3/a4)
c = 1/1*[1;pA;1;pA;0];
% c=[1;1];
% f = [0;EI/R^4*(DuDx(3)^2-DuDx(1))-
EA/R^2*(u(3)+DuDx(1));0;EI/R^4*(DuDx(3)^3-DuDx(1)^2)+EA/R^2*(u(1))-
p0*br/R*DuDx(3)];
```



```

f = -1/1*[0;-EA/R^2*DuDx(1);0;EI/R^4*DuDx(5)-a2*DuDx(3);DuDx(3)];
% f = 1/AAA*[0;-1*EI/R^4*(DuDx(3)^2-DuDx(1))+EA/R^2*(u(3)+DuDx(1));0;-
1*EI/R^4*(DuDx(3)^3-DuDx(1)^2)-EA/R^2*(u(1))+p0*br/R*DuDx(3)];
% f=[0;EI/R^4*(DuDx(3)^2-DuDx(1))-
EA/R^2*(u(3)+DuDx(1));0;a1*(DuDx(3)^3-DuDx(1)^2)+a3*(

% f=[0;0];
% f=[0;-DuDx(1)-DuDx(1)];
% y = u(1) - u(2);
% F = exp(5.73*y)-exp(-11.47*y);
% s = -1/1*[-u(2);EI/R^4*DuDx(5)-EA/R^2*DuDx(3)+cbv*u(1);-
u(4);EA/R^2*(u(3))-a2*u(3)+cbw*u(3)+EA/R^2*DuDx(1);-u(5)-DuDx(1)];
s = -1/1*[-u(2);EI/R^4*DuDx(5)-EA/R^2*DuDx(3)+cbv*u(1);-
u(4);EA/R^2*(u(3))-a2*u(3)+cbw*u(3)+EA/R^2*DuDx(1)+K*u(4);-u(5)-
DuDx(1)];
% s = 1/AAA*[u(2);-cbv*u(1);u(4);-1*(EA/R^2-p0*br/R+cbw)*u(3)-K*u(3)];
% KK=.06*(EA/R^2-p0*br/R+cbw)
% pA
% sqrt(KK/pA)
% s=[u(2);u(1)+u(2)];
% s = [u(2);a3*u(1)+K*u(1)^2];
% s = [u(2);a3*u(1)+K*u(2)];
% -----
function u0 = pdex4ic(x);
% u0 = [cos(x); 0];
% u0=[.01;0];
d=0;
if x==5*pi/180
    u0=[0;0;-.03;.01*2*pi*d;0];
elseif x==355*pi/180
    u0=[0;0;-.03;.01*2*pi*d;0];
else
    u0=[0;0;0;0;0];
end
% u0=[0,0];
% -----
function [pl,ql,pr,qr] = pdex4bc(xl,ul,xr,ur,t)
% if t<=1e-4
%     o=.01;
% else
%     o=0;
% end
aa=1;
d=0;
% pl = [ul(1);ul(2);ul(3)-sin(2*pi*t*(aa*t+d))*0.01+.03 ; ul(4)-
.01*cos(2*pi*t*(aa*t+d))*(2*pi*(aa*t+d)+aa*2*pi*t);ul(5)];
pl = [ul(1);ul(2);ul(3)-sin(2*pi*t*(aa*t+d))*0.01+.03 ; ul(4)-
.01*cos(2*pi*t*(aa*t+d))*(2*pi*(aa*t+d)+aa*2*pi*t);0];
% pl = [ul(1)-sin(50*t)*.01; ul(2)];
% pl = [ul(1)-o; ul(2)];
ql = [0;0;0; 0;1];
% pr = [ur(1);ur(2);ur(3)-sin(2*pi*t*(aa*t+d))*0.01+.03; ur(4)-
.01*cos(2*pi*t*(aa*t+d))*(2*pi*(aa*t+d)+aa*2*pi*t);ur(5)];
pr = [ur(1);ur(2);ur(3)-sin(2*pi*t*(aa*t+d))*0.01+.03; ur(4)-
.01*cos(2*pi*t*(aa*t+d))*(2*pi*(aa*t+d)+aa*2*pi*t);0];

```

```
% pr = [ur(1)-sin(50*t)*.01; ur(2)];  
% pr = [ur(1)-o; ur(2)];  
qr = [0;0;0; 0;1];
```

pdesweep_config2.m

This file compiles the results obtained from **pdetestboth_sweep3.m** and computes the FRFs

```
% xxx=sin(2*pi*t.*(100/100*t+5))*0.01;
% xx=xxx(1:10001);
F=1/t(2);
FF=floor(F*50)

[tt,www]=tfestimate(xx,u3(:,3),[],[],FF,F);
zzz=size(tt);
ZZ=zzz(1);
% T=x([2,5,10,15,20,25,30,35,40,45,50,55,60,65,70,75,80,85,90,95,100])';
T=x;
for i=1:101
% [TT,W1]=tfestimate(xx,u3(:,i),[],[],[],F);
% size(TT)
if i==1
    TTT(:,i)=repmat(1,ZZ,1);
elseif i==101
    TTT(:,i)=repmat(1,ZZ,1);
else
    [TT,W1]=tfestimate(xx,u3(:,i),[],[],FF,F);
    TTT(:,i)=TT;
end
end

W=repmat(W1,1,101);
HH=TTT';

NN=101

mm=1;
```

testest3final_pde_2.,

This file uses the FRFs from the above program to perform the modal analysis that was done on the experimental data on the analytical data from the flexible ring model.

```
mm=1;
% Wcount1=resample(W11,1,1);
% Wcount=Wcount1(1:25000);

%
w=[Wcount1';Wcount1';Wcount1';Wcount1';Wcount1';Wcount1';Wcount1';Wcount1';Wcount1';Wcount1';Wcount1'];
Jj=0;
% w1=58.6
% w01=linspace(30,130,401)
w01=1.1
% w02=linspace(43,68.4+2,7)
% w03=linspace(75,82+2,7)
% w04=linspace(84,101+2,7)
% w05=linspace(90,55,11)

for j1=1:1
Jj=Jj+1

% for i=1:1
W0(j1,:)=linspace(w01(j1)*.95,w01(j1)*1.05,100);
% end

% for j=1:1
for i=1:100
count(i,j1)=find(min(abs(W1-W0(j1,i)))==abs(W1-W0(j1,i)));
count1=find(min(abs(W1-W0(j1,i)))==abs(W1-W0(j1,i)));
count(i,1)=count1(1);
end
% end
% k=1

kk1=linspace(0,1,1001);

for ii=1:1001

kkk1=kk1;

for o=1:100
G(ii,o)=1./(w01(j1)^2+2*sqrt(-1)*kk1(ii)*w01(j1).*W0(j1,o)-W0(j1,o).^2);
end

% for p=1:1
for n=1:NN
for j=1:100
% Wplot(n,j)=W1(count(j,j1));
H(n,j)=HH(n,(count(j,j1)));
% HP(m,n)=mean(angle(H(n,:)));
% G(i,:)=1./(w1^2+2*i*k(1)*w01*w1-w01.^2);
```

```

%      G(n,j)=1./(
end
end
      AV(j1)=mean(mean(abs(H)));
      for q=1:NN

          a(q,ii)=(conj(G(j1,:))*H(q,:).')/(conj(G(ii,:))*G(ii,:).');
%      E(q,ii)=norm(real((H(q,:)-a(q,ii)*G(j1,:)))));
%      Ei(q,j1)=norm(imag((H(q,:)-a(q,j1)*G(j1,:)))));
      En(q,ii)=sum(abs((((abs(H(q,:))-abs(a(q,ii)*G(ii,:))))));
%      EE(ii,j1)=sum(E(:,j1));
%      EEE(ii,q)=sum(E(q,:));
%      EEEE(ii)=sum(sum(E));
%      EEI(ii,j1)=sum(Ei(:,j1));
%      EEEI(ii,q)=sum(Ei(q,:));
%      EEEIi(ii)=sum(sum(Ei));
      EEn(ii,j1)=sum(En(:,ii));

          EE(ii,j1)=sum(En(:,ii))./AV(j1);

%      EEEn(ii,q)=sum(En(q,:));
%      EEEEn(ii)=sum(sum(En));

          end
% end

% b=[zeros(1,7);a(12,:);a;zeros(1,7)];
%
% end

end
% kkmin=[kk1(kmin(1))];
% Emin=min(EEEn);
% Eminj(Jj)=Emin;
% kkminj(Jj,:)=kkmin;

%
kkminr=[kk1(kminr(1)),kk2(kminr(2)),kk3(kminr(3)),kk4(kminr(4)),kk5(kminr(5))];
% Eminr=min(EEEE);
% Eminjr(Jj)=Eminr;
% kkminjr(Jj,:)=kkminr;
%
%
kkmini=[kk1(kmini(1)),kk2(kmini(2)),kk3(kmini(3)),kk4(kmini(4)),kk5(kmini(5))];
% Emini=min(EEEEi);
% Eminji(Jj)=Emini;
% kkminji(Jj,:)=kkmini;
% Eminw(j1)=Emin;
% kminw(j1)=kmin;
kk(j1)=find(min(EEEn(:,j1))==EEn(:,j1));
kmin(j1)=kk1(kk(j1));
emin(j1)=EEEn(kk(j1),j1);
eemin(j1)=EE(kk(j1),j1);
aa([1:NN],j1)=a(:,kk(j1))
end

```

```

% t=linspace(0,2*pi,100);
% for i=1:12
%     aaa(i,:)=abs(aa(i))*sin(t+angle(aa(i)));
% end
% %
plot(W11,abs(T1y1f),W11,abs(T2y1f),W11,abs(T3y1f),W11,abs(T4y1f),W11,abs(T1y2f),
W11,abs(T2y2f),W11,abs(T3y2f),W11,abs(T4y2f),W11,abs(T1y3f),W11,abs(T2y3f),W11,abs(T3y3f),W11,abs(T4y3f))
% T=[0,30,45,75,90,120,150,180,210,240,270,285,315,330,360]*pi/180;
% T=[45,75,90,120,150,180,210,240,270,285,315,330]*pi/180;

```

Bibliography

- Ewins, D.J. (2000). *Modal Testing: Theory, Practice and Application (2nd Edition)*. Philadelphia, PA: Research Studies Press Ltd.
- Fricke, D. (2006). Effective Road Profile Control: ATC Technology Review. Ground Vehicle and Advanced Systems, MTS Systems Corporation.
- Gong, S. (1993). A Study of In-Plane Dynamics of Tires (Doctoral dissertation, Delft University of Technology, The Netherlands).
- Matlab Tutorial*. (2005). Matlab ver. 7.0.4.365 (R14)
- Meirovitch, L. (2001). *Fundamentals of Vibrations*. New York, NY: McGraw-Hill.
- Nayfeh, A. H., Balachandran, B. (1995). *Applied Nonlinear Dynamics, analytical, computational, and experimental methods*. New York, NY: John Wiley & Sons, Inc.
- Pacejka, H.B. (2005). *Tire and Vehicle Dynamics, Second Edition*. Warrendale, PA: SAE International
- Worden, K., and Tomlinson, G.R. (2001). Nonlinearity in experimental modal analysis. *Dynamics Research Group, Department of Mechanical Engineering, University of Sheffield*. Sheffield S1 3JD, UK.
- Yam, L.H., Guan, D.H., and Zhang, A.Q. (2000). Three-dimensional Mode Shapes of a Tire Using Experimental Modal Analysis, *Experimental Mechanics*, 40, 369-375.
- Zavodney, L. (1997). Can the modal analyst afford to be ignorant of nonlinear vibration phenomena? *Engineering Science and Mechanics Department, Virginia Polytechnic Institute and State University*. Blacksburg, VA.
- Zegelaar, P. (1997) Modal Analysis of Tire In-Plane Vibration. *SAE International*. SAE971101